VISER
www.viserdata.com

RESEARCH AND APPLICATION OF
MATERIALS SCIENCE

ISSN:2661-4464(**online**) 2661-4456(**print**)
Volume 4 No. 1 2022

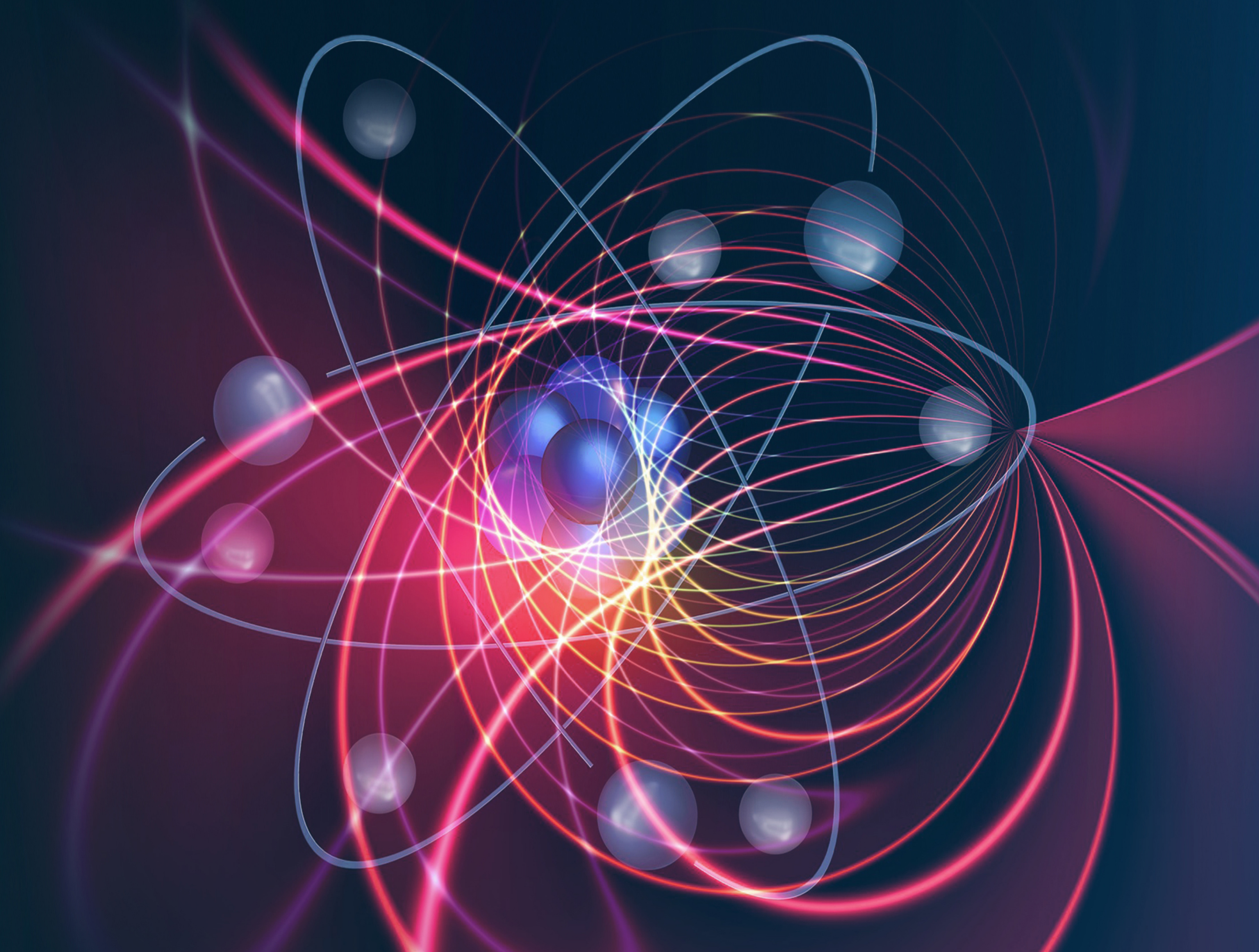

COMPANY INTRODUCTION

Viser Technology Pte. Ltd. was founded in Singapore with branch offices in both Hebei and Chongqing, China. Viser focuses on publishing scientific and technological journals and books that promote the exchange of scientific and technological findings among the research community and around the globe. Despite being a young company, Viser is actively connecting with well-known universities, research institutes, and indexation database, and has already established a stable collaborative relationship with them. We also have a group of experienced editors and publishing experts who are dedicated to publishing high-quality journal and book contents. We offer the scholars various academic journals covering a variety of subjects and we are committed to reducing the hassles of scholarly publishing. To achieve this goal, we provide scholars with an all-in-one platform that offers solutions to every publishing process that a scholar needs to go through in order to show their latest finding to the world.

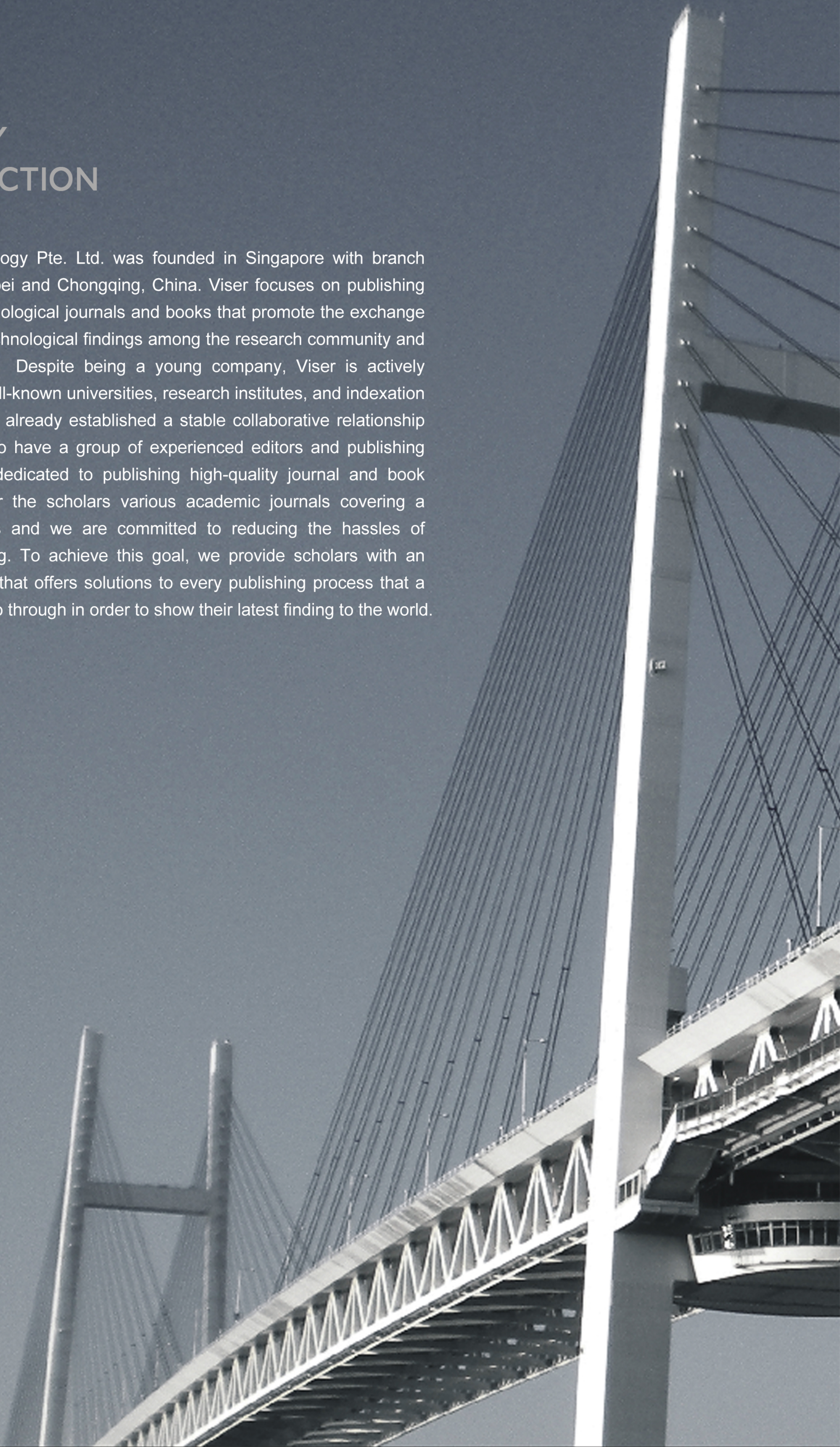

Research and Application of Materials Science

Publisher: Viser Technology Pte. Ltd.

ISSN: 2661-4464(online)
2661-4456(print)

Frequency: Semi-annual

Add.:21 Woodlands Close, #08-18
Primz Bizhub SINGAPORE (737854)

https://www.viserdata.com/

Editors:

Yajun Lian
John Wilson
Mart Chen
Debra Hamilton
Jennifer M Dohy
Edward Adam Davis
Yanli Liu
Nike Yough
Qiuyue Su
Xin Di
Xiuli Li
Liangjun Qiu

Designer: Anson Chee

Research and Application of Materials Science

Volume 4 No.1 (2022)

CONTENTS

Viser Technology Pte. Ltd.
Research and Application of Materials Science
DOI: 10.33142/rams.v4i1.8457

Research Article **Open Access**

Unsaturated transport properties of water molecules and ions in graphene oxide / hydrated calcium silicate nanochannels: from basic principles to complex environmental performance effects

Zhuye HUANG, Yong FENG, Hongwei WANG, Lei FAN*

School of Civil Engineering and Architecture, Zhejiang University of Science & Technology, Hangzhou, China

***Corresponding Author:** *Lei FAN, E-mail: fanleigl@foxmail.com*

Abstract:
The problems of traditional concrete such as brittleness, poor toughness and short service life of concrete engineering under acid rain or marine environment need to be solved urgently. Hydrated calcium silicate (C-S-H) is a key component to improve the mechanical properties and durability of concrete. However, the traditional method of concrete material design based on empirical models or comparative tests has become a bottleneck restricting the sustainable development of concrete. The synthesis method, molecular structure and properties of C-S-H were systematically described in this paper; The interface structure and interaction of graphene oxide / calcium silicate hydrate (C-S-H / GO) were discussed. On this basis, the saturated and unsaturated transport characteristics of ions and water molecules in C-S-H / GO nanochannels under the environment of ocean and acid rain were introduced. The contents of this review provide the basis for improving the multi-scale transmission theory and microstructure design of concrete. It has important guiding significance for analyzing and improving the service life of concrete in complex environment.

Keywords: *acid rain environment ; marine environment ; Service life of concrete ; Graphene oxide / calcium silicate hydrate ; molecular dynamics ; Unsaturated transport of ions and water molecules.*

Abbreviations: C-S-H , Hydrated calcium silicate; GO, Graphene oxide ; C-S-H / GO, Hydrated calcium silicate / Graphene oxide ; MD, molecular dynamics; SFCB, Steel continuous fiber composite reinforcement; SEM, scanning electron microscope; LK , Lerf-Klinowski ; DSM , Dynamic structural model.

1 Introduction

With the continuous development of science and technology, concrete materials are extensive used in various buildings. It is a kind of composite heterogeneous material, which has the distinguishing features of high compressive strength and good compatibility with the surrounding environment. At the same time, it has low production cost and easy access to raw materials. Therefore, its strength and durability have been studied by many researchers [1-6]. The effect of surroundings on the durability of concrete is one of the most common factors. Among them, acid rain and ocean are the two most common environments that influence the endurance of concrete.

With the development of industrialization, the impact of acid rain on all parts of the world has become more and more serious in the past ten years. And the erosion of acid rain causes huge economic losses every year. It is estimated that China's annual economic loss in building materials due to acid rain exceeds 2.5 billion dollars [7-8]. At the same time, due to the superposition of multiple and complex factors (such as salinity, climate and biology), the corrosion of marine engineering structures has also become a worldwide problem. The corrosion of marine buildings in the world has caused serious economic losses. According to statistics, the cost of highway bridges in the United States due to concrete corrosion reached 27.6 billion dollars in 1998; 75% of concrete bridges in England and Wales are corroded by seawater, and the maintenance cost is twice as high as the construction cost; The corrosion of marine engineering in China is also serious, and the loss of marine corrosion accounts for about 1 / 3 of the total corrosion loss, as high as 700 billion RMB. Therefore, strengthening the durability and strength of concrete structures in these environments and extending the service life are essential research directions.

In view of these factors, adding admixture to cement-based materials is a major means to prepare high-performance concrete materials. Admixture is an

Received on April 10, 2022; Accepted on May 11, 2022

indispensable part of concrete, which is the consensus of all civil workers now. High performance concrete mainly improves the workability and durability of concrete by adding additives. In particular, high-efficient water reducing agent can fully disperse cement particles and improve the pore structure and interface microstructure on the basis of reducing water consumption. Therefore, the concrete is more dense and the mechanical properties are greatly improved. Whether impermeability or chloride ion diffusion, sulfate corrosion resistance and wear resistance are better than concrete without admixture. It not only improves the workability of concrete, but also improves its durability and strength. So, it is possible to prepare high performance concrete with high strength and high durability only by mixing high efficiency water reducing agent.

And admixtures can be divided into inorganic admixtures, organic admixtures and composite admixtures according to chemical composition. Among them, organic admixtures account for the vast majority of concrete admixtures, such as high-performance water reducer, retarder and so on[9].

Z.C. Lu [10]studied the role of organic admixtures with different functional groups in cement hydration. He summarized that the addition of organic admixtures can improve the plasticity of concrete materials and prevent the occurrence or increase of cracks. Besides, it can also effectively improve the service strength and service life of concrete. On the other hand, he found the difference between the functional groups and molecular structures contained in the small organic molecules in the organic admixtures will affect the cement hydration. The carboxyl groups on the polymer surface can prolong the cement hydration time, which is conducive to ensuring the workability of concrete.

C-S-H is the main cementation phase of concrete materials, accounting for over half of cement hydration products. Therefore, research on materials based on hydrated calcium silicate has been paid more and more attention. In addition, graphene oxide as a derivative of graphene has excellent mechanical properties and has gradually become a popular cement-based modified material.

Meanwhile, in order to simulate and analyze more intuitively, molecular simulation of materials was led into the research field of new concrete materials at the beginning of the 21st century, especially in the study of microstructure and performance of hydration products of cement.

The environment such as acid rain and ocean has a great impact on the service life of concrete. They circulate dry and wet in the concrete. So, the water and ions in concrete belong to unsaturated transport. At the same time, M. Devasena et al.[11] employed GO to study its influence on the mechanical properties and durability of concrete. Their results showed that when the addition amount of GO was 0.1%, the strength of concrete increased by the highest extent. The compressive strength of concrete with 0.1% GO was 11% higher than that without GO when the flexural strength was 4% higher. Therefore, the demand for unsaturated transport of water and ions in C-S-H / GO is increasing every year. However, due to the relatively complex structure of C-S-H and other reasons, the research on micro mechanism is limited.

Therefore, this paper summarizes the construction of multi-scale C-S-H/GO variable model using molecular dynamics method to study the unsaturated transport of water molecules and ions. It can provide a basis for improving the multi-scale transport theory and microstructure design of concrete, which can also have important guiding significance for analyzing and improving the service life of concrete in complex environments

2 Environment and concrete structure

2.1 Influence of environment on durability of concrete structure

Environment is an important factor influencing the ruggedness of concrete. Freezing thawing, sulfate and other different environments will have various adverse effects on the mechanical properties and ruggedness of concrete materials. Acid rain and ocean are the two most common environments that affect the durability of concrete.

When the concrete construction is eroded by acid rain, cement hydration products will react with acid rain to form ettringite or gypsum, which will dilate its volume by 1.5-2.2 times and generate tensile stress inside, resulting in cracks and spalling in the concrete. Its mechanical properties, interface bonding and composition will change accordingly [12-19], and finally the strength and durability of the concrete structure will gradually decrease [20-21].

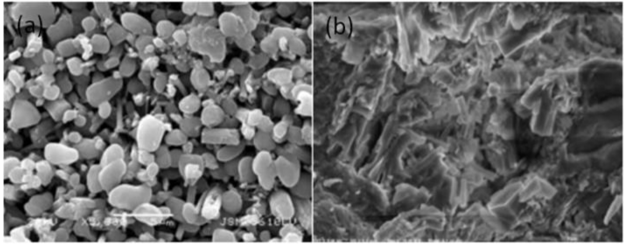

Figure 1 SEM of concrete before (a) and after (b) acid rain erosion [22]

In the marine environment, concrete structures bear static and hydrodynamic loads due to water pressure and have complex stress states [23-24]. In addition, water is easy to penetrate into concrete under high pressure, which will result in the decline of its internal mechanical performance. Although some scholars have fully considered the quiescent condition and fatigue behavior of concrete structures in epeiric sea [25-30], it is still difficult to analyze the impact of high water pressure in deep sea [31-32]. At the same time, the concrete construction in the district where the water level drops is most vulnerable to corrosion. In this district, the concrete is repeated to dry and wet cycles, which leads to complex chemical reactions of chloride ions, sulfate ions and magnesium ions in seawater to cement concrete [33-36]. There is also physical erosion caused by crystallization pressure of sea salt and wave action in this area [37]. When the concentration of chloride ion in reinforced concrete attains a certain range, the chloride ion will be adsorbed on the superficial layer of reinforcement, thus accelerating the corrosion rate. Under the condition of sufficient chloride ion and water, the corrosion rate of reinforcement will be accelerated with the large amount of chloride ion [38]. With the increase of corrosion, the volume will gradually increase to 2-6 times of the original reinforcement volume, thus generating expansion pressure on the boundary between cement and reinforcement. After that, the tensile stress loss will lead to concrete cracking and delamination. It also will reduce the cross-sectional area of reinforcement, and finally damage the durability of concrete structure [39-40].

Figure 2 marne corrosion surface[41]

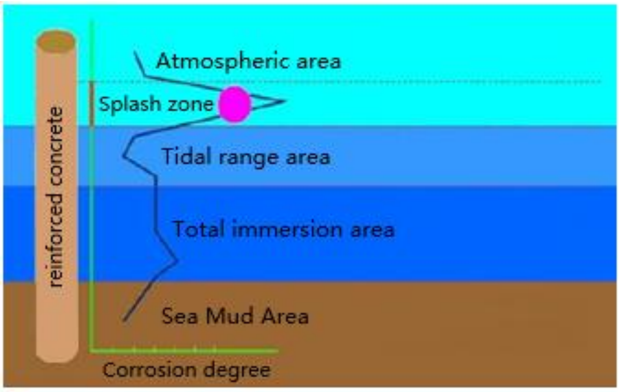

Figure 3 characteristics of marine corrosion zoning[42]

Because these environments have an important influence on the durability and strength of concrete, it is particularly important to research these factors.

2.2 Research status in various countries

According to the environment of acid rain, H.F. Yuan et al. [43] examined the degradation model of concrete corroded by sulphuric acid and built a simplified damage model to describe the deterioration of concrete induced by gypsum expansion in accordance with the acid rain environment. The resistance of glass powder content in cement materials to sulfuric acid was researched by H. Siad et al. [44]. They discovered that adding more glass powder to mortar will boost its resistance to sulfuric acid. F. Girardi and R.D. Maggio [45] studied the resistance of concrete mixtures to periodic sulfuric acid and sulfate solutions, and the results showed that the deterioration of concrete mixtures was particularly serious when the samples contained ordinary aggregates and were regularly exposed to sulfuric acid and mixed sulfate solutions. M. Mahdikhani et al. [46] found when exposed to sulfuric acid rain, silica-containing concrete samples' mechanical properties and durability were examined. They discovered that as the acidity of the solution increases, the concrete's quality degrades, its resistance and adsorption coefficient rise, but its compressive strength falls. In their study of the dry-to-wet cycle test for concrete under sulfate-accelerated corrosion, J.J. Guo et al. [47] investigated the effect of dry-to-wet duration ratio on sulfate corrosion of concrete. According to the test results, there are three stages to the sulfate change during dry-wet cycle erosion: the increasing period, the fluctuating period, and the quick decreasing period.H. Siad et al. [48] also recommended a new treatment procedure to accelerate the degradation process of concrete sulfate erosion, and found that the use of supplementary pretreatment in the dryer is an important acceleration of the degradation process. After studying the damage process of concrete subjected to sulfate attack under bending force and dry wet cycle, J.M. Gao [49] found that both bending load and dry wet cycle can hasten concrete degradation.

For the marine environment, H. Fazli et al. [50] investigated the effects of the marine environment on the bonding and exposed surface of concrete slabs. They discovered that a 12-month marine exposure had little effect on the performance of the epoxy resin between the carbon fiber reinforced polymer composite and concrete. W.H. Hu et al. [51] conducted an experimental study on the uniaxial compressive strength of concrete under natural and saturated conditions, and found that the concrete sample showed greater strength under water saturated conditions. C. Poinard et al. [52] reported that in the cyclic hydrostatic test, the most serious damage of cement matrix was observed between 60 and 150 MPa, and the linear elastic behavior was observed when the confining pressure was less than 60 MPa.

In recent years, scholars from various countries have done lots of research in this district, which provides a variety of new ideas for enhancing the ruggedness of concrete. However, due to the relatively complex construction of C-S-H in concrete, the liquid-solid interface interaction, the saturation model established by the experiment is not applicable to the unsaturated state and so on, which limits the research on the micro mechanism, especially the research on the molecular scale. Therefore, it is particularly important to build a multi-scale model by MD to research the unsaturated transport of water molecules and ions in C-S-H, which provides a theoretical basis for the microstructure design of concrete.

3 MD theory and Application

The main characteristic spatial scales of concrete cementitious materials are divided into macro scale, meso scale, micro scale and nano scale. In the first three scales, scholars in various countries have many relevant test methods and theories, and a set of mature research systems. A example multi-scale complicated material is cement, especially the complex structure of C-S-H in the nano scale limits the study of its micro and nano mechanism. Therefore, using molecular simulation as an auxiliary means of experiments can model multi-scale and effectively solve the limitations of experiments.

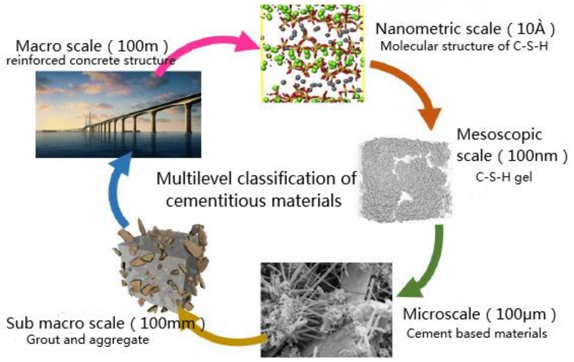

Figure 4 multi-scale representation of cement materials [53]

Molecular simulation is a method to simulate the structure and movement of molecules by using a computer molecular model in the unit of atoms, so as to simulate various chemical and physical attributes of molecular systems. It is based on experiment, through the basic principle to build the corresponding model and algorithm, so as to deduce the reasonable molecular structure and molecular motion. It can simulate static molecular structure and dynamic molecular motion. There are two main simulation methods: molecular Monte Carlo method and MD method.

In the molecular simulation of new concrete materials, the molecular kinematics method is generally used. This method primarily uses Newtonian mechanics to simulate the motion of the molecular system. Samples are taken from systems made up of various molecular states in order to calculate the configuration integral of the molecular system, which is then used to determine the molecular system's thermodynamic behavior and other pertinent information.

Its advantage is that the force between atoms is equivalent to the motion between particle coordinates by using appropriate simplified conditions, thus avoiding complex quantum calculation equations. While ensuring the accuracy, it greatly improves the applicable scope of atomic simulation, and can reach the operation of millions of atoms.

Because of the ocean, the environment such as acid rain is in an unsaturated state. However, most of the experimental studies of various researchers are based on the saturation model. However, the saturated model is not suitable for the unsaturated state, so there is a certain error between the experimental results and the reality. Therefore, studying the unsaturated transport of C-S-H / GO by MD can not only solve the limitations of experiments, but also solve the difficulties of finite element method or linear elastic fracture mechanics in continuum theory. It can observe and model multi-scale and simulate complex chemical reactions, so as to increase the longevity of cement-based materials even more.

4 Molecular structure and properties of multi-scale cement-based materials

4.1 Molecular structure and properties of C-S-H

C-S-H has the characteristics of strong surface activity, light weight, hydrophilicity and poor compatibility with organic aggregates. It is the primary product of hydration of cement-based cementitious materials. It can absorb some alkali metal ions and inhibit alkali aggregate reaction to some extent, so as to enhance the compressive strength of concrete in all aspects, effectively improve the cracking resistance and impermeability of concrete. At the same time, it is a mesoporous medium with pores that range in size from 0.5 nm to 10 nm [54-57], which can be used as a crucial conduit for ion transport.

In addition, C-S-H is a layered and arranged construction with complex chemical bonds. At the same time, other added polymers further increase the complexity of its structure. So far, it is generally believed that C-S-H and Tobermorite crystals have similar crystal structures, with short layer ordered and long layer disordered gel properties. The morphology of C-S-H is in an amorphous state, and the accumulated particles form relatively loose flakes. Defective silicon chains grow on the calcium layer of its crystal structure, which form a silicon calcium framework. Water molecules, calcium hydroxyl groups and silicon hydroxyl groups are distributed in the adjacent interlayer regions, which are characterized by high silicon calcium ratio, low silicon chain polymerization degree and low crystallinity.

P.A. Bonnaud et al. [58] researched the properties of confined water in C-S-H under different relative humidity through giant regular Monte Carlo simulation, and found that the influence of confined water on C-S-H condensation depends on the inter particle spacing between C-S-H particles. N. Giovambattista et al. [59] investigated the impact of surface polarity on the composition, dynamics, and mechanical characteristics of silicate interlayer water. The findings demonstrate that the hydrophilicity and hydrophobicity of silicate chains influence the structure of water molecules on the surface, and that the ice-like water layer of silicate crystals is responsible for the low rate of water molecule diffusion near the hydrophobic surface. M.J.A. Qomi et al. [60] ran MD simulations on 150 models with various Ca/Si ratios,. It was discovered that the matrix's composition affects the physical and chemical characteristics of water. According to M. Youssef et al. [61], the radial interaction between non-bridged oxygen atoms (O-NB) and hydrogen atoms in the interfacial water molecules is what gives C-S-H nanopore surfaces their hydrophilicity. D.S. Hou et al. [62] improved the solid-liquid interface model of calcium hydroxysilicate and discovered that the silicate chain deflects chloride ions under extensive simulation over a long period of time. In addition, they also showed that calcium ions adsorbed on the solid-liquid interface can enhance the adsorption of chloride on the surface.

The transport of water and molecules in C-S-H nano channels is a major factor affecting the durability of concrete. Therefore, it is essential to study the C-S-H through MD, so as to regulate the ion transport in the C-S-H microstructure in order to obtain good durability.

4.2 Molecular structure of GO and its application in concrete

Graphene oxide, a graphene derivative, has gained popularity as a cement-based modified material because of its excellent mechanical properties. Graphene is the material with the highest strength known to human beings. However, because of its hydrophobic surface, it is difficult to dissolve and diffuse in water. Therefore, graphene oxide with high hydrophilicity is used as a new material for concrete research. Although the strength of GO is marginally inferior to that of graphene, it still retains the advantages of graphene's superior mechanical properties and super high specific surface area. It also has hydroxyl, carboxyl, epoxy and other active functional groups. These functional groups make it have excellent reaction activity, reduce the van der Waals force between graphene layers to avoid the two layers from converging, and can easily composite with other materials.

After oxidation treatment, GO still has the layered structure of graphite, but each layer's graphene monolayer has had several oxygen functional groups added to it, making the single graphene structure exceedingly complicated. Although computer simulation, nuclear magnetic resonance and other methods have been used for analysis, the precise structure of GO cannot be determined. At present, several structural models have been put out regarding the structure of GO , including LK model, dynamic structural model (DSM), two-component structural model and so on. The most widely accepted crystal structure model is the LK model, which randomly distributes hydroxyl and epoxy groups on the GO monolith and introduces carboxyl and carbonyl groups near the monolith's edge.

Compared with other carbon based nanomaterials (such as carbon nanotubes, carbon nanofibers, etc.), the attached oxygen-containing function makes GO a highly dispersed reinforcing agent in cement matrix, and these materials are easy to agglomerate in cement-based composites [66-67]. According to A. Mohammed et al. [68], GO inclusions increase the porosity of GO reinforced cement-based composites. Therefore, with the increase of GO percentage, the chloride ion permeability increases and the adsorption value decreases.

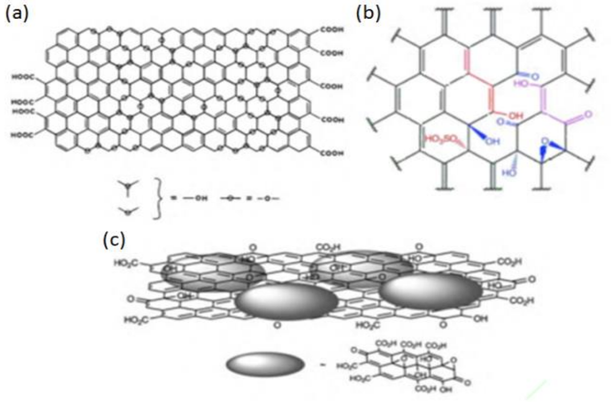

Figure 5 (a) LK model [63] , (b) DSM [64] and(c) two component structure model [65]

C.D. Sanglakpam [69] and others found that adding GO to concrete improved the ability of resisting sulfate attack, and with the increase of the percentage concentration of GO and gobm, the carbonation depth decreased. R.R. Bellum [70] and others found that the dense microstructure of the geopolymerized concrete sample made with graphene is beneficial for enhancing the geopolymer reaction. The GO with high specific surface area has the advantage of filling the gap and improving the strength performance of geopolymer concrete. S. Lv et al. [71] found that the oxygen-containing functional groups on the GO surface can offer adsorption sites for cement and promote the crystallization of cement hydration products through testing methods.

Although there is no unified theory about the chemical structure of GO at present, its tensile strength and compressive strength are enhanced by 53% and 91% respectively contrasted with those of the composites without graphene oxide, and the amount of 0.5% - 1% of other nano admixtures is reduced by nearly 20 times, which effectively reduces the carbon footprint in the cement production process, Therefore, it is necessary to study the unsaturated transport of GO in C-S-H by MD.

4.3 Synthesis and properties of C-S-H/GO

4.3.1 Synthesis of C-S-H / GO

C-S-H can be synthesized by hydrothermal synthesis, single ore hydration, solution synthesis and so on. Among them, the solution synthesis method is to dissolve calcium salt and silicon salt with deionized water, add 1-2ml sodium hydroxide solution to the mixed solution to keep the solution under alkaline conditions, and then add the two to the dispersant separately to obtain a mixed solution of C-S-H, which is relatively stable. Then, wash the sample with deionized water and absolute ethanol repeatedly, filter and wash at least three times, and then place the filtered C-S-H in the vacuum drying oven for drying for 1-2 days to obtain C-S-H.

The synthetic methods of GO mainly include Brodie method, staudmaier method and Hummers method. They all use strong protonic acid to deal with the original graphite to form a first-order graphite interlayer compound, and then add strong oxidant to oxidize it. Among them, Hummers method is the most widely used method with the best effect and the highest safety. It is to add natural graphite powder to sulfuric acid placed in the ice bath, add potassium permanganate and sodium nitrate under strong stirring, reduce excess manganese dioxide and potassium permanganate with 30% hydrogen peroxide and 1mol / L hydrochloric acid after three reaction stages, and after the black suspension turns bright yellow under the treatment of hydrogen peroxide, centrifuge the suspension until neutral, and dry at 60 ℃ to obtain graphite oxide. Finally, put the graphite oxide sheet into a beaker, add ultrapure water, and sonicate it to completely disperse it, so as to obtain GO solution.

4.3.2 Microstructure and property evolution of C-S-H/GO under complex environment

Under the erosion of acid rain environment, ions will invade along the C-S-H pore channel, and then react with it to form ettringite or gypsum, which will expand the original volume by 1.5-2.2 times, thus reducing the durability and strength of concrete. When GO with high surface area and good dispersion is added, the defect region of C-S-H can be repaired by forming an interlocking layered structure, improving its pore size distribution, reducing the total porosity and blocking its nanochannel connectivity, thus effectively preventing ion erosion and effectively alleviating the influence of acid rain environment on the strength and ruggedness of C-S-H.

In the case of freezing and thawing, the water in the channel of C-S-H will be frozen by cold, and the volume will start to increase, thus expanding the pores and forming water pressure, which will lead to concrete cracking and damage. When GO is added, due to the benefits of its large specific surface area, it can condense each phase, make it closely arranged, reduce the interface effect, improve the mechanical properties and reduce the influence of freezing and thawing environment on the physical properties of C-S-H.

Scholars from various countries have also conducted corresponding research on relevant aspects. W.L. Yang [72] et al. Studied that when the content of GO is 0.08%, the compressive strength of slag cement at 28d is increased by 10%, and the compressive strength of concrete at 28d is raised by 5.8%, and the fluidity of concrete, the corrosion coefficient of hydrogen and sulfate resistance are significantly improved. A. Mohammed et al. [68] studied the effect of GO on the transport performance of cement-based materials. The outcomes demonstrated that after adding GO, the anti chloride ion corrosion performance and water permeability of the test pieces were improved. GO crosslinked the hydrated crystals to form a relatively dense structure, decreased the invasion of chloride ions, and helped the concrete materials to be used in the marine environment for a longer time.

5 Study on structure and properties of C-S-H / GO based on MD theory

According to the structural similarity performance, the C-S-H model is usually replaced by Tobermorite 11 Å model for relevant simulation analysis. Its cell size is the a = 22.32 Å, b= 22.17 Å, c= 22.77 Å (α= 90°, β= 90°,γ= 90°)。 After that, the silicon tetrahedron partially bridged in the silicon chain was deleted, and the calcium silicon ratio of the model was adjusted to 1:4. Finally, a micro crack was generated in the z-axis direction along the middle of the cutting model.

The GO model uses graphite crystal instead of simulation analysis. Its cell size is the a = 2.46 Å, b= 4.26 Å, c= 3.4 Å (α= 90°,β= 90°,γ= 90°)。 Then, each unit cell was copied 15 times, 7 times and 1 times along the X, Y and Z directions, respectively. Then, on the basis of this graphene model, three functional groups of hydroxyl, epoxy and carboxyl were added to obtain the final GO structure. The number of three functional groups was 24, 24 and 12 respectively.

After the two models are constructed respectively, the GO model can be inserted into the nano-cracks of the C-S-H model for corresponding analysis. [70]

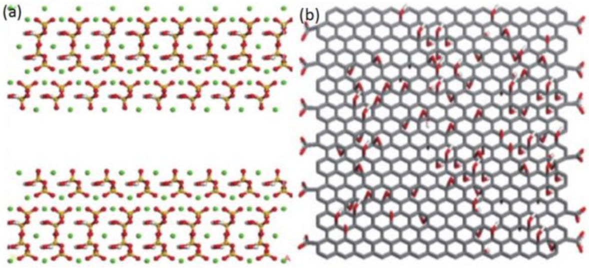

Figure 6 (a) Tobermorite 11Å model and (b) GO model [73]

5.1 Structural analysis of C-S-H / GO

The local structure of calcium ion in C-S-H determines the interface strength between it and GO. It acts as a bridge connecting adjacent silicon layers and can enhance the mechanical strength of multilayer graphene oxide sheets. However, calcium ions are present close to silicates, and silicate tetrahedron provides more oxygen sites for them, making calcium ions preferentially connected to them, which further results in the non-connection of more than half of the interlayer calcium ions to GO. Meanwhile, in water molecules, the hydrogen network formed between hydroxyl groups and functional groups also plays a key part in bridging calcium silicate sheets and GO. But due to the fracture of C-S bond, there are very few hydrogen bonds directly connected between C-S-H and GO. In addition, because of the weak interaction between the epoxy and oxygen atoms in the silicate chain, the hydrogen bond between the epoxy group in GO and the calcium silicate sheet is the weakest.

S. Sharma et al. [74] prepared two kinds of GO with thickness of 14nm, sheet diameter of 900nm, and thickness of 3nm, sheet diameter of 100nm by different methods, and studied the influence of the two GO on cement hydration crystals. The results showed that the large-size GO had more obvious regulating effect on hydration crystals, and the growth of hydration crystals was more dispersed; While the small diameter GO is more favorable to reduce the porosity and pore volume. The addition of GO can refine the microstructure of hydration products and efficiently enhance the macro bending strength and compressive strength. Q. Wan et al. [75] also studied the influence of different mixing amounts of GO on the microstructure, and found that the formation speed of hydrated crystals was accelerated, the arrangement tended to be regular, the acicular crystal clusters were significantly increased in the early stage, the number and volume of pores in the microstructure were significantly decreased, and the strength and toughness of the specimen were improved.

5.2 Mechanical properties of C-S-H / GO nanostructures

The GO reinforced C-S-H has superior mechanical characteristics when receiving tensile load because of the robust Ca-O bond and hydrogen bond. The interface region between two dissimilar materials often has weak load resistance, and fracture always happens there. However, the GO-reinforced C-S-H composite initially fails in the base material's matrix before breaking at the interface. This failure mechanism is very favorable for the devise of cement composite materials. It can simultaneously deform the C-S-H and GO composite materials to resist the load.

The chemical bonding between the functional groups of C-S-H and GO can effectively enhance the brittleness of materials. In addition, the carboxyl and hydroxyl groups in GO can maintain good stability and high interfacial strength in C-S-H, thus ensuring and improving the stability and durability of materials.

B. Fakhim et al. [76] researched the mechanical properties of GO cement-based composite. GO sol was prepared by oxidation-reduction and ultrasonic method and added to cement mortar to prepare GO cement-based composite. The results reflected that the best content of GO was 1.5wt%, which could improve the tensile strength of the material by 48%. Through FE-SEM, XRD and other tests, it is found that GO can slow down the development of cracks and promote, nucleate and template the formation of C-S-H gel. S. Lv et al. [77] Studied the influence of GO on the microstructure and performance of cement paste and its mechanism by preparing naphthalene water reducer / GO composite solution and adding it into cement mortar. Through comparison, the compressive strength and flexural strength of the sample can reach 65.4 MPa and 10.6 MPa when 0.06 g GO is added into 100 g of cement, respectively, increasing by 29.3% and 41.4%. SEM observation shows that GO can promote cement hydration reaction to form dense lamellar structure.

5.3 Analysis of interfacial atomic dynamics of C-S-H / GO

The hydrogen bonding of C-S-H and the coordination between Ca-O make the graphene oxide sheet stably confined in the nano gap of C-S-H, and the connection between the two is very stable. At the same time, the carboxylate functional group on GO has strong polarity and hydrophilicity, which can limit the adjacent water molecules through hydrogen bonding and play a role in stabilizing the interlayer water. Because the interlayer water can travel quickly and create a strong separation pressure, which decreases the stability of the chemical bonds in C-S-H and lowers the silicate materials' characteristics. Hydrophilic functional groups can efficiently stop water from moving, increasing the tensile strength of materials.

As mentioned above, the chemical bond between calcium ion and oxygen in functional groups and the hydrogen bond at the interface play a key role in bridging GO and C-S-H. The high strength Ca-Oc bond ensures the stability of GO and C-S-H binding. Calcium ions combine with adjacent water and hydroxyl groups to form a stable hydrated structure, while it is strongly restricted in the cage constructed by Si-O-Ca bonds. The bond strength of calcium ions between different functional groups should be GO-COOH > GO-OH > GO-Oo. Because carboxylate groups have high binding energy to calcium ions on the surface, GO-COOH can remain on the surface of C-S-H for a relatively long time.

The stability of the hydrogen bond depends on the polarity of the functional oxygen atom. Therefore, the carboxyl group model with high degree of protonation in GO can closely attract adjacent hydrogen atoms and improve bonding stability. On the contrary, epoxy groups with low polarity and weak hydrophilicity have weak restrictions on the movement of hydrogen atoms.

5.4 Chemical reaction of C-S-H / GO model

The closed environment of C-S-H will affect the stability of functional groups on GO, leading to its bond breaking and reforming. The calcium ions in the C-S-H layer move to the vicinity of the Oc of the epoxy group, stretching the broken C-O bond and generating the C = O bond. However, because the electronegativity of the epoxy group is low, the attraction between GO and C-S-H is very weak, so only a very small part will be destroyed to form the C = O bond.

Additional interactions between functional groups and C-S-H will take place. As time goes on, water molecules and C-OH groups will continue to decrease, when Si-OH and Ca-OH molecules will increase (eq.1).

This suggests that the hydrolysis reaction will not be prevented by the reaction of C-OH groups, but rather will be further promoted in the latter stages. But at the same time, carboxyl group can also inhibit the dissociation reaction of water to a certain extent, and affect the diffusion degree of GO in water according to the pH value (eq.2).

$$CaO\cdot SiO\cdot mH_2O+GO\text{-}OH+H_2O\rightarrow Ca(OH)_2+SiO_2(H_2O)_m+CO_2 \quad (1)$$

$$GO\text{-}COOH\rightarrow GO\text{-}COO^-+H^+ \quad (2)$$

Therefore, it can be shown that the non bridged sites and equilibrium ions provided by the C-S-H surface contribute to the deprotonation of the functional groups in the graphene oxide sheet, and the degree of reaction depends largely on the activity of the functional groups. On the other hand, the deprotonation reaction affects the hydrolysis reaction of water molecules in C-S-H, and the hydrolysis dissociation and deprotonation of GO will disturb the flatness of graphene bottom structure.

6 Unsaturated transport of water molecules and ions in C-S-H / GO

Ion transport affects the physical and chemical properties of cement-based materials in concrete, including ion diffusion and salt solution capillary adsorption. As the main product of hydration of cement-based cementitious materials, C-S-H, the change of water content makes its internal structure partially irreversible, which inevitably affects the permeability. In addition, C-S-H becomes the dominant factor controlling water permeability at very low saturation [78-79]. In the past decade, most of the research in the laboratory has focused on the ion transport in saturated cement-based materials. However, the on-site concrete structure is rarely saturated in the actual use environment, so the ion transport is a water dependent process. Therefore, it is very important for us to study the ion transport in unsaturated cement-based materials.

6.1 Experimental research status of unsaturated transport of water molecules and ions in C-S-H / GO

For the ion migration mechanism of saturated cementitious materials, scholars have almost studied it on the basis of Fick's second law. However, these assumptions are not tenable in reality. Therefore, more and more scholars propose amendments to these assumptions and multi-scale experimental and simulation studies. L. Homan et al.[80] analyzed the influence of water transport on chloride ion penetration in partially saturated and fully saturated concrete. The results confirm the coupling effect between water transport and chloride penetration in concrete. Z. Liu et al.[81] studied the transport characteristics of multi-component ions in the pores of C-S-H in saturated state through molecular dynamics simulation. They found that the calcium silicon ratio had a significant impact on the adsorption of chloride ions on the surface of C-S-H. And the adsorption was strongest when the calcium silicon ratio was 1.2.

For the ion migration mechanism of unsaturated cementitious materials, some scholars still use Fick's second law to study. But some scholars considered diffusion and convection separately. They believed that chloride ions were transported by convection at a certain depth of the concrete surface when they were transported in the form of diffusion beyond this depth[82]. E.P. Nielsen [83] analyzed the transport process of chloride ions according to the Fick's law. He attributed all the effects caused by convection effects to the chloride diffusion coefficient. A. Ayman [84] deduced the chloride ion transport equation considering convection effect. However, the convection term ignores the chloride concentration gradient. So the governing equation does not strictly satisfy the law of conservation of matter. Y. Zhang [85] obtained the multi-component partial differential equation of chloride ion transport process under the dry wet cycle. It uses saturation as the driving force of water diffusion which is complicated to determine the boundary conditions, so it is not conducive to practical application.

And many experiments have focused on ion diffusion or capillary adsorption of saline solutions in C-S-H pore channels. They use nuclear magnetic resonance technology or quasi elastic neutron scattering technology to study the water in the pore channel, analyze its mobility, and divide it into chemically bound water, physically adsorbed water and capillary water according to the results. P. Yu and R.J. Kirkpatrick [86] studied the kinetic characteristics of chloride binding on C-S-H mineral analogues in contact with chloride aqueous solution using NMR relaxation method, thus proving the weak chloride ion binding ability of C-S-H surface. D.S. Hou et al. [87] also concluded that the adsorption capacity of chloride ions on C-S-H channels is weak, and found that chloride ions can be indirectly adsorbed through the adsorbed cations.

However, most of the studies on the unsaturated transport of water molecules and ions are based on macroscopic experiments or theoretical formulas, so it is difficult to find the microscopic mechanism of the transport characteristics of water molecules and ions. Therefore, it is very necessary to establish the C-S-H / GO model with MD to study the unsaturated transport of water molecules and ions, which provides a considerable basis for the durability design of concrete.

6.2 MD theory and model of C-S-H / GO

At present, the experimental and theoretical research on water and ion transport at the macro level has been relatively mature, and the research on the micro mechanism is relatively small. However, to explore the reaction and characteristics between material atoms from the microscopic scale will help us to understand the essence of things more deeply, and then better guide the development of concrete. Therefore, research on the microscopic mechanisms of concrete has received increasing attention in recent years [88].

X.Y. Wang et al. [89] established theoretical diffusion equations in saturated, unsaturated and dry states by using Fick's theorem and mass balance equation; J.Y. Sun [90] studied the transmission law of water in unsaturated concrete, and carried out numerical analysis and calculation on the transmission law of water when the concrete is capillary water absorption. The transport properties of water molecules and erosion ions in C-S-H using MD were investigated by D.S. Hou et al. [91]. The findings demonstrate that water molecules move at a faster pace than ions do, and the penetration depth of ions is positively related to the pore size of C-S-H nanoparticles.

With the rapid development of high-performance computing equipment, it is feasible to simulate the amorphous C-S-H on the molecular scale by MD, which can not only determine the performance change mechanism of cement concrete subjected to ion and water molecule erosion and destruction at the same scale, but also make it possible to design the material structure and predict the performance at the molecular scale, So as to realize the multi-scale modeling of GO / C-S-H and the integrated research of microstructure / ion control / performance in complex environment.

M. Wang et al. [92] proposed a three-dimensional mechanism model of GO functional group structure regulating hydration products and microstructure. The model believes that GO is connected into a three-dimensional network structure from the vertical and horizontal directions, and then - COOH at the edge of GO and Ca $^{2+}$ of hydration product $Ca(OH)_2$ form COO-CA-OOC to connect the three-dimensional network structure. At the same time, the hydration product is further inserted into the three-dimensional structure to compact the microstructure, Realize the regulation of GO functional groups on the interface of cement-based composites. In another work, D.S. Hou [93] et al found through reaction force field MD that the hydroxyl and carboxyl groups of GO provided a large number of oxygen sites to accept hydrogen bonds and bind with adjacent sodium ions, thereby fixing water molecules and ions on the GO surface. GO-COOH is deeply rooted in C-S-H, further blocking the connectivity of transport channels and "cage" water and ions in the entrance region of gel pores. In addition, W.L. Jin et al. [94] established a theoretical model of chloride ion transport in partially saturated concrete by considering the time of dry wet cycle, the initial saturation of pores and the saturation of surface layer during drying, and verified the reliability of the model through experiments.

Therefore, it is of great theoretical significance and engineering application value to deeply study the dynamic evolution of ions and water molecules in GO / C-S-H nanochannels. It is also significant to investigate the influence of interface bonding strength, structural stability, surface / interface chemical state and mechanical properties through configuration design and MD theroy.

6.3 Unsaturated transport mechanism of ions and water molecules in nanopores

C-S-H has micro/nano pores, including small gel pores (5 ～ 100 Å) and capillary pores (＞ 100 Å). Some water molecules are changed during the cement hydration step into chemically bonded water, which is then closely associated with the C-S-H layer through the development of Ca-OH and Si-OH connections. The remaining water molecules are used to fill the gel pores and pores. A significant number of sodium, potassium, calcium, and hydroxide ions are released from the cement as the chemical reaction progresses and are intensely concentrated in the nanopores. Meanwhile, due to the strong interaction between water and silicate oxygen atoms, the water molecules adsorbed on the C-S-H surface have higher bulk density, orientation preference and lower diffusivity. In addition, the transport of water and ions in the channels is also affected by slip effect, dynamic contact angle and effective viscosity.

Y. T. Jia et al.[95] employed MS to study the water and ions in the unsaturated and saturated C-S-H channels. Their results show that the transport of water molecules in saturated state is mainly an interactive transport process formed by the mutual diffusion of upper and lower water molecules, which slows down the diffusion speed of water molecules in solution along the channel. So the invasion speed of ions carried is slower than that in unsaturated state. Because of the large number of water molecules, the restriction effect of other water molecules filled in the pores makes the hydration film at the interface more compact and stable, which also increases the retention time of ions at the interface. This strong interaction makes chloride ions firmly adsorbed on the pore surface. At the same time, it can further attract sodium ions and grow into large ion clusters. Because the width of the pore is limited, this kind of ion clusters formed on the surface combine with the ion clusters in the solution to prevent subsequent water molecules and ions from entering. Thus, the transport speed of water molecules and ions is too slow and the number of ions entering the channel is too small.

Besides, their results also prove that the transport of water molecules and ions in the unsaturated state is mainly driven by capillarity. Water molecules are transmitted in the form of meniscus along the C-S-H channel interface, which is consistent with the actually observed capillary absorption phenomenon. At the same time, the transmission speed of water molecules and ions is faster than that in the saturated state.

In terms of dynamics, due to the adsorption of ions at the pore interface and the formation of ion clusters, the movement speed of water molecules in the unsaturated state is stronger than that of ions. Silicate links on the surface of C-S-H can provide non bridged oxygen sites to connect with sodium ions, and calcium ions on the surface of C-S-H can capture chloride ions to form ion pairs. The strong interaction between sodium ions and the interface makes the long-term retention of sodium ions lead to the surface shedding of calcium ions to form ion clusters in the solution. If the ion cluster is too large, it can block the nanochannel and prevent the invasion of water molecules and ions.

When GO is added to C-S-H, the flow velocity of the fluid in the C-S-H nanochannel largely depends on the type of functional groups embedded in the coated plate on the inner surface of C-S-H. The hydroxyl and carboxyl groups in the graphene oxide sheet provide enough oxygen sites to accept hydrogen bonds and bind to the adjacent sodium ions, thus effectively resisting the entry of water molecules and ions. In particular, the surface calcium atoms in the C-S-H play a dominant role in connecting the non bridged oxygen sites and oxygen functional groups in the silicate chain in the graphene oxide sheet, which enhances the chemical bond at the interface. The carboxyl groups on the GO further blocks the connectivity of the transport channel and condenses the water and ions in the inlet area of the gel hole.

Graphene oxide sheets separate from the surface of C-S-H as a result of the van der Waals interaction between GO and C-S-H being greatly weakened by the entry of ions and water molecules. Water and ions are barely repelled by the divided graphene oxide sheets.

In addition, the graphene oxide sheet slows down the intrusion of ions and water in C-S-H pore through the cage effect. With the increase of gel pore size, the effect will gradually weaken, and the fixation effect caused by the attraction of GO plays a major role in resisting the invasion of water molecules and ions.

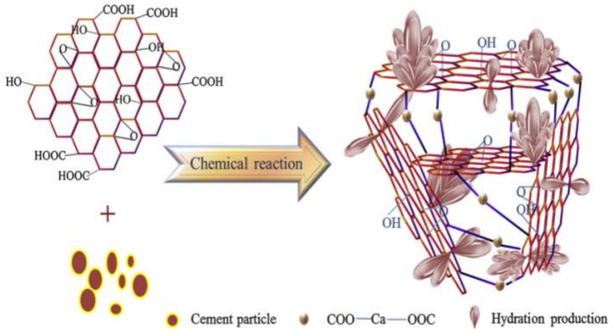

Figure 7 model of GO regulating hydration products and microstructure [92]

Due to the coupling and fixation between the two interfaces of C-S-H nanopore, a transition zone with slow migration speed is formed at the entrance of the pore. The existence of the transition zone can well inhibit the intrusion of ions with large hydration layer. Therefore, the pore diameter of C-S-H can be less than 2nm, which has a certain filtering effect on water molecules and ions. At the same time, harmless ions can also be added to C-S-H to make it grow into larger ion water clusters, preventing the invasion of other water molecules and ions. In this way, the transport of ions can be regulated from the microstructure so that C-S-H can obtain good strength and durability.

7 Conclusion and future prospects

This paper mainly introduces the influence of the environment on the durability of concrete and the two new concrete materials, C-S-H and GO, and also introduces the relevant characteristics of studying the unsaturated transport of water molecules and ions in C-S-H / GO from the nano and micro scale by MD.

GO has strong universality, but its output is low. So GO is expensive and cannot be widely used in practice now. Many researchers have proposed some improved methods. E. Siegfried et al.[96] reduced the production of CO_2 by keeping the reaction temperature at 0~10℃ and prolonging the oxidation time. In this way, GO with fewer defects is obtained. L. Peng et al.[97] used strong oxidant K_2FeO_4 instead of $KMnO_4$ to prepare GO, which can avoid the introduction of polluting heavy metals and the generation of toxic gases in the preparation process. This method can also recover sulfuric acid, which is a safe, efficient and low-cost environmental protection method. Therefore, high-quality and more GO products can be prepared at the same cost with the continuous optimization of GO preparation technology in the future. And the price of GO will gradually decrease, which can be widely used in actual projects.

In the past, the research on water and ion transport of C-S-H/GO in unsaturated environment mainly used micro scale or macro scale single scale. Moreover, the research mainly focuses on the influence of a single erosive ion on unsaturated transport. So the research still needs to be improved in many aspects. The following aspects can be considered:

(1) The MD simulation of C-S-H / GO model still has some limitations and does not fully reflect the uncertainty of C-S-H and GO structure. If we can build mesoscopic and even macroscopic models, we can better realize the confirmation and connection between simulation and experiment.

(2) The dispersion of cement-based materials strengthened by nano materials has always been one of the core issues. When the mixing amount of GO is faced with a large number of concrete materials, the mechanism efficiency may be too low and it is difficult to effectively disperse GO. Therefore, it is necessary to study and formulate large-scale GO dispersion technology to ensure that GO can be fully improved.

(3) In real life, natural electric fields exist in the ocean and other environments. Under the action of electric fields, water molecules and ions will be affected accordingly. Therefore, it is necessary to further study the unsaturated transport of water molecules and ions in C-S-H / GO under the action of electric field.

(4) The varied interface structure, complex solid-solid and liquid-solid interface interactions in C-S-H/GO limit the microscopic study. So it is necessary to study the local interface of C-S-H/GO to analyze the role of GO in C-S-H.

(5) Since there are many kinds of ions invading into

C-S-H, and there may be certain mutual reactions between them, it is necessary to consider the invasion depth and influence of different ions in unsaturated transport.

(6) There are actually three zones (saturated zone, transition zone and unsaturated zone) in unsaturated cementitious materials, which also affect the unsaturated transport of water molecules and ions. Therefore, it is necessary to consider the interaction between saturated zone, transition zone and unsaturated zone.

Supplementary notes:

Figure 3:

Atmospheric area: This area is affected by sea salt particles and land atmosphere.

Splash area: In this area, the dry and wet environment caused by seawater splash and the temperature rise caused by sunlight form the most serious corrosion environment.

Tidal range area: This area is affected by sea tide.

Total immersion area: In this area, the corrosiveness of seawater is mainly affected by dissolved oxygen, flow rate, temperature, salinity, pH value, pollution factors and biological factors.

Sea Mud Area: In this area, dissolved oxygen, temperature and the role of anaerobic organisms are the main factors affecting corrosivity.

Declaration of competing interest

No potential conflict of interest was reported by the authors.

Acknowledgments

This work was supported by a Doctoral program of Zhejiang University of science and technology (F701104L08).

References

[1] G. Wang, Y. Wang, W. Lu, et al.. XFEM based seismic potential failure mode analysis of concrete gravity dam water-foundation systems through incremental dynamic analysis. Engineer Structures, 2015 (98): 81–94.

[2] Y.F. Fan, S.Y Zhang, Q. Wang, et al.. The effects of nano-calcined kaoliniteclay on cement mortar exposed to acid deposits. Construction and Building Materials. 2016(102): 486–495.

[3] C. Wang, C. Yang, F. Liu, et al.. Preparation of Ultra-High Performance Concrete with common technology and materials. Cement and Concrete Composites. 2012(34): 538–544.

[4] T. Kamile. The effect of C3A content on sulfate durability of Portland limestone cement mortars. Construction and Building Materials. 2012(36): 437–447.

[5] E.A. Keller. Introduction to Environmental Geology, Prentice Hall, New Jersey,USA, 2012.

[6] S. Zhao, W. Sun. Nano-mechanical behavior of a green ultra-high performance concrete. Construction and Building Materials. 2014(63): 150–160.

[7] B.L. Hu. Clear Water, Blue Skies: China’s Environment in the New Century.Washington D.C.: The World Bank, 1997.

[8] B.G. Ma, J. Xiao, W. Kai. Effects of slag cement concrete to anti-acid rain performance. Concrete. 2009(4): 5–7.

[9] J.L. Shang. Civil engineering materials.China Building Materials Industry Press. 2010(11): 108.

[10] Z.C. Lu. Analysis on the influence rule and mechanism of different functional groups of organic additives on cement hydration. Tsinghua University, 2017.

[11] M. Devasena, J. Karthikeyan. Investigation on strength properties of graphene oxide concrete. International journal of engineering science invention research and development. 2015(1): 307-310.

[12] S.D. Xie, L. Qi, D. Zhou. Investigation of the effects of acid rain on the deterioration of cement concrete using accelerated tests established in laboratory. Atmospheric Environment. 2004(38): 4457–4466.

[13] J. Haufe, A. Vollpracht. Tensile strength of concrete exposed to sulfate attack. Cement and Concrete Research. 116 (2019) 81–88.

[14] Y.F. Fan, Z.Q. Hu, Y.Z. Zhang, et al.. Deterioration of compressive property of concrete under simulated acid rain environment. Construction and Building Materials. 2010(24): 1975–1983.

[15] P. Vargas, N.A. Marin, J.I. Tobon. Performance and microstructural analysis of lightweight concrete blended with nanosilica under sulfate attack. Advances in Civil Engineering. 2018(1) :2715474.

[16] H. Okochi, H. Kameda, S.I. Hasegawa, et al.. Deterioration of concrete structures by acid deposition—an assessment of the role of rainwater on deterioration by laboratory and field exposure experiments using mortarspecimens. Atmospheric Environment.2000(34): 2937–2945.

[17] M. Zhang, L.M. Yang, J.J. Guo, et al.. Mechanical properties and service life prediction of modified concrete attacked by sulfate corrosion. Advances in Civil Engineering. 2018(1): 8907363.

[18] B.X. Li, L.H. Cai, K. Wang, et al.. Prediction of the residual strength for durability failure of concrete structure in acidic environments. Journal of Wuhan University of technology - Materials Science.2016(31): 340–344.

[19] R. Wang, Z. Tao, Y. Li. Evaluation of microcrack size in rubber concrete ITZ exposed to sulfate attack, J. Materials in Civil Engineering. 2019(31): 04019308.

[20] R. Dhole, M.D.A. Thomas, K.J. Folliard, et al.. Chemical and physical sulfate attack on fly ash concrete mixtures. Aci Materials Journal. 2019(116): 31–42.

[21] S.L. Gao, J.P. Jin, G.H. Hu, et al.. Experimental investigation of the interface bond properties between SHCC and concrete under sulfate attack. Construction and Building Materials. 2019(217): 651–663.

[22] X.L. Yuan, B.X. Li, W.K. Zhu, et al.. Corrosion Mechanism of Acid Rain on the Surface Structure of Concrete. Materials Reports. 2022(36): 20120006.

[23] M.F. Funari, S. Spadea, F. Fabbrocino, et al.. A moving interface finite element formulation to predict dynamic edge debonding in FRP-Strengthened concrete beams in

service conditions. Fibers. 2020(8): 42.

[24] O. Rabinovitch. Cohesive interface modeling of debonding failure in FRP strengthened beams. Journal of Engineering Mechanics. 2008(134): 578–588.

[25] T. Han, W.H. Yang, Z.J. Yang, et al.. Monitoring study of shaft lining concrete strain in freezing water-bearing soft rock during mine shaft construction period in west China. Procedia Engineering. 2011(26): 992-1000.

[26] R. Wang, Y. Li, Y. Li, et al.. Influence of Water Pressure on the Mechanical Properties of Concrete after Freeze-Thaw Attack under Dynamic Triaxial Compression State. Advances in Materials Science and Engineering. 2019(1): 8702324.

[27] Z.L. L, S.L. Du. Experimental study on mechanical properties of concrete due to high seepage pore water pressure. Engineering Mechanics. 2011(28): 72–77.

[28] Q. Wang, Y. Liu, G. Peng. Effect of water pressure on mechanical behavior of concrete under dynamic compression state.Construction and Building Materials. 2016(125): 501–509.

[29] J. Cui, H. Hao, Y. Shi. Study of concrete damage mechanism under hydrostatic pressure by numerical simulations. Construction and Building Materials. 2018(160): 440–449.

[30] Y. Karinski, D. Yankelevsky, S. Zhutovsky, et al.. Uniaxial confined compression tests of cementitious materials. Construction and Building Materials. 2017(153): 247–260.

[31] W. Xue, Z. Yao, W. Jing, et al.. Mechanical damage and failure behavior of shaft-lining concrete after exposure to high pore-water pressure. Journal of Materials in Civil Engineering. 2020(32): 04019339.

[32] J. Cui, H. Hao, Y. Shi, et al.. Experimental study of concrete damage under high hydrostatic pressure. Cement and Concrete Research. 2017(100): 140–152.

[33] A.M. Ragab, M.A. Elgammal, O.A. Hodhod, et al.. Evaluation of field concrete deterioration under real conditions of seawater attack. Construction and Building Materials. 2016(119): 130–144.

[34] M.M. Islam, M.S. Islam, M. Al-Amin, et al.. Suitability of sea water on curing and compressive strength of structural concrete.Journal of Materials in Civil Engineering. 2012(40): 37–45.

[35] A. el Mahdi Safhi, M. Benzerzour, P. Rivard, N.E. Abriak, I. Ennahal. Development of self-compacting mortars based on treated marine sediments. Journal of Building Engineering. 2029(22): 252–261.

[36] F.M. Wegian. Effect of seawater for mixing and curing on structural concrete.IES Journal Part A: Civil and Structural Engineering. 2010(3): 235–243.

[37] R.A. Medeiros-Junior, M.G. Lima, P.C. Brito, et al.. Chloride penetration into concrete in an offshore platform-analysis of exposure conditions, Ocean Engineering. 2015(103): 78–87.

[38] R.R. Hussain, T. Ishida. Influence of connectivity of concrete pores and associated diffusion of oxygen on corrosion of steel under high humidity, Construct. Build. Mater. 2010(24 (2010): 1014–1019.

[39] Q. Yuan, C. Shi, G. De Schutter, et al.. Chloride binding of cement-based materials subjected to external chloride environment–a review. Construction and Building Materials. 2009(23): 1–13.

[40] R. Yu, P. Spiesz, H.J.H. Brouwers. Effect of nano-silica on the hydration and microstructure development of Ultra-High Performance Concrete (UHPC) with a low binder amount. Construction and Building Materials. 2014(65): 140–150.

[41] X.M. Gong, X.J. Zou, D.B. Liu, et al..Research progress of concrete durability in marine environment.New century cement Guide. 2014(20): 21-24.

[42] J.Q. Li.Ions penetration and reaction in concrete exposed to different corrosion zones in marine environment.Qingdao University of Technology, 2016.

[43] H.F Yuan, P. Dangla, P. Chatellier, et al.. Degradation modelling of concrete submitted to sulfuric acid attack. Cement and Concrete Research. 2013(53): 267–277.

[44] H. Siad, M. Lachemi, M. Sahmaran, et al.. Effect of glass powder on sulfuric acid resistance of cementitious materials. Construction and Building Materials. 113 (2016) 163–173.

[45] F. Girardi, R.D. Maggio. Resistance of concrete mixtures to cyclic sulfuric acid exposure and mixed sulfates: Effect of the type of aggregate. Cement and Concrete Composites. 2011(33): 276–285.

[46] M. Mahdikhani, O. Bamshad, M.F. Shirvani. Mechanical properties and durability of concrete specimens containing nano silica in sulfuric acid rain condition. Construction and Building Materials. 2018(167): 929–935.

[47] J.J. Guo, K. Wang, T. Guo, et al.. Effect of dry-wet ratio on properties of concrete under sulfate attack. Materials. 2019(12): 2755.

[48] H. Siad, M. Lachemi, M. Sahmaran, et al.. Preconditioning method for accelerated testing of concrete under sulfate attack. ACI Materials Journal. 2016(113): 493-504.

[49] J.M. Gao, Z.X. Yu, L.G. Song, et al.. Durability of concrete exposed to sulfate attack under flexural loading and drying-wetting cycles. Construction and Building Materials. 2013(39): 33–38.

[50] H. Fazli, A.Y. Mohd Yassin, N. Shafiq, et al.. Pull-off testing as an interfacial bond strength assessment of CFRP-concrete interface exposed to a marine environment. International Journal of Adhesion and Adhesives. 2018(84): 335 .

[51] W.H. Hu ; Peng, G.; Zou, S.B.; Liang, H. A comparative analysis of damage characteristics of concrete under natural and water-saturated states. China Rural Water Hydropower. 2014(393): 115–121.

[52] C. Poinard, Y. Malecot, L. Daudevile. Damage of concrete in a very high stress state: Experimental investigation. Materials and Structures. 2010(43): 15–29.

[53] Y.T. Jia. Research on unsaturated transport of water and ions in cement-based materials based on molecular dynamics. Qingdao University of Technology . 2018.

[54] W. Xu, P. Lan, Y. Jiang, D. Lei, et al.. Insights into excluded volume and percolation of soft interphase and conductivity of carbon fibrous composites with core-shell networks. Carbon. 2020(161): 392–402.

[55] K. Celik, C. Meral, A. Petek Gursel, et al.. Mechanical properties, durability, and life-cycle assessment of self-consolidating concrete mixtures made with blended portland cements containing fly ash and limestone powder. Cement and Concrete Composites. 2015(56): 59–72.

[56] Z. Gong, Y. Wu, Z. Zhu, et al.. DEM and dual-probability-Brownian motion scheme for thermal conductivity of multiphase granular materials with densely packed non-spherical particles and soft interphase networks. Computer Methods in Applied Mechanics and Engineering. 2020(372): 113372.

[57] D. Hou, W. Zhang, M. Sun, et al.. Modified lucas-washburn function of capillary transport in the calcium silicate hydrate gel pore: a coarse-grained molecular dynamics study. Cement and Concrete Research. 2020(136): 106166.

[58] P.A. Bonnaud, Q.JI, B. Coasne, et al. Thermodynamics of water confined in porous calcium-silicate-hydrates. Langmuir. 2012(28): 11422-11432.

[59] N. Giovambattista, P.J. Rossky, P.G. Debenedetti. Effect of pressure on the phase behavior and structure of water confined between nanoscale hydrophobic and hydrophilic plates. Physical Review E. 2006(73): 041604.

[60] M.J.A. Qomi, M. Bauchy, F.J. Ulm, et al.. Anomalous composition-dependent dynamics of nanoconfined water in the interlayer of disordered calcium-silicates. Journal of Chemical Physics. 2014(140): 054515.

[61] M. Youssef, R.M. Pellenq, B. Yildiz. Glassy nature of water in an ultraconfining disordered material: the case of calcium-silicate-hydrate. Journal of the American Chemical Society. 2011(133): 2499–2510.

[62] D.S. Hou, Z. Li. Molecular dynamics study of water and ions transport in nano-pore of layered structure: a case study of Tobermorite. Microporous Mesoporous Materials. 2014(195): 9–20.

[63] A. Lerf , H. He, M. Forster, et al. Structure of Graphite Oxide Revisited. The Journal of Physical Chemistry B. 1998(102): 4477-4482.

[64] A.M. Dimiev, L.B. Alemany, J.M. Tour. Graphene Oxide. Origin of Acidity, Its Instability in Water, and a New Dynamic Structural Model. Acs Nano. 2013(7): 576-588.

[65] J.P. Rourke, P.A. Pandey, J.J Moore, et al. The Real Graphene Oxide Revealed: Stripping the Oxidative Debris from the Graphene-like Sheets. Angewandte Chemie-International Edition. 2011(50): 3173-3177.

[66] Y. Zhu, S. Murali, W. Cai, X. Li, J.W. Suk, J.R. Potts, R.S. Ruoff. Graphene and graphene oxide: synthesis, properties, and applications. Advanced Materials. 2010(22): 3906–3924.

[67] D.A. Dikin, S. Stankovich, E.J. Zimney, R.D. Piner, G.H.B. Dommett, G. Evmenenko, S.T. Nguyen, R.S. Ruoff, Preparation and characterization of graphene oxide paper. Nature. 2007(448): 457–460.

[68] A. Mohammed, J.G. Sanjayan, W.H. Duan, A. Nazari, Incorporating graphene oxide in cement composites: a study of transport properties. Construction and Building Materials. 2015(84): 341–347.

[69] C.D. Sanglakpam , A.K. Rizwan .Influence of graphene oxide on sulfate attack and carbonation of concrete containing recycled concrete aggregate. Construction and Building Materials. 2020(250): 118883.

[70] R.R. Bellum, K. Muniraj, C.S. Reddy Indukuri, S.R. Chand Madduri. Investigation on Performance Enhancement of Fly ash-GGBFS Based Graphene Geopolymer Concrete. Journal of Building Engineering. 2020(32): 101659.

[71] S. Lv ,Y. Ma, C. Qiu, et al. Effect of graphene oxide nano-sheets of microstructure and mechanical properties of cement composites .Construction and Building Materials. 2013(49): 121-127．

[72] W.L. Yang, Y.S. Zhang, Z.Y. Zhao. Effect of graphene oxide on slag grinding process and properties of cement concrete. Cement. 2018(6): 6-9.

[73] B.Y. Ma，T.J. Yang, C.J Pan, D.S. Hou. Simulation Study on Interfacial Properties of Graphene Oxide Modified Cement Materials with Different Water Content. Bulletin of the Chinese Ceramic Society. 2020(39): 7.

[74] S. Sharma. N.C.Kothiyal. Influence of graphene oxide as dispersed phase in cement mortar matrix in defining the crystal patterns of cement hydrates and its effect on mechanical, microstructural and crystallization properties. Rsc Advances. 2015(65): 52642-52657.

[75] Q. Wang, J. Wang.Influence of graphene oxide additions on the microstructure and mechanical strength of cement.New Carbon Materials. 2015(30): 349-356.

[76] B. Fakhim, A. HAssani, A. Rashidi, et al. Preparation and Mechanical Properties of Graphene oxide:Cement Nanocomposites .Scientific world journal. 2014(4): 276-323.

[77] S. Lv , Y.J. Ma ,C.C. Qiu, et al. Regulation of GO on cement hydration crystals and its toughening effect. Journal of Functional Materials. 2013(6): 1245-1253.

[78] Z.Y. Liu, Y.C. Wang, D. Xu, C.Y. Zang , Y.S. Zhang, J.Y. Jiang. Multiple ions transport and interaction in calcium silicate hydrate gel nanopores: Effects of saturation and tortuosity. Construction and Building Materials. 2021(283): 122638.

[79] K. Li, L. Xu, P. Stroeven , C.J. Shi. Water permeability of unsaturated cementitious materials: A review. Construction and Building Materials. 2021(302): 124168.

[80] L. Homan, A.N. Ababneh, Y. Xi. The effect of moisture transport on chloride penetration in concrete. Construction and Building Materials. 2016(155): 1189-1195.

[81] Z. Liu, D. Xu, S. Gao, et al. Assessing the adsorption and diffusion behavior of multicomponent ions in saturated calcium silicate hydrate gel pores using molecular dynamics. ACS Sustainable Chemistry and Engineering. 2020(8): 3718-3727.

[82] L. Z. Jia. Y. Z. Zhang. K. Y. wang, et al.Chloride transport mechanism in unsaturated concrete. Journal of Building Materials. 2016(19): 45-52

[83] E.P. Nielsen. M. R. Geiker. Chloride diffusion in partially saturated cementitious material. Cement and Concrete Research.2003(33): 133.

[84] A. Ayman. B. Farid. Y.P. Xi. Chloride penetration in nonsaturated concrete. Journal of Materials in Civil Engineering.2003(15): 183.

[85] Y. Zhang.Mechanics of chloride ions transportation in concrete.Zhejiang University,2008.

[86] P. Yu, R.J. Kirkpatrick. 35Cl NMR relaxation study of cement hydrate suspensions. Cement and Concrete Research. 2001(31): 1479–1485.

[87] Y. Zhou, D.S. Hou, J. Jiang, et al. Chloride ions transport and adsorption in the nano-pores of silicate calcium hydrate: Experimental and molecular dynamics studies. Construction and Building Materials. 2016(12): 991-1001.

[88] D.S. Hou, Y. Jia, J. Yu, P. Wang, Q. Liu, Transport Properties of Sulfate and Chloride Ions Confined Between Calcium Silicate Hydrate Surfaces: A Molecular Dynamics Study. The Journal of Physical Chemistry. 2018(122): 28021–28032.

[89] X.Y. Wang, Z.W Jiang. Review on mechanism and model of water transport in concrete. Journal of Building Materials. 2002(5): 67-71.

[90] J.Y. Sun, N.G. Jin, Y. Tian, X.Y. Jin. Experiment study of capillary absorption of fly ash concrete at different curing ages. Advanced Materials Research. 2012(451): 78-81.

[91] D.S. Hou, D.K. Li, J. Yu, et al. Insights on capillary adsorption of aqueous sodium chloride solution in the nanometer calcium silicate channel: A molecular dynamics study. Journal of Physical Chemistry C. 2017(121): 13786-13797.

[92] M. Wang , R.M. Wang, H. Yao, et al. Study on the three dimensional mechanism of graphene oxide nanosheets modified cement. Construction and Building Materials. 2020(12): 730-739.

[93] D.S. Hou ,Z.Y. Lu,X.Y. Li,H.Y. Ma,Z.J. Li. Reactive molecular dynamics and experimental study of graphene-cement composites: Structure, dynamics and reinforcement mechanisms. Carbon. 2017(115): 188-208.

[94] W.L. Jin, Y. Zhang, Z.Y. Lu. Mechanism and mathematic modeling of chloride permeation in concrete under unsaturated state. Journal of the Chinese Ceramic Society. 2008(36): 1362-1369.

[95] Y. T. Jia. T.J. Zhao. D. S. Hou, et al.Molecular Dynamics Study on Water and Ion Transport in Unsaturated and Saturated Calcium Silicate Hydrate Channels.Silicate Bulletin.2019(38): 615-621.

[96] L. Peng, Z. Xu, Z. Liu, et al.An iron-based green approach to 1-h production of single-layer graphene oxide. Nature Communications. 2015(6): 5716.

[97] E. Siegfried, E. Michael, G. Stefan, et al. Wet chemical synthesis of graphene.Advanced Materials. 2013(25): 3583-3587.

Viser Technology Pte. Ltd.
Research and Application of Materials Science
DOI: 10.33142/rams.v4i1.8458

Research Article Open Access

Study on polyurethane-based porous materials and their adsorption properties

Jiajia LI, Jiahui ZHU, Jialin GU, Zhenhao ZHOU, Qi SUN, Guangcan GUO, Yibin ZHOU, Shujun CHEN, Xinggang SHAN*, Gangqiang WANG*

Keyi College of Zhejiang Sci-Tech University, 58 Kangyang Avenue, Shangyu Economic and Technological Development Zones, Shaoxing 312369, China 5 Boya International Academy Shaoxing, Shaoxing 31200

***Corresponding Author:** Xinggang SHAN (shanxg0601@126.com), Gangqiang Wang (sywgq@163.com)*

Abstract:
The flexible superhydrophobic thermoplastic polyurethane(TPU) porous material was prepared by heat-induced phase separation method with two cooling steps. The influence of the preparation process on the microstructure of the material was discussed in depth. The microstructure, hydrophobicity and specific surface area of porous TPU materials were analyzed in detail. The surface wettability, separation selectivity, saturated adsorption capacity and adsorption rate, mechanical properties, environmental adaptability and cyclic properties of porous TPU materials were studied.The results show that the TPU-8% porous monolithic material prepared by heat-induced phase separation method shows good performance when the polymer concentration is 8%, the phase separation temperature is 0 ℃, the phase separation time is 30min, and the mixing solvent ratio is 9:1.

Keywords: *Polymer-based porous materials; Separation of oil and water; Oil recovery*

1 Introduction

In recent years, frequent oil spills and organic chemical spills around the world have caused almost irreversible damage to ecological environment and human health. How to efficiently and environmentally remove and recycle organic pollutants from polluted water bodies has become a key problem that governments all over the world urgently need to solve, and has attracted wide attention from the scientific community.[1-2]Current methods fall into three broad categories: physical methods (e.g. filtration, flotation and absorption), chemical methods (e.g. dispersion, solids and combustion) and biological methods (e.g. bioremediation).[3-7]Polymer-based porous materials show excellent water absorption and separation properties because of high porosity, large specific surface area and three-dimensional connected porous structure. So it shows excellent water absorption and separation performance. However, the high brittleness of the material leads to its poor durability, which makes it far from practical applications.In this case, the aim of this paper is to develop a sustainable, economical and durable oil-water separation material with efficient and rapidly recyclable oil-absorbing properties that can be used to treat contaminated water.

2 The experiment

2.1 Experimental materials and instrument and equipment

1, 4-dioxane and cyclohexane were purchased from Shanghai Zhanyun Chemical Co., Ltd.The polyurethane was purchased from BASF Co., Ltd.、Electronic balance, constant temperature heating magnetic stirrer, vacuum freeze dryer, ultrasonic cleaner, magnetic stirrer, scanning electron microscope, surface contact Angle measuring instrument, Fourier near infrared spectrometer.

2.2 Preparation of porous polyurethane materials

First, dissolve 8g TPU in a mixture (100ml) of 1, 4-dioxane / deionized water (v/v=9/1) under vigorous magnetic stirring at 60 ℃ for 90 min until becoming a homogeneous

solution.After the initial dissolution, the TPU was further dissolved in an ultrasonic cleaner at 80 ℃, so that the TPU was completely dissolved, and the homogeneous solution of 8% TPU was obtained.The mixture was then quickly transferred to a test tube with 20 mm outside diameter, and the test tube was placed in an ice bath (0 ℃)

Received on April 18, 2022; Accepted on May 24, 2022

for 30 min for preliminary phase separation. Then the tube was moved to the refrigerator (-20℃) for 48h to complete the phase separation. Finally, the tube was put into the freeze dryer (-80℃) for 72h to prepare porous TPU composite.

The experimental conditions were changed to conduct a comparative experiment:T-1(TPU concentration: 4%, separation temperature: 0℃, separation time: 30min, mixing solvent ratio: 9:1),T-2(TPU concentration of 6%, separation temperature of 0℃, separation time of 30min, mixing solvent ratio of 9:1),T-3(TPU concentration: 8%, separation temperature: 0℃, separation time: 30min, mixing solvent ratio: 9:1),T-4(TPU concentration: 10%, separation temperature: 0℃, separation time: 30min, mixing solvent ratio: 9:1).

2.3 Characterization method

Scanning electron microscopy (SEM) was employed to observe the morphology of TPU monoliths, and contact angle (CA) measurements were performed on a Powereach JC2000C instrument at ambient temperature. The size of water droplets was 2μL, and the mode was circle fitting. Fourier infrared spectrometer (FTIR) was used to plot the relevant infrared spectra, and the scanning speed was $1cm^{-1}$, ranging from 650-4000.

2.4 Performance Detection

Take TPU-8% of samples for bending resistance, compression resistance, The physical properties of the samples were tested by weight test, the selective adsorption capacity of the TPU materials for the two typical separation of oil/organic solvent and water mixture was tested, and the stability and environmental adaptability of the samples were tested by the oil-water separation process of the whole TPU-8% material under the strong magnetic stirring simulation of ocean wave motion (-600rpm). Easily remove the oil and organic solvent adsorbed by the sample to test the recycling and recyclability of the sample.

3 Results and discussion

3.1 Characterization of the samples

3.1.1 Morphological analysis

The surface shapes and pore SEM maps at different SEM ratios at various TPU concentrations are shown in Figure 1.As shown in Figure 1,we can see from Figure, The T-1 sample did not present clear hole imaging and showed poor connectivity between holes;The T-2 sample showed a larger pore size and presented as filiform;The T-3 sample showed a three-dimensional connected porous pattern with a wide aperture distribution, showing a hemispherical hollow porous structure;The T-4 sample also showed a porous structure with thick connections between the skeletons.Therefore, when the TPU concentration is low (4-6%), the solution system viscosity is low, the phase separation rate is fast, the pore size grows rapidly and the pore size is large, and the irregular porous morphology, and the gap between 8% and 10% is small.

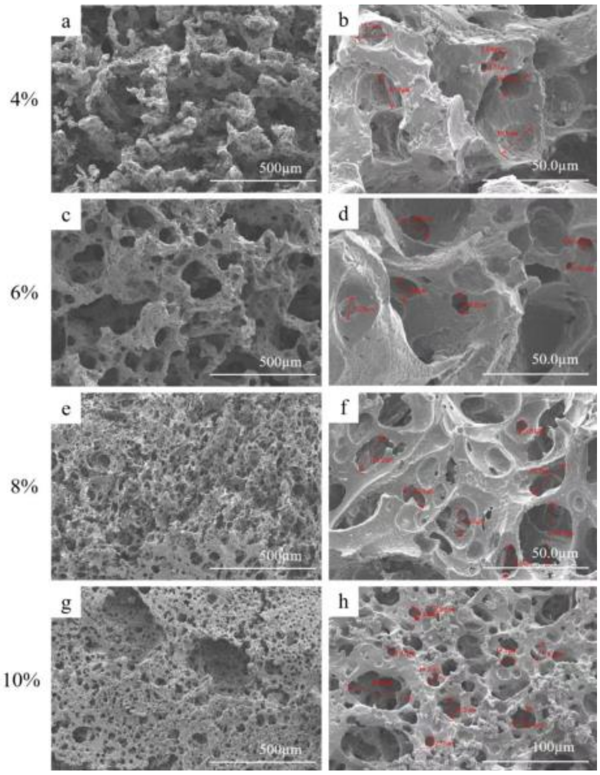

Figure 1 Surface shapes and pores at various TPU concentrations at different multiples of SEM

a:[4%,x100LM] b:[4%,x500LM] c:[6%,x100LM] d:[6%,x500LM] e:[8%,x100LM] f:[8%,x500LM] g:[10%,x100LM] h:[10%,x500LM]

3.1.2 WCA analysis

As shown in Figure 2a, several water droplets (dyed with potassium permanganate) are allowed to remain in astable spherical shape on the cross section of TPU-8% monolith, the water CA (144°) of the monolith reveals highhydrophobicity without any surface treatment. Figure 2b shows the oil wettability of TPU-8% monolith, where a drop of soybean oil (dyed with oil red) is immediately and completely absorbed into the monolith within 1 s once it touches the cross section of the monolith, which suggests that the oil CA is ～0°.

The above phenomena demonstrate the excellent hydrophobicity and superoleophilicity of the porous monolith.

Figure 2c presents the water CA values of the TPU film and porous TPU monoliths with different polymer concentrations.It can be easily observed that all TPU monoliths show hydrophobic property with water CA of ＞120°compared tothe hydrophilic TPU film (water CA of 84°). The maximum CA for TPU-8% monolith is 144°, which is close to superhydrophobicity (150°), reflecting the ultra-highly.drophobicity.

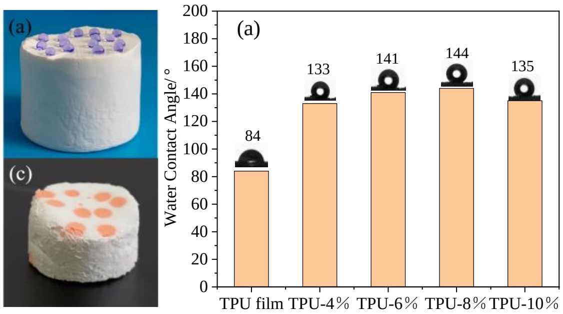

Figure 2 (a) image of water droplets (stained with methyl blue) on the cross section of TPU-8% of the material; (b) droplet angles of TPU and porous TPU, and (c) image of oil (stained with methyl red) on the cross section of TPU-8% of the material

3.1.3 Infrared spectrum analysis

Figure 3 shows the membrane prepared from the TPU-8% of the sample and the raw materials, making the infrared spectrum of the two samples.As shown in Figure 3,1765 – 1729 cm^{-1} as the ether bond, 1718 – 1704 cm-1 as the carboxyl group and 1 690 – 1650 cm^{-1} as the base.The infrared spectrum determined the different functional groups represented by each peak. The peak of this experiment was matched with the raw material and changed, reflecting the stability of the structure of the sample.Among them, 898-1327cm^{-1} is the C-H bending vibration peak, 1243cm^{-1} is the C-O-C vibration, 1505cm^{-1} is the aromatic ring skeleton vibration peak, and 1266cm^{-1} is the C=O expansion vibration.

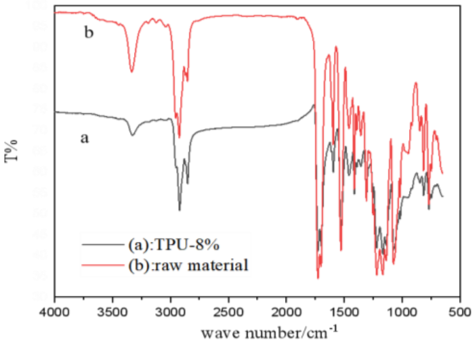

Figure 3 Sample infrared spectrum diagram: (a): TPU-8% solid; (b): raw material

3.2 Performance analysis

3.2.1 Analysis of the physical properties

Figure 4(a) presents after multiple manual bending, the sample can always quickly recover to its original state, reflecting the good bending resistance of the sample.Figure 4(b) presents a 400 g weight was placed for the compression test, and the sample showed good compression resistance.Figure 4(c) presents places the sample on the blade, and the blade is less variable and can be placed upright on the blade, indicating that the sample is relatively light.as illustrated in following figure.[11]

Figure 4 Photo of the TPU-8% material block showing (a) sample bending resistance test, (b) sample compression test, (c) light performance test

Figure 5 presents the curve of absorption capacity (Qt) for vegetable oil as a function of absorption time (t) to evaluate the absorption kinetics of TPU-8% monolith, where vegetable oil was chosen as a representative because of its difficult absorption induced by high viscosity. During testing procedure, the absorption equilibrium state of TPU-8% monolith is quickly reached within 20s, meaning a very rapid oil absorption rate. The absorption rate constant (k) can be obtained from the slope of linear regression plot of ln (Qs − Qt) [8]versus t. The highly consistent fitting result (R2 = 0.979) exhibited in the inset of Figure 3c reveals that the sorption kinetics of the monolith conforms to pseudo-first-order kinetics model with a k value of 6.96 The fast absorption rate of TPU-8% monolith is mainly attributed to its hierarchical interconnected macroporous structure and superoleophilicity.

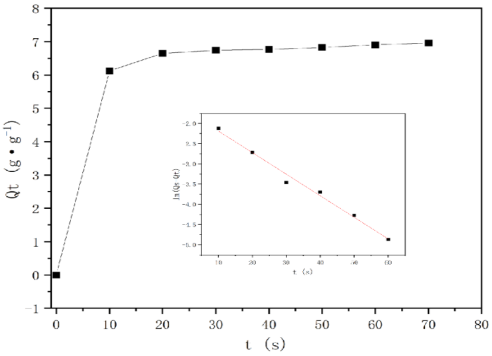

Figure 5 The picture shows the relationship of absorption capacity on adsorption time and the pseudo-first-order kinetic model of vegetable oil absorption by TPU-8% monomer (inset)

As shown in Figure 5, the absorption dynamics of TPU-8% material was evaluated by the function curve of the absorption capacity and absorption time of vegetable oil, among which vegetable oil was selected as a representative due to the difficulty in absorption caused by its high viscosity.During the test process, the TPU-8% material reached an adsorption equilibrium state between 20s and 30s, which means that the oil absorption rate is very fast, with an absorption rate constant of 6.96.The highly consistent fit shown in Figure results in R2=0.979.The rapid absorption rate of the TPU-8% material column is mainly attributed to its macroporous structure and superlipophilicity.[10]

3.2.2 Analysis of saturated adsorption performance

Figure 6 shows the bar graph of the saturated adsorption of TPU-8% monomer. The saturated absorption capacities (Qs) of TPU-8% monolith for different types of oils (vegetable oil, pump oil) and organic solvents (cyclohexane, ethanol, dichloromethane, tetrachloromethane) are shown in Figure 6. All Qs values are in the range of 6.64−35.87 g g−1[12],which are closely related to the viscosity and density of the absorbed oil and organic solvents.[9]

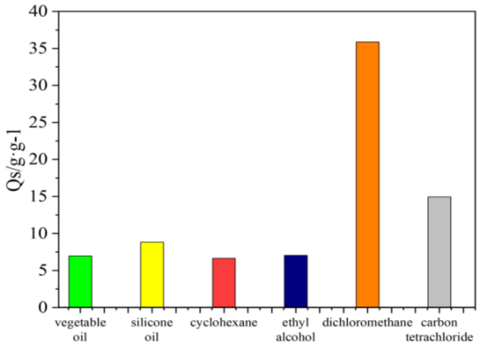

Figure 6 Bar chart of saturated adsorption amount of monomer to oil and organic solvent of TPU-8%

3.2.3 Analysis of stability energy and environmental adaptability energy

Figure 7 shows the oil-water separation process of the TPU-8% material under strong magnetic stirring simulating wave motion (-600rpm).Vegetable oil, suspended in a turbulent oil-water mixture, can be fully absorbed by the porous body within a few seconds, indicating good mechanical stability and environmental adaptability.

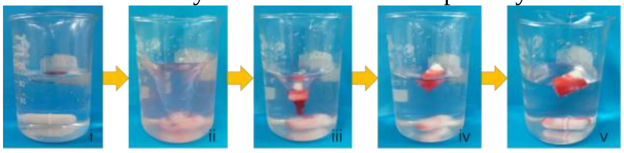

Figure 7 (i-v): The picture shows the separation of pump oil (oil red staining) from water (TPU-8% monomer) under strong magnetic stirring

3.2.4 Analysis of cycle performance and recyclable performance

Figure 8 shows the process of pumping the oil out of the water through the three absorption and extrusion cycles.As shown in Figure. 8, a typical absorption and extrusion process from oil floats or organic solvents in water, in which the floating pump oil can be removed through three cycles of absorption and extrusion processes.

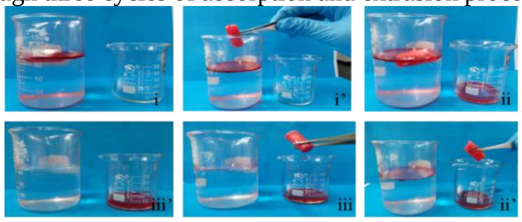

Figure 8 (i - i ’; ii - ii ’;iii-iii’):The picture shows the process of pumping oil out from the water through three absorption and extrusion cycles

Figure 9 shows the line diagram of the saturated adsorption of TPU-8% monomer to vegetable oil by absorption extrusion.As shown in Figure 9, for reused TPU materials of vegetable oils, stable Qs values were shown when tested for 20 cycles, but it is noteworthy that the tested Qs were significantly reduced in the second cycle, because the high viscosity of the oil was difficult to be completely removed by the manual extrusion process.Materials reused in subsequent cycles maintained stable Qs values even by centrifugation and evaporation methods.

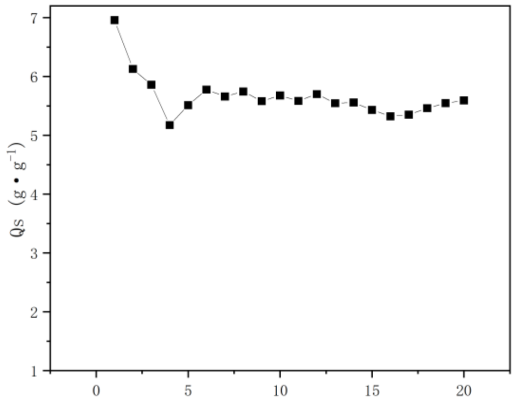

Figure 9 [Line plot of TPU-8% monomer to vegetable oil by absorption and extrusion method]

4 Conclusion

(1) When the polymer concentration was 8%, the phase separation temperature was 0℃, the phase separation time was 30min, and the mixing solvent ratio was 9:1, the TPU-8% porous monolithic material prepared by the heat-induced phase separation method showed good performance.

(2) It can be seen that the overall material at TPU-8% shows good reversible compressibility and fatigue resistance characteristics, showing excellent super elasticity. The environmental adaptability test shows that TPU-8% porous monolithic material has good environmental adaptability in different solvents.

(3) The oil or organic solvent adsorbed by T-3(8%) porous material can be removed by adsorption/extrusion, and the sample can be reused many times, up to 20 or more times, showing better recycling performance and durability.

(4) Three-dimensional TPU-8% material with non-stratified porous structure was successfully prepared by a simple heat-induced phase separation method through two cooling steps.Can effectively absorb various oils and organic solvents from water and greasy. The prepared materials have many excellent properties, such as high saturation absorption capacity, fast absorption rate, excellent mechanical stability and recycling performance.The maximum saturation adsorption capacity of dichloromethane was 35.87 times its own weight, and the TPU-8% material remained intact, returning to its original shape even after the compression release cycle.Therefore, porous TPU materials will be a

promising eco-friendly adsorption material for large-scale removal and collection of petroleum/organic solvent contaminants in water.

Acknowledgements

We acknowledge the fnancial support from the Research Project of Keyi College of Zhejiang Sci-Tech University (KY2021001), the National Natural Science Foundation of Zhejiang Province China (LY15B030002).

References

[1] Ge J, Zhao H Y, Zhu H W, et al. Advanced sorbents for oil-spill cleanup: Recent advances and future perspectives [J]. Advance Materials, 2016(28): 10459-10490.

[2] Wang X L, Pan Y M, Liu X H, et al. Facile fabrication of superhydrophobic and eco-friendly polylactic acid foam for oil-water separation via skin-peeling [J]. ACS Applied Materials & Interfaces, 2019(11): 14362-14367.

[3] Wang S, Peng X W, Zhong L X, et al. An ultralight, elastic, cost-effective, and highly recyclable superabsorbent from microfibrillated cellulose fibers for oil spillage cleanup [J]. Journal of Materials Chemistry A, 2015(3): 8772-8781.

[4] Kujawinski E B, Kido Soule M C, Valentine D L, et al. Fate of dispersants associated with the deepwater horizon oil spill [J].Environmental Science Technology, 2011(45): 1298-1306.

[5] Broje V, Keller A A. Improved mechanical oil spill recovery using an optimized geometry for the skimmer surface [J]. Environmental Science Technology, 2006(40): 7914-7918.

[6] Aurell J, Gullett B K. Aerostat sampling of PCDD/PCDF emissions from the gulf oil spill in situ burns [J]. Environmental Science Technology, 2010(44): 9431-9437.

[7] Bayat A, Aghamiri S F, Moheb A, et al. Oil spill cleanup from Bi H C, Xie X, Yin K B, et al. Spongy graphene as a highly efficient and recyclable sorbent for oils and organic solvents [J]. Advanced Functional Materials, 2012(22): 4421-4425.

[8] Azizian, S. Kinetic Models of Sorption: a Theoretical Analysis.[J]. Colloid Interface Sci. 2004(276): 47−52.

[9] Wang H, Wang E, Liu Z, Gao D, Yuan R, Sun L, Zhu Y.A novel carbon nanotubes reinforced superhydrophobic and superoleophilic polyurethane sponge for selective oil/water separation through a chemical fabrication. [J]. Mater. Chem. 2015(3): 266−273.

[10] Wu Y, Xue S, Yang H, Zhang H, Zhang T,Gou S.Polymerization-Induced Phase Separation for the Fabrication of Magnetic Sponges for Oil Spill Reclamation. Chem. Eng. [J]. 2017(328): 639−644.

[11] Cao N, Yang B, Barras A, et al. Polyurethane sponge functionalized with superhydrophobic nanodiamond particles for efficient oil/water separation [J]. Chemical Engineering Journal, 2017(370): 319-325.

[12] He Y Q, Liu Y, Wu T, et al. An environmentally friendly method for the fabrication of reduced graphene oxide foam with a super oil absorption capacity [J]. Journal of Hazardous Materials, 2013(260): 796-805.

Viser Technology Pte. Ltd.
Research and Application of Materials Science
DOI: 10.33142/rams.v4i1.8459

Research Article Open Access

Portable solar billboard

Fangyue ZHAO, Xinhua YI*, jia CAI, Weishi MA, Boyan LIU, Xinru LI, Yansong MENG

School of Materials Science and Engineering, Yingkou University of Technology 115014

***Corresponding Author:** Xinhua YI, E-mail addresses: 290440492@qq.com*

Abstract:
Public bulletin boards are widely used in various public places, but due to the large size of the billboards, it is not easy to carry, and the traditional billboards are integrated, when the billboards need to be transferred, the limited storage space of the vehicle needs to be occupied It is extremely inconvenient, and at night, the traditional bulletin boards need to install additional light sources to illuminate them, which greatly increases energy consumption. Based on this paper designed a new structure of the bulletin board, this structure can make the bulletin board when not in use completely folded up and easy to carry, and in use can be completely unfolded and in the bottom of the added retractable support leg structure can be placed anywhere, and according to the terrain or human will to adjust the height. A solar panel is placed on the top of the bulletin board, which can store solar energy during the day and supply energy to the LED lights on the top at night for lighting, which saves energy and is very environmentally friendly.

Keywords: *Portable; solar energy; environment protection Billboard*

1 Introduction

Bulletin boards are an indispensable tool for some organizations such as enterprises and schools or school associations to carry out some publicity. With the increasing number of various organizations in recent years, the demand for bulletin boards will gradually increase [1]. Domestic research on bulletin boards is less, and the first patent was applied for as early as 1987. Since then, various patents on publicity boards have appeared one after another, but most of them are based on appearance design, and there are few utility model and invention patents. Although the research on such devices in my country started late, many patents in this area have also emerged in recent years, but less is actually used [2].

Our country has a huge population base, and the number of various enterprises, schools and other organizations is also increasing. If you want to improve your own popularity, various methods of publicity are essential [3]. This will also lead to a gradual increase in the demand for billboards [4]. However, the existing bulletin boards have many shortcomings, such as: the bulletin boards are bulky, inconvenient to carry and install, and the publicity effect achieved by the bulletin boards is also average, which does not play a big role [5]. In addition, some modern common The bulletin board covers a large area and can only be fixed on the ground. If it is moved, it will take a lot of manpower and material resources, and it will also need to consume extra energy to illuminate the billboard at night, which cannot meet people's needs well [6-7]. Therefore, it is a more urgent task to develop a kind of billboard with reasonable price, environmental protection, portability and ease of use. It is also some expectations of companies or school associations that currently need a lot of publicity. Aiming at these shortcomings, a new mechanical structure bulletin board is designed in this paper.

2 Product design

The base of the bulletin board can play a very good role in fixing. The base is adsorbed on the ground by strong adsorption force to achieve the fixing effect on the billboard. The telescopic rod can adjust the height of the billboard. At the same time, the telescopic rod also increases the portability of the bulletin board. It can shrink the telescopic rod to the minimum and reduce its footprint. The splint and triangular groove are set to facilitate the fixing of promotional materials, and the splint and triangular groove are also convenient. The replacement and retrieval of publicity materials, the sun visor can protect the publicity column and publicity materials in rainy days, prevent rain from damaging the publicity materials, and the sun visor can also provide pedestrians passing by in the sun. A sunshade place, when pedestrians come here to shade, they will notice the content of the promotion, increase the exposure rate of the

Received on March 14, 2022; Accepted on April 20, 2022

promotional materials, and make the promotion efficiency of the bulletin board higher. The board can be retracted so that it can be retracted when not in use, which is convenient to carry and reduces the space occupied. The player is set up to play promotional materials or some music. Playing promotional materials can make passers-by hear the content to be promoted. Music can add attractiveness to the bulletin boards, and at the same time can cultivate sentiment, adding some romantic atmosphere to the whole section of the road. The LED lights can be set to illuminate the billboards at night, so that the billboards can also be played at night. To the effect, the set anti-slip strip can increase the friction between the back cover and the storage cabinet, preventing the back cover from opening and closing at will.

3 Working Principle

The bulletin board is composed of four parts: telescopic support foot structure, folding board structure, storage structure, and circuit assembly.

3.1 Telescopic support foot structure

The structure of the telescopic support foot is shown in Figure 1. The rotating axis allows the support foot to rotate up and down in the vertical plane, and when not in use, it can be turned to the horizontal and stuck to the bottom of the bulletin board to reduce the space occupation rate.

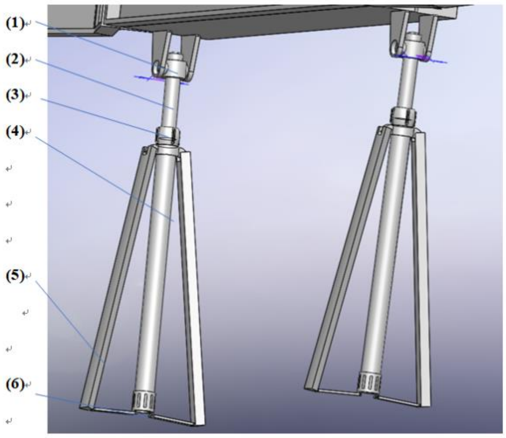

Figure 1 Structure diagram of telescopic support foot (1): rotation axis; (2): telescopic rod 1; (3): knob; (4): telescopic rod 2; (5): support rod; (6): connection sleeve

When using the rotary axis can be rotated to the vertical state, the connection between the knob and the telescopic rod as shown in Figure 2, through the thread at the bottom of the knob and the telescopic rod 2 connected to the upper part of the telescopic rod 1, when the telescopic rod is extended to a certain extent, you can tighten the knob through the friction between the telescopic rod 1 and fixed. At this point by sliding up and down (6) connecting sleeve can be spread the support rod, so that the propaganda bar stable placement.

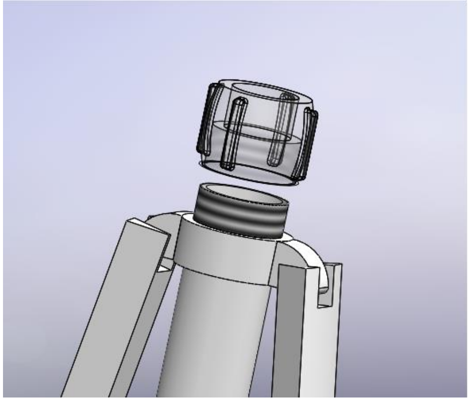

Figure 2 Knob and telescopic rod connection diagram

3.2 Folding plate mechanism

The unfolded and folded states of the folding board are shown in Figures 3 and 4. Folding board 1 and folding board 2 can be connected by ordinary connectors. When not in use, the back of folding board 1 is overlapped with the side of the entire billboard through the connecting rod. At this time, the connecting rod is just placed in slot 1, and the folding board 2 coincides with the back of the bulletin board. Folding board 1 is connected with bulletin board by connecting rod, and connecting rod structure as shown in Figure 5 is used when only needing to rotate connecting rod to straight line and just reaches the dead point in the four-bar structure at this moment.

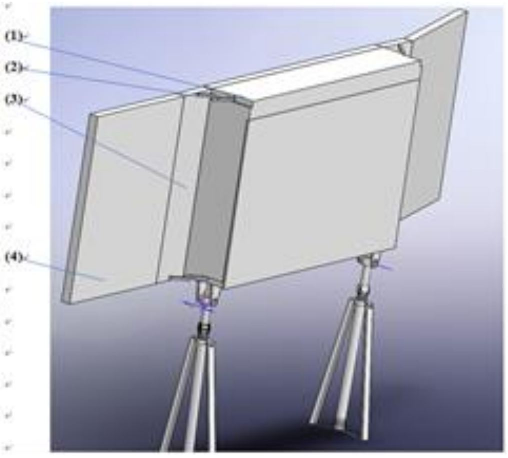

Figure 3 Folding plate unfolding diagram (1): slot; (2): connecting rod; (3): folding plate 1; (4) folding plate 2

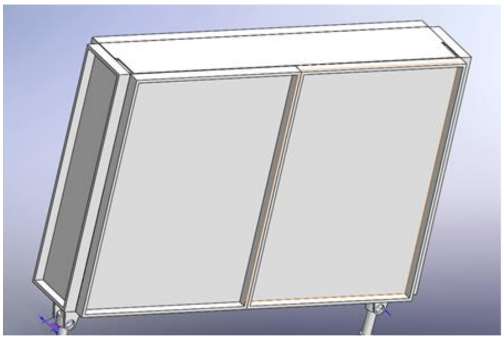

Figure 4 Folded plate folding

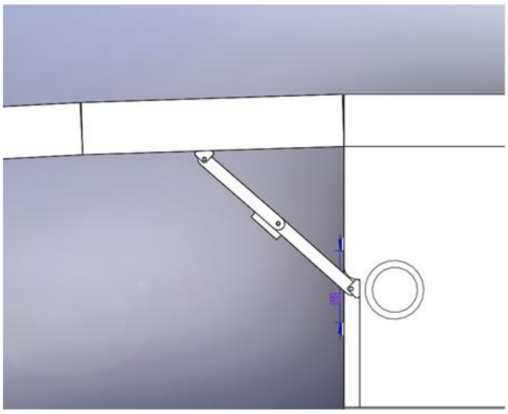

Figure 5 Connection bar structure

3.3 Storage structure

As shown in Figure 6, the back cover and the publicity column can be connected by ordinary connectors. When the publicity column needs to be fully unfolded, the back cover of the publicity column can be uncovered, and the required promotional materials can be placed inside.

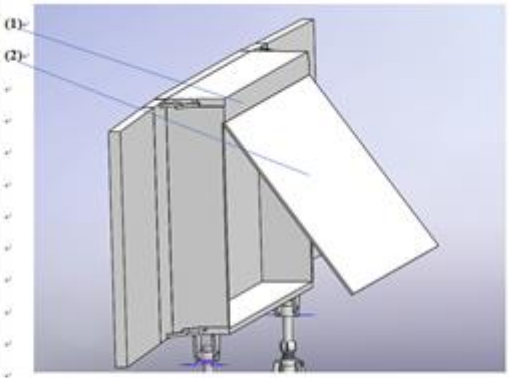

Figure 6 Storage structure (1): circuit placement; (2): back cover

3.4 Circuit Components

The circuit device is placed on the upper part of the bulletin board as shown in Figure 6 (1), and the solar panel is placed on the top of the billboard to absorb solar energy and store it in the battery during the day. It can also achieve the effect of publicity.

3.5 Usage

When using, first through the rotary axis of the two sides of the column support feet rotate to the vertical state, and then loosen the knob, will adjust the telescopic rod up and down to the desired height and then tighten the knob to the telescopic rod height fixed, then the two sides of the connecting sleeve down slide to support the rod to expand, I both sides of the support rod through a connecting rod and connecting sleeve connected, the connecting sleeve slide to the bottom so that the connecting rod just parallel to the ground and Make the support feet on both sides of the support rod and the middle of the support rod three points of a line and just touch the ground. Next, we will be behind the folding board 2 rotation to the folding board 1 parallel, and then the folding board 1 will be unfolded, so that the two connecting rods just straight at this time just to reach the dead spot position in the four rod structure. All done, you can open the back cover will be placed in advance of our publicity material out and placed on the surface of the bulletin board. At this time only need to be placed in the sunlight can be through the top of the solar panel to absorb solar energy and storage, in the night can be stored during the day by led energy release, in order to achieve the purpose of lighting, so as to ensure that the night column can also play a role in the case of energy saving to achieve the purpose of environmental protection.

4 Analysis of innovation points and prospects

4.1 Innovation

(1) The structure of solar panel is adopted, so that our billboard can achieve the effect of publicity even at night, and the energy source is environmentally friendly without spending extra electricity. (2). Our billboard uses a folding board structure to improve the space utilization rate and make the surface area utilization rate reach more than 90%.

(3) The structure of the support foot with telescopic rod allows us to adjust the placement height of the propaganda, and the support foot is fully expanded into a triangle, which improves the stability of the propaganda board and prevents it from being placed on various terrains.

(4) The whole billboard is a cuboid when folded, and we use aluminum alloy to reduce the weight of the billboard.

(5) The hollow part in the middle of our bulletin board can be placed with some materials for our publicity in advance, which also facilitates our publicity and improves the space utilization.

4.2 Prospect analysis

Now more and more enterprises as well as schools and some school clubs need to promote their products or some activities and so on, so the market of the bulletin board will gradually increase, and the current market of the bulletin board, due to a large area, not easy to carry and move and night need to consume electricity for lighting and other issues, resulting in school clubs and enterprises can not carry out effective publicity, and because of At present, the number of bulletin boards is relatively small, leading to many enterprises and school associations can not use the bulletin board for publicity. And our bulletin board just to overcome these shortcomings, it can be carried anywhere we want to propaganda, and occupies a small area, and when not in use can be completely folded up, the space occupied than the general luggage is small, when using the entire surface area can be fully expanded and the bottom can extend the support legs to support the whole board, and the bottom of the support legs for the telescopic structure, can be adjusted according to the terrain or human will. Can be adjusted according to the terrain or human will to adjust the height. And in the era of environmental protection and conservation, our board uses solar energy as the energy source to illuminate the board at night, which not only achieves environmental protection but also saves excess electricity.

Fund project: College Students Innovation and Entrepreneurship Project (S202214435012).

Author introduction: Zhao Fangyue, male, undergraduate, research direction: mechanical design.

References

[1] Zhang Shuai Shuai, Zhao Shengnan, Zhang Yuchuang, et al. Talking about the status quo and management of the bulletin board from the perspective of energy conservation and emission reduction [J]. Enterprise Guide, 2014(8):3.

[2] Ding Yibo, Cai Chuanyang, Qu Jingyi. Design of a new electronic information bulletin board based on solar power generation [J]. Science and Technology Innovation and Productivity, 2021(6): 4.

[3] Chen Jing Research on the Application of Task driven Teaching Method in the Teaching Practice of Higher Vocational Colleges of Architecture -- Taking the computer course "Changzhou Metro Bulletin Board Production" as an example [J]. Science and Technology Horizon, 2017 (30): 2.

[4] Zhang Yuchuang, Zhao Shengnan, Qi Jie, et al. Design research and application analysis of the new bulletin board [J]. Enterprise Guide, 2014 (8): 2.

[5] Qi Jie, Zhao Shengnan, Zhang Yuchuang, et al. Energy conservation and environmental protection issues in the bulletin board [J]. Enterprise Guide, 2014 (8): 2.

[6] Gong Rui, Zhang Yi. Taking Northeastern University as an example to explore the innovative design and promotion of the campus bulletin board [J]. Packaging World, 2015 (4): 2.

[7] Wang Jiaqi, Guo Yuan, Ding Yibo. A new type of solar electronic information bulletin [P]. 2020.

Viser Technology Pte. Ltd.
Research and Application of Materials Science
DOI: 10.33142/rams.v4i1.8460

Research Article **Open Access**

Efficient bio-assembled nanogenerator fabricated from chicken bone epidermis

Yanran MA, Yongfa WANG, Li LI, Chunchang WANG*

Laboratory of Dielectric Functional Materials, School of Materials Science & Engineering, Anhui University, Hefei 230601, China.

***Corresponding Author:** Chunchang WANG, E-mail addresses: ccwang@ahu.edu.cn*

Abstract:
Using biological self-powered materials as a new energy source to replace traditional batteries to power micro-electronic devices is a current research hotspot. We herein fabricate a piezoelectric bio-nanogenerator from chicken bones. The nanogenerator can output a voltage of 1.25 V and a current of 9 nA after being subjected to a pressure of 30 N. This research facilitates an in-depth understanding of bio-nanogenerators and provides a new strategy for reusing bio-waste.

Keywords: *nanogenerator; collagen; piezoelectric; chicken bone epidermis*

1 Introduction

As the energy crisis becomes increasingly severe, the exploration of green and renewable energy sources subsequently received wide attention in various fields. In addition to the traditional energy sources such as coal, natural gas, oil, nuclear energy, as well as green energy sources such as wind, hydro, and solar power that are currently being widely used in the world. On a smaller scale, many scientists are focusing on energy harvesting utilized in our daily life. Researchers have now made some progress in collecting and converting piezoelectric and frictional electricity [1]. The self-powered nanogenerators based on piezoelectric materials have been developed and widely used in fields such as piezoelectric ceramics [1-4] and synthetic polymers [5-7]. However, inorganic power generation materials have some defects in the preparation process, such as high energy consumption, complicated production process, and serious environmental contamination. Therefore, many researchers have turned their attention to biological piezoelectric materials. Piezoelectricity is found in many organs made of biological materials that make up the animal body, such as bone, skin, cellulose, virus, protein, nucleotide and so on [8].

Biological materials are often easily obtained in large quantities and are renewable and less polluting to the environment. Biological piezoelectric materials have not only the high flexibility and toughness of organic materials but also biological compatibility, which is another research hotspot now.

As one of the most abundant renewable resources, biomaterials have an extremely wide range of application scenarios. Compared with conventional polymers, natural biomaterials have unparalleled advantages, namely abundant resources, low prices, simple preparation processes, high energy conversion efficiency, environmental friendliness, and excellent degradability. Problem arises with bio-waste, which can be easily obtained in food production and processing, industrial materials, medical materials, etc. Thus, a large amount of bio-waste is produced every day in these production processes, and how to deal with this bio-waste in the maximum utilization is one of the challenges in this field. Based on the main constituents of bio-waste such as proteins [9], cellulose [10], gelatin [11], chitosan [12], and so on, previous reports have discovered that they can be reused in bio-piezoelectricity. Therefore, we can use bio-waste, for instance, fish scale[13], fish swim bladder[14], and prawn shell [12], to fabricate nanogenerators by simple design and treatment and reduce pollution from traditional energy and electronic waste products. Besides, the nanogenerators based on micro and nanostructures of biomaterials have extremely high sensitivity and electrical output characteristics and can be designed as implantable medical devices or power sources for a wide range of uses considering the degradable properties and excellent biocompatibility of biomaterials [15].

As one of the world's major sources of edible meat, chickens produce a large amount of bone waste every year, and its epidermis is mainly composed of type Ⅰ

Received on April 3, 2022; Accepted on April 23, 2022

collagen which has piezoelectric properties. To our knowledge, piezoelectric nanogenerators fabricated by bone materials are not reported yet. Therefore, chicken bone was chosen as the raw material to prepare bio-nanogenerators. In this study, we fabricated a piezoelectric nanogenerator using chicken bone epidermis (CBENG). The output performance of the CBENG was compared with reported bio-nanogenerators, and the results were listed in Table 1. The raw materials of those reported bio-nanogenerators maintained their natural structures after chemical treatment. The categories, structures, and effective piezoelectric component have an effect on the piezoelectricity of these bio-piezoelectric materials. The CBENG generated an output voltage of 1.25 V and an output current of 9 nA at a pressure of 30N with an impact frequency of 1 Hz. It took 900 seconds to charge the 4.7 μF capacitor to 1.37 V. The CBENG can generate an output power density of 0.01 μW/cm^2 and supply power to small devices like timer through rectifier bridge. The output voltage and current were increased with the rising pressure and impact frequency which proves great sensitivity of CBENG to external pressure changes.

Table 1 Comparison of output performances between the CBENG and other reported piezoelectric nanogenerators based on biomaterials

Material	Effective area	Pressure	Voltage	Current
Native cellulose microfiber[10]	Not supplied	40 kPa	30 V	500 nA
Prawn shell[12]	1.5 ×1 cm^2	12 kPa	4.4V	3.7 nA
Fish scale[13]	1.5 ×1 cm^2	0.17 MPa	4 V	1.5 μA
Fish swim bladder[14]	7 ×3 cm^2	1.4 MPa	10 V	51 nA
Ginkgo tree leaves[16]	Not supplied	16 N	131 V/cm^3	2.5 μA/cm^3
Chicken feather fiber[17]	Not supplied	0.31 MPa	10 V	1.8 mA /cm^2
This work	2.5 ×1.5 cm^2	30N	1.25 V	9 nA

2 Experiment

2.1 Chicken bone treatment

The chicken bone was collected from the fresh food market. The bone treatment and the process of nanogenerator fabrication are shown in Figure 1(a). The chicken bone was cleaned thoroughly with deionized water and dried at 50℃ for 10 hours. For the purpose of demineralization, the bone was soaked in 5 wt% citric acid solution and 0.5 M EDTA for 12 hours in turn [13,18-19]. Then the softened layer was peeled from the surface of the chicken bone and subsequently dried at 50℃ for 10 hours. CBE was sheared into a rectangle for electrode fabrication, which can be seen in Figure 1(b).

2.2 Nanogenerator fabrication

To make a stable nanogenerator, gold (Au) electrodes (with an effective area of ～375 mm^2) were sputtered on both sides of the CBE film. Cu foil was stuck to Au electrodes. Thin copper wires were attached to the Cu foil. Finally, the nanogenerator was sealed to avoid the effect of moisture in the air by a polydimethylsiloxane (PDMS) (DOWSIL, 184 Silicone Elastomer) layer. The PDMS layer is made by mixing the solidified agent in a 1:10 ratio, degassing and curing at room temperature for 15 hours. Figure 1 (c) shows the picture of the CBE made nanogenerator.

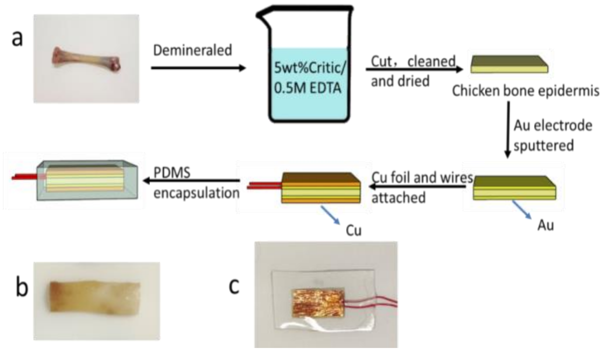

Figure 1 (a) The process of the demineralization and nanogenerator fabrication of chicken bone; (b) A rectangular demineralized chicken bone epidermis; (c) A nanogenerator based on the chicken bone epidermis

2.3 Material characterizations

The structure of the CBE was investigated by X-ray diffraction (XRD, Rigaku Smartlab Beijing Co, Beijing, China) with Cu K α radiation. The detailed cross-section morphologies of the CBE were analyzed by a field emission scanning electron microscope (FESEM, Regulus 8230, Hitachi Co, Japan). The functional groups were analyzed by Fourier microscopy (Vertex80+ Hyperon2000, Bruker, Germany). The dielectric properties of the CBE were gauged by a Wayne Kerr 6500B impedance analyzer (Wayne Kerr Electronic Instrument Co., Shenzhen, China) with Partulab DMS-2000 dielectric measurement system (Partulab Technology Co, Wuhan, China). The sample for dielectric properties characterization was sprayed circular Au electrodes with 6 mm diameter to both sides. The ferroelectric properties of the CBE were tested by a ferroelectric hysteresis measurement tester (MultiFerroic II, Radiant Technologies Inc., Albuquerque, New Mexico) at room temperature and a frequency of 10 Hz. The open circuit voltage and short-circuit current of the CBENG were tested by an electrometer (Model 6514 Programmable Electrometer, Keithley, America). In order to avoid the interference to the test result caused by friction between the PDMS and exterior, the CBENG was wrapped with insulating tape and copper foil with wire grounding.

3 Results and discussion

3.1 Characterization

It has been confirmed in many previous researches that the main components of bone are hydroxyapatite and collagen [18, 20]. Inorganic component with hydroxyapatite as the main component was separated by immersed in citric acid and EDTA solutions [18-19, 21]. To confirm the collagen type of the CBE and analyze its structure, it was investigated by XRD and Fourier Transform infrared spectroscopy (FTIR). As illustrated in Figure 2(a), two main crystallization peaks were located at $2\theta = 7.43^\circ$ and 21.51 °in the XRD pattern of the demineralized CBE. The feature peak at 7.43 ° represents a highly crystalized structure in collagen. The broad peak at 21.51 ° is due to the amorphous composition of collagen [14]. Meanwhile, there were shoulder peaks at $2\theta = 30.81^\circ$ and 38.95° which are caused by amino acid residue of triple-helical structure[14]. These characteristic peaks prove the crystallization behavior of the CBE. The crystallinity is about 27.25% calculated by the Fourier deconvolution calculation. The stable crystalline structure is derived from peptide chains in collagen that relies on many intramolecular and intermolecular hydrogen bonds to form ordered and dense structures.

The cross-section SEM images of the CBE with different multiples are shown in Figure 2 (b, c). Notably, the CBE exhibits a relatively loose layered fiber structure as shown in Figure 2(b). In Figure 2(c), a further enlarged view reveals that the structural composition of the CBE is composed of superimposed collagen fibrils.

The chemical composition of the CBE was tested by FTIR spectrum. The FTIR spectra of the CBE with the attribution of characteristic peaks are shown in Figure 2(d). The figure shows amide I, II, and III bands at 1633, 1548, and 1260 cm^{-1}, respectively. The assignments of amide I band are stretching vibration (ν) of carbon-oxygen double bond (ν(C=O)) or hydrogen bonding. Amide II band is caused by stretching vibrations of carbon-nitrogen bond (ν(C-N)) coupled with bending vibrations (δ) of nitrogen-hydrogen bond (δ(N-H)) [22].The absorption band at 1452 cm^{-1} and amide III band at 1260 cm^{-1} are attributed to δ(CH_2) and δ(N-H), respectively [16]. The existence of triple-helical structure in the CBE collagen is supported by the ratio of absorption band at 1260 cm^{-1} (amide III) and 1452 cm^{-1} (δ (CH_2)), which is 1.034, approximately equal to 1[23-24].Amide A band is usually at 3400-3440 cm^{-1}, and it is generally associated with N-H stretching vibrations (ν (N-H)) and hydrogen bonding on the polypeptide within the CBE collagen. The position of the characteristic peak towards low wavenumber 3287 cm^{-1} is due to the involvement of stretching vibrations of double-bonded carbonic acid (ν(C=N)) and N-H on the peptide in the formation of hydrogen bonds[24]. The observation of two vibration bands at 2980 and 2860 cm^{-1} are related to the asymmetric and symmetric vibrational modes of CH_2 (ν(CH_2)), respectively. The two combined bands prove that amide B band is existed in collagen fibers. The above analysis demonstrates the existence of the triple-helical structure in collagen of the CBE and the structural stability of collagen fibrils in the CBE because of its regular bonding and crystallinity. Collagen fibers are combined by hydrogen bonding to form type I collagen fiber bundles, which finally constitute a laminar structure. This structural feature facilitates the formation of

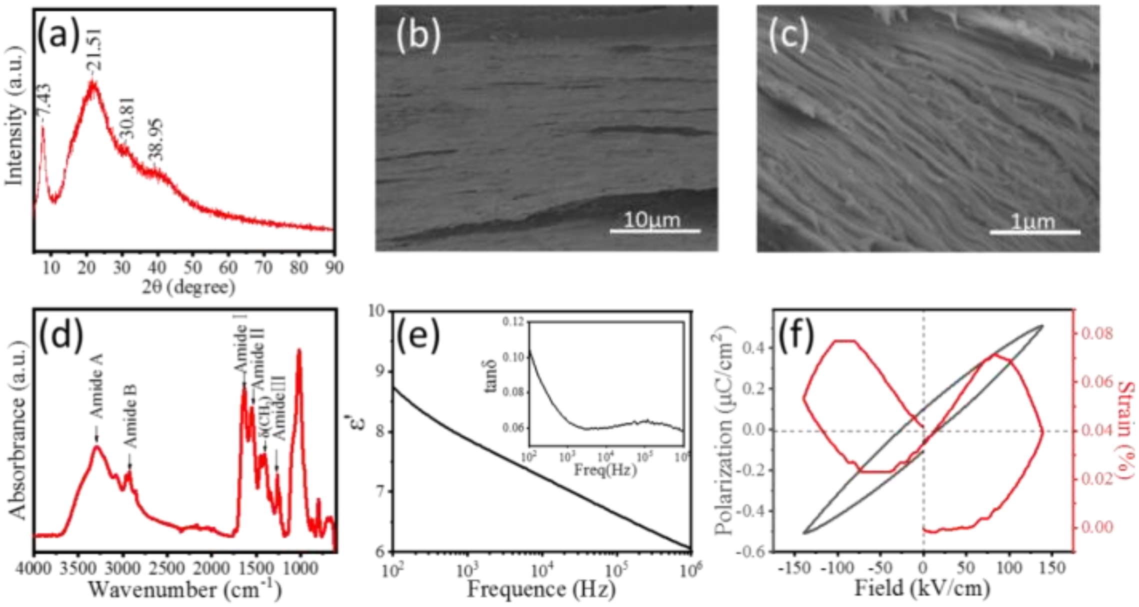

Figure 2 (a) XRD spectra of the CBE. (b, c) SEM of cross-section images. (d) FTIR patterns of the CBE. (e) Frequency dependent tan δ and ε' in the frequency range from 10^2 to 10^6 Hz. (f) The standard P-E loop and S-E loop of the CBE

spontaneous polarization, which results in the piezoelectric effect [25-26]. Quarterly interlacing of collagen molecules gives the typical axial and cyclical organization of collagen protofibrils, and protofibrils are further assembled to form collagen fibers. The formation of hydrogen bonds between multi-peptide chains is crucial for piezoelectricity. Collagen is a natural electret or bio-electret material because of the inherent uniaxial polar orientation of molecular dipoles leading to polarization and piezoelectricity [27]. In summary, the results prove the existence of the helical structure and the tripeptide sequence of Gly-Pro-Y in the collagen of the CBE as shown in Figure 3 [27].

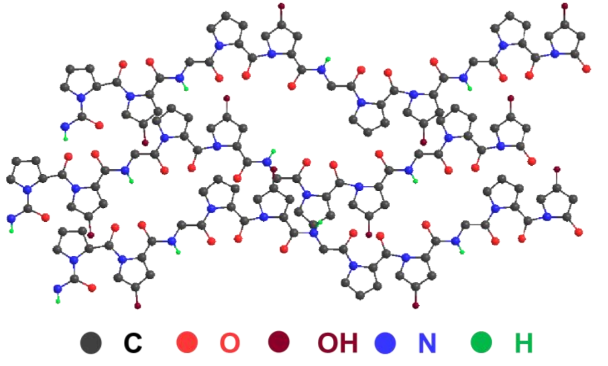

Figure 3 The schematic illustration of peptide chains of collagen in CBE

In order to illustrate this point, we measured the dielectric dissipation factor (tan δ) and dielectric constant (ε') of the CBE in the frequency range from 10^2 to 10^6 Hz, and the results are shown in Figure 2(e). The dielectric constant is 8.5 at 100 Hz and monotonically decreases with increasing frequency. The tan δ curve registers a pear at 2×10^5 Hz and increases rapidly with decreasing frequency. The tan δ pear suggests that there exists a relaxation in the CBE. The low-frequency increase in tan δ indicates a Maxwell-Wagner relaxation caused by the space charge. The results evidence that the CBE is able to store and release electric charge. To further confirm the ferroelectricity and piezoelectricity of the CBE, hysteresis of polarization (P) with electric field (E) was measured as shown in Figure 2(f). It demonstrates a remnant polarization (Pr) of 0.1 μC/cm^2. The corresponding strain (S) - electric field (E) hysteresis loop shows a butterfly shape as shown in Figure 2(f). The above proved the existence of inverse piezoelectric effect in the CBE.

3.2 Working principle

It has been confirmed that the reason of piezoelectricity in bone is the existence of tropocollagen, which is the basic structural composition unit of collagen [28]. This is due to the particular arrangement of the polypeptide chain in tropocollagen [29]. The tropocollagen consists of three polypeptide chains in a triple-helical structure. When subjected to external mechanical pressure, the triple-helical structure will uncoil. As a result, the hydroxyproline side chains will become more inclined to the long axis of the tropocollagen which reorients the polar groups of the molecule. At the same time, the dipole moment changed under external pressure. The above leads to the polarization of the CBE and piezoelectric effect. The piezoelectric mechanism is shown in Figure 4. The generation of electricity in the CBENG results from piezoelectric mechanism, of which the CBE generates an electric field and induces opposite charges in the upper and lower electrodes because of the mechanical deformation and polarization of the CBE. Due to the fact that CBE is a dielectric material, electrons can only pass through the external load. When it is pressed by external pressure, it will generate a positive output current. When deformation reaches the maximum, the output current decreases to 0 nA. As the nanogenerator is releasing, the free charge reverses to form the opposite current to balance the cumulative charge at both ends of the external circuit.

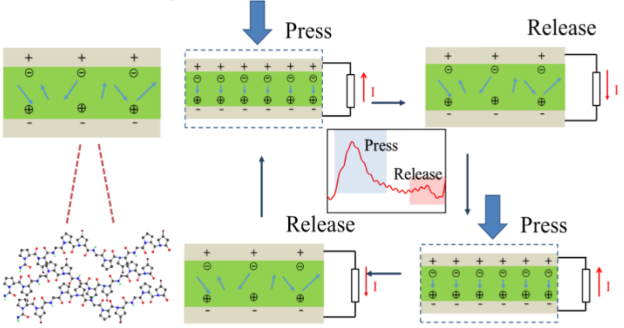

Figure 4 Schematic diagram of the CBE piezoelectricity

3.3 CBENG output

To test the output performance of the nanogenerator, we used an electrometer to measure its output voltage and output current under the steady pressure of the electric motor. The results are demonstrated in Figure 5.

The output performance of the nanogenerator was tested by periodical electric motor impact vertically on the electrodes under a mechanical pressure of 30 N. As shown in Figure 5(a, b), the output voltage of the CBENG is 1.25 V and the output current is 9 nA. In the reverse connection, the output amplitude of the CBENG is same but the curve is in opposite direction compared with the forward connection. It is due to piezoelectric effect. In order to measure the output current and calculate the power density of the CBENG under different resistive loads, a variable value resistor box was connected to the nanogenerator to form a closed circuit. In Figure 5(c), the current decreases with the increase of the resistance. When resistance reached 5×10^7 Ω, the output power shows a maximum value of 0.01 μW/cm^2 as deduced according to the following formula:

$$P = U^2 /RA \tag{1}$$

where A is the effective area of the CBENG (25mm×15mm), U is the output voltage in the closed circuit, R is the external load resistance. In the output test, CBENG exhibited better output performance when subjected to vertical mechanical stress on the electrode

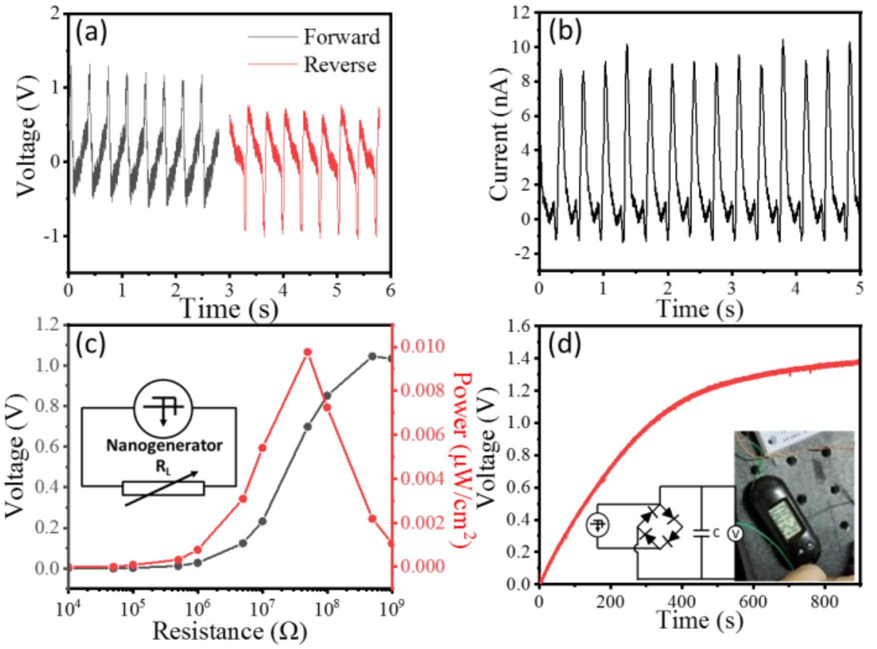

Figure 5 Output performance of the CBENG. (a) Output voltage and (b) output current under a constant pressure of 30 N. (c) Output voltage and output power density on the different external load resistance (R_L). (d) A capacitor charging and driving an electronic timer performance

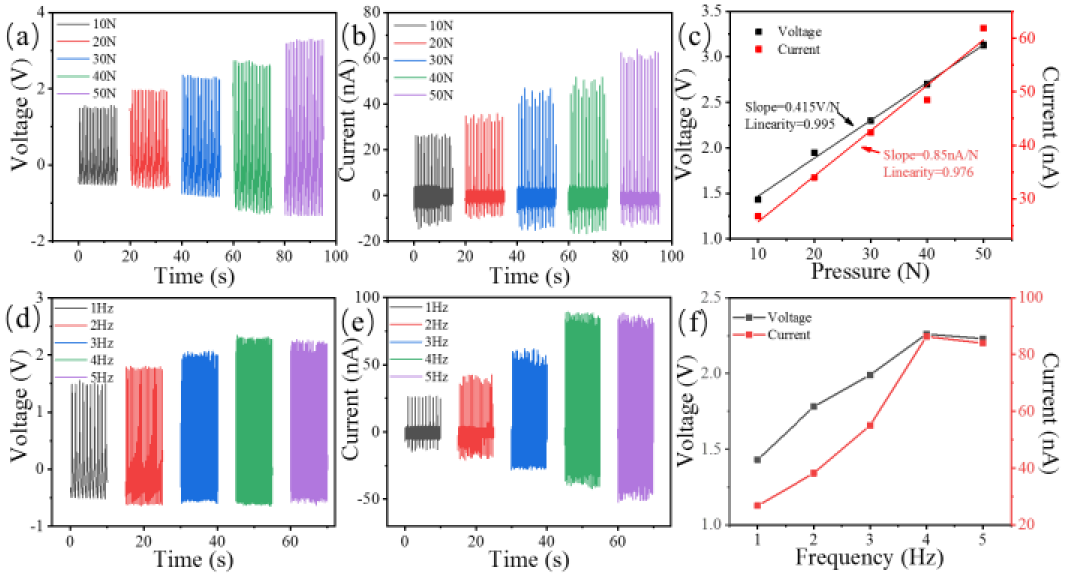

Figure 6 (a) Output voltage and (b) output current of CBENG under diverse external pressure. (c) Dependence of output voltage and current of the CBENG on the external pressure. (d) Output voltage and (e) output current of CBENG under different impact frequency. (f) Dependence of output voltage and current of the CBENG on the impact frequency

surface. It is expected that the molecular structure is changed under an applied stress, which, in turn, gives rise to the piezoelectricity of collagen.

To test the charging performance of the CBENG, a rectifier bridge and a 4.7 μF capacitor in closed circuit were connected to the generator. The schematic circuit diagram used to charge the 4.7 μF capacitor is shown in Figure 5(d). It took 900 seconds to charge the 4.7 μF capacitor to 1.37 V. It can supply power to small devices like timer through rectifier bridge as shown in Figure 5(d).

In order to systematically study the output properties of the CBENG ($A=3\times2$ cm^2), it was tested under diverse external pressure and different impact frequency. As Figs. 6(a-c) show, with the increase of external pressure, the output voltage and current were linear increased. Through linear fit calculation, the slope of output voltage is 0.415

V/N and the linearity is 0.995. The slope of output current is 0.85 nA/N and the linearity is 0.976. It performed the great pressure sensing property of CBENG in a broad range of pressure. The CBE is polarized under the external force and leads to the appearance of bound charges with opposite polarities on the surfaces of both ends of the CBE. The charge density is proportional to the external mechanical force. Therefore, the output voltage and current are positively correlated with the external force which proved piezoelectric effect in CBE. As Figs. 6(d-f) show, with the increase of impact frequency, the output voltage and current increased gradually to a steady level. Due to the high impact frequency, the CBE can't recover its shape in time to cause the voltage to stop increasing. CBENG exhibits good pressure sensing sensitivity and can be used as an excellent pressure sensor. It also can be used to collect and transform mechanical energy to charge small devices.

4 Conclusion

In conclusion, we proved that CBE can be used as biological piezoelectric material and fabricated a flexible and biocompatible nanogenerator based on it. The main component, microstructure, dielectric properties of chicken bone epidermis, and the output performance of the nanogenerator were investigated. The nanogenerator can output a voltage of 1.25 V and a current of 9 nA after being subjected to a pressure of 30 N. It can be used to charge low-power devices by a rectifier bridge and measure pressure as pressure sensor because of its sensitivity of external force. Authors believe it will provide further insights into the processing of bio-wastes.

Declaration

The authors report no declarations of interest.

Acknowledgements

This work was financially supported by the National Natural Science Foundation of China (Grant Nos. 51872001 and 12174001).

References

[1] Su Y Li, W Yuan, L Chen, C Pan, H, Xie, G Conta, G, Ferrier, S Zhao, X Chen, G Tai, H Jiang, Y Chen. J Piezoelectric fiber composites with polydopamine interfacial layer for self-powered wearable biomonitoring. Nano Energy 2021(89): 106321.

[2] Su, H Wang, X Li, C Wang, Z Wu, Y Zhang, J Zhang, Y Zhao, C Wu, J Zheng. H Enhanced energy harvesting ability of polydimethylsiloxane-BaTiO3-based flexible piezoelectric nanogenerator for tactile imitation application. Nano Energy 2021(83): 105809.

[3] Wang, Z Yuan, X Yang, J Huan, Y Gao, X Li, Z Wang, H Dong. S 3D-printed flexible, Ag-coated PNN-PZT ceramic-polymer grid-composite for electromechanical energy conversion. Nano Energy 2020(73): 104737.

[4] Ji, S. H Lee, W Yun, J. S All-in-One Piezo-Triboelectric Energy Harvester Module Based on Piezoceramic Nanofibers for Wearable Devices. ACS applied materials & interfaces 2020, 12 (16): 18609-18616.

[5] Rahman, M. A Rubaiya, F Islam, N Lozano, K Ashraf, A Graphene-Coated PVDF/PAni Fiber Mats and Their Applications in Sensing and Nanogeneration. ACS applied materials & interfaces 2022, 14 (33): 38162-38171.

[6] Su, Y Chen, C Pan, H Yang, Y Chen, G Zhao, X Li, W Gong, Q Xie, G Zhou, Y Zhang, S Tai, H Jiang, Y Chen, J Muscle Fibers Inspired High-Performance Piezoelectric Textiles for Wearable Physiological Monitoring. Advanced Functional Materials 2021, 31 (19): 2010962.

[7] Zhao, J Li, F Wang, Z Dong, P Xia, G Wang, K Flexible PVDF nanogenerator-driven motion sensors for human body motion energy tracking and monitoring. Journal of Materials Science: Materials in Electronics 2021, 32 (11): 14715-14727.

[8] Cao, L Qiu, X Jiao, Q Zhao, P Li, J Wei, Y. Polysaccharides and proteins-based nanogenerator for energy harvesting and sensing: A review. International journal of biological macromolecules 2021, 173, 225-243.

[9] Chang, T.-H Peng, Y.-W Chen, C.-H Chang, T.-W Wu, J.-M Hwang, J.-C Gan, J.-Y Lin, Z.-H. Protein-based contact electrification and its uses for mechanical energy harvesting and humidity detecting. Nano Energy 2016(21): 238-246.

[10] Alam, M. M Mandal, D. Native Cellulose Microfiber-Based Hybrid Piezoelectric Generator for Mechanical Energy Harvesting Utility. ACS applied materials & interfaces 2016, 8 (3): 8-1555.

[11] Ghosh, S. K Adhikary, P Jana, S Biswas, A. Sencadas, V. Gupta, S. D Tudu, B Mandal, D. Electrospun gelatin nanofiber based self-powered bio-e-skin for health care monitoring. Nano Energy 2017(36): 166-175.

[12] Ghosh, S. K.; Mandal, D. Bio-assembled, piezoelectric prawn shell made self-powered wearable sensor for non-invasive physiological signal monitoring. Applied Physics Letters 2017, 110 (12): 123701.

[13] Ghosh, S. K Mandal, D. High-performance bio-piezoelectric nanogenerator made with fish scale. Applied Physics Letters 2016, 109 (10): 103701.

[14] Ghosh, S. K Mandal, D. Efficient natural piezoelectric nanogenerator: Electricity generation from fish swim bladder. Nano Energy 2016(28): 356-365.

[15] Chen, S Wu, N Lin, S Duan, J Xu, Z Pan, Y Zhang, H Xu, Z Huang, L Hu, B Zhou, J. Hierarchical elastomer tuned self-powered pressure sensor for wearable multifunctional cardiovascular electronics. Nano Energy 2020(70): 104460.

[16] Shao, D Wang, C Li, W Lu, L Lu, J Yang, W. Natural ginkgo tree leaves as piezo-energy harvesters. Journal of Materials Chemistry C 2022, 10 (40): 15016-15027.

[17] Kar, E Barman, M Das, S Das, A Datta, P Mukherjee, S Tavakoli, M Mukherjee, N Bose, N. Chicken feather fiber-based bio-piezoelectric energy harvester: an efficient green energy source for flexible electronics. Sustainable Energy & Fuels 2021, 5 (6): 1857-1866.

[18] Cao, S Wang, Y Xing, L Zhang, W Zhou, G. Structure and

physical properties of gelatin from bovine bone collagen influenced by acid pretreatment and pepsin. Food and Bioproducts Processing 2020(121): 213-223.

[19] Wilson, T Szpak, P. Acidification does not alter the stable isotope composition of bone collagen. PeerJ 2022(10):e13593.

[20] Liu, H.; Huang, K., Structural Characteristics of Extracted Collagen from Tilapia (Oreochromis mossambicus) Bone: Effects of Ethylenediaminetetraacetic Acid Solution and Hydrochloric Acid Treatment. International Journal of Food Properties 2014, 19 (1): 63-75.

[21] Jaziri, A. A Shapawi, R Mohd Mokhtar, R. A Md Noordin, W. N Huda, N. Biochemical analysis of collagens from the bone of lizardfish (Saurida tumbil Bloch, 1795) extracted with different acids. PeerJ 2022(10): e13103.

[22] Muyonga, J. H Cole, C. G. B Duodu, K. G. Characterisation of acid soluble collagen from skins of young and adult Nile perch (Lates niloticus). Food Chemistry 2004, 85 (1): 81-89.

[23] Kaewdang, O Benjakul, S Kaewmanee, T Kishimura, H. Characteristics of collagens from the swim bladders of yellowfin tuna (Thunnus albacares). Food Chem 2014(155): 264-70.

[24] Wang, L. S Shi, Z Shi, B. M Shan, A. S. Effects of dietary stevioside/rebaudioside A on the growth performance and diarrhea incidence of weaned piglets. Animal Feed Science and Technology 2014(187): 104-109.

[25] Guerin, S.; Syed, T. A. M.; Thompson, D., Deconstructing collagen piezoelectricity using alanine-hydroxyproline-glycine building blocks. Nanoscale 2018, 10 (20): 9653-9663.

[26] Ravi, H. K Simona, F Hulliger, J Cascella, M. Molecular Origin of Piezo- and Pyroelectric Properties in Collagen Investigated by Molecular Dynamics Simulations. The Journal of Physical Chemistry B 2012, 116 (6): 1901-1907.

[27] Wu, B Mu, C Zhang, G Lin, W. Effects of Cr3+ on the structure of collagen fiber. Langmuir 2009, 25 (19): 11905-10.

[28] Weiner, S. W. H. D. The Material Bone: Structure-Mechanical Function Relations. Annual Review of Materials Science 1998, 28 (1): 271-298.

[29] Zhou, Z Qian, D Minary-Jolandan, M. Molecular Mechanism of Polarization and Piezoelectric Effect in Super-Twisted Collagen. ACS Biomater Sci Eng 2016, 2(6): 929-936.

Viser Technology Pte. Ltd.
Research and Application of Materials Science
DOI: 10.33142/rams.v4i1.8461

Research Article Open Access

Recent Progress of Catalytic Cathodes for Lithium-oxygen Batteries

Wei WANG [1], Simin WANG [1], Longhai ZHANG [1*], Sijiang HU [2], Xuyang XIONG [1, 3], Tengfei ZHOU [1], Chaofeng ZHANG [1*]

1.Institutes of Physical Science and Information Technology, Leibniz Joint Research Center of Materials Sciences, Anhui Graphene Engineering Laboratory, Anhui University, Hefei 230601, China
2.Guangxi Key Laboratory of Low Carbon Energy Material, Guangxi Normal University, Guilin 541004, China
3.Key Laboratory of Advanced Energy Materials Chemistry (Ministry of Education), College of Chemistry, Nankai University, Tianjin 300071, China

***Corresponding Author**: Longhai ZHANG, Chaofeng ZHANG*

Abstract:
Lithium-oxygen batteries are among the most promising electrochemical energy storage systems, which have attracted significant attention in the past few years duo to its far more energy density than lithium-ion batteries. Lithium oxygen battery energy storage is a reactive storage mechanism, and the discharge and charge processes are usually called oxygen reduction reaction (ORR) and oxygen evolution reaction (OER). Consequently, complex systems usually create complex problems, lithium oxygen batteries also face many problems, such as excessive accumulation of discharge products (Li_2O_2) in the cathode pores, resulting in reduced capacity, unstable cycling performance and so on. Cathode catalyst, which could influence the kinetics of OER and ORR in lithium oxygen (Li-O_2) battery, is one of the decisive factors to determine the electrochemical performance of the battery, so the design of cathode catalyst is vitally important. This review discusses the catalytic cathode materials, which are divided into four parts, carbon based materials, metals and metal oxides, composite materials and other materials.

Keywords: *lithium oxygen battery; cathode; catalyst; energy storage*

1 Introduction

With the continuous progress of science and technology, the demand for energy becomes higher and higher, which presents a huge challenge to energy storage technology. Electrochemical energy storage modes include fuel cells, supercapacitors, rechargeable batteries, etc [1-3]. At present, rechargeable lithium-ion batteries are widely used in human daily life (such as notebook computers and smart phones) [4-8]. However, lithium-ion battery (LIB) also face some serious problems, the most fatal problem of lithium-ion batteries is the low energy density, only 250 Wh kg-1, which hinders its application in some fields [5-9]. Other ion batteries (such as zinc ion batteries and sodium ion batteries) still need a lot of research to improve their performance [10-15]. This has led to an increasing requirement for electrochemical energy storage devices with high energy density. Lithium-oxygen batteries (LOB) as a promising energy storage form is widely studied, due to the ultra-high theoretical specific energy density (about 3500 Wh kg-1), which is much higher than lithium-ion battery [16-20].

Electrochemical storage of nonaqueous lithium oxygen batteries is reactive storage mechanism [21]. As shown in equation 1, during the discharge process of lithium oxygen battery, oxygen is reduced in the cathode and reacts with Li+ to form Li_2O_2, which stays in the pores of the cathode. This process is also called oxygen reduction reaction (ORR). In the charging reaction, Li_2O_2 decomposes to form Li+ and O_2 (equation 2). This process is also called oxygen evolution reaction (OER) [22]. However, in the ORR process, Li_2O_2 will be continuously generated and attached to the surface of the catalyst. Excessive deposition of Li_2O_2 will block the pores of the catalyst, resulting in the reduction of discharge capacity. In turn, in the OER process, the incomplete decomposition of Li_2O_2 will reduce the charging capacity [23-24]. Due to the insulation of Li_2O_2, it leads to sluggish kinetics in ORR and OER process [25-26]. In this case, LOB face issues such as large overpotential between charge and discharge process, low round-trip

Received on February 20, 2022; Accepted on April 10, 2022

efficiency, and poor cycle life, which hinder their commercial application [4, 27-31]. Using appropriate catalyst can enhance the cycle stability and diminish the overpotential [23, 29, 32]. Therefore, it is necessary to study suitable and porous cathode catalysts.

$$\mathrm{ORR:}\quad 2\mathrm{Li}^{+} + \mathrm{O}_2 + 2\mathrm{e}^{-} \rightarrow \mathrm{Li}_2\mathrm{O}_2 \tag{1}$$

$$\mathrm{OER:}\quad \mathrm{Li}_2\mathrm{O}_2 \rightarrow 2\mathrm{Li}^{+} + \mathrm{O}_2 + 2\mathrm{e}^{-} \tag{2}$$

In the past several decades, an army of scientists have been committed to solving the challenges which confronted with lithium oxygen batteries. Research shows that Li_2O_2 is only ideal discharge product, but it is not the only discharge product. LOB may also generate products such as LiOH during discharge, which cannot be completely changed back to Li ions and O_2 in charging [5]. This will lead to poor performance of lithium oxygen batteries. Recent studies have pointed out that cathode catalyst as an indispensable part of lithium oxygen battery. The structure, the surface pores and the type of catalyst will affect the formation of Li_2O_2, so the selection and design of catalyst is of great significance [33-36].

Figure 1 Classification of cathode materials for lithium oxygen batteries

This paper reviews the effects of cathode catalyst types on the performance of LOBs in recent years. In this review, catalysts are divided into four types as shown in figure 1. (1) Carbon materials [37-38]. Carbon materials are used in LOB cathode because of high conductivity and rich pores, which can accommodate more discharge product Li_2O_2 [39]. Moreover, carbon materials can also promote the ORR process. However, during the OER process, the catalytic activity of carbon materials is slightly low.[40] (2) Metals and metal oxides [41].They can enhance the decomposition of Li_2O_2, thereby accelerating the OER process [42-44]. (3) Composite materials [45-46]. Few single materials can promote both ORR and OER process in LOB at the same time. Scientists try to composite two or more materials to make up for their shortcomings, so as to obtain better electrochemical performance. For example, the combination of carbon materials and metals, on the one hand, the addition of metals can effectively improve the shortcomings of carbon materials in the OER process, on the other hand, it can also have the advantages of porous carbon materials. (4) Other materials [47-48]. In addition to the three types of materials mentioned above, sulfides and nitrides etc. Can also be used as cathode of lithium oxygen batteries and show good performance. In order to clearly understand the performance of various catalyst materials, we compared them in the form of radar chart (figure 2), where their pore size, catalytic activity, preparation complexity, cycle stability, overpotential and price are considered. In the following chapters, we will briefly introduce these types of catalyst materials.

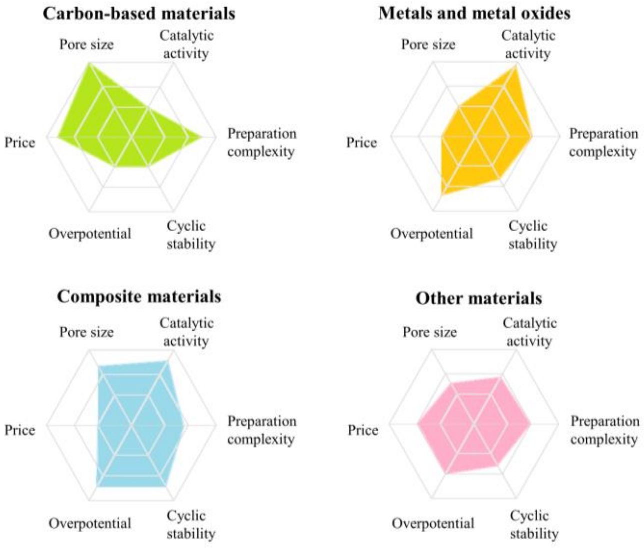

Figure 2 Overview of performance of different types of catalysts in lithium oxygen batteries

2 Carbon based materials

Carbon materials have been broadly used as conductive agents, cathode material and catalyst carrier in lithium oxygen batteries due to their high specific surface area, excellent electrical conductivity and low cost. Carbon material can show very good catalytic performance in ORR and OER processes and can be used as porous cathode catalyst in non-aqueous lithium oxygen batteries [3].

2.1 Carbon materials

General speaking, the properties of lithium oxygen cells may be influenced by the morphology, specific surface area and pore structure of carbon materials. To explore the link between carbon performance and battery capacity. Ding et al [49]. have compared the influence of eight different carbon materials on the capacity of lithium oxygen batteries: multi-walled carbon nanotubes (MWCNT), and ordered mesoporous carbon (OMC), and activated carbon and commercial carbon black (Ketjen black, Super P and acetylene black), and inverse opal carbon (IOC) and reduced graphene oxide (rGO).

Figure 3a shows the initial charge-discharge curves of different carbon materials as the cathode electrode of lithium oxygen batteries. MWCNT clearly delivers the lowest discharge capacity of only 1311 mA h g-1, while rGO delivers the highest discharge capacity of above 8400 mA h g-1. The OMC and activated carbon have a slightly higher discharge capacity than the MWCNT, with only 1812 mA h g-1 and 1897 mA h g-1 respectively. The capacities of three kinds of carbon black (Ketjen black, Super P and acetylene black) cathode are 2865, 3399 and 3512 mA h g-1. Both IOC and OMC are mesoporous carbon materials, but the discharge capacity of IOC is 4504 mA h g-1, which is more than twice that of OMC. The difference of the capacities between OMC and IOC can be attributed to different properties of carbon materials. As seen from the Table 1, the discharge capacity of battery exhibits proportionality to the pore sizes. When the pore size of the carbon material is larger, the capacity to store the product Li_2O_2 becomes better, so the discharge capacity is increased. However, MWCNT is an exception. The reason for this is the large length-to-diameter ratio of the MWCNT. The ultralong transport channel is not conducive to the diffusion of O_2. The open ends of MWCNT are small, which are easily to be blocked by the discharge products, resulting in little actual utilization rate of pore and low discharge capacity.

Table 1 Surface area and pore characteristics of various carbons and their influence on the capacity of Li－O_2 batteries

Carbon materials	Surface area (m2 g-1)	Pore volume (cm3 g-1)	Pore size (nm)	Discharge capacity (mA h g-1)
MWCNT	929	1.64	7.0	1311
OMC	863	1.14	5.2	1812
Activated carbon	1230	1.07	4.7	1897
Ketjen black	818	1.17	7.7	2865
Super P	62	0.32	11.9	3399
Acetylene black	56	0.16	11.4	3512
IOC	794	3.17	16.0	4504
rGO	361	1.58	17.5	8418

The disadvantage of single carbon material is that there are fewer active sites and the catalytic activity cannot meet the needs of batteries. At high voltage single carbon material will promote the conversion of discharge product Li_2O_2 to other lithium compounds, which will lead to the degradation of the cycle performance of the battery.

2.2 Doped carbon materials

Many studies have shown that the introduction of heteroatoms will change the morphology and electronegativity of carbon-based materials, resulting in the formation of pores and functional groups. Therefore, carbon materials with low doping level of non-metallic elements (such as N-element doping) can significantly enhance the electrochemical properties of carbon materials. N-doped carbon materials can obviously improve the electrochemical performance. As the concentration of N element doping in the carbon material increases, the band gap decreases, which benefit to improve the conductivity of the carbon material.

Shui *et al* [50]. used CVD (chemical vapor deposition) method to get vertically aligned nitrogen-doped coral-like carbon fiber (VA-NCCF). As shown in the figure 3b, the overpotential decreases obviously due to the doping of the N element. At 500 mA g-1 current density, the lithium oxygen battery which used VA-NCCF as cathode catalyst demonstrated a high discharge capacity more than 40000 mA h g-1 (figure 3c). At limit high specific capacities (1000 mA h g-1), the cell could cycle stably for 150 times. Because of low overpotential and minimal electrolyte decomposition. The doping of N elemental improved the catalytic activity, reduced the overpotential between charge and discharge, and reduced the decomposition of electrolyte. The unique structure provided space for the deposition of product Li_2O_2 and transport of reactants.

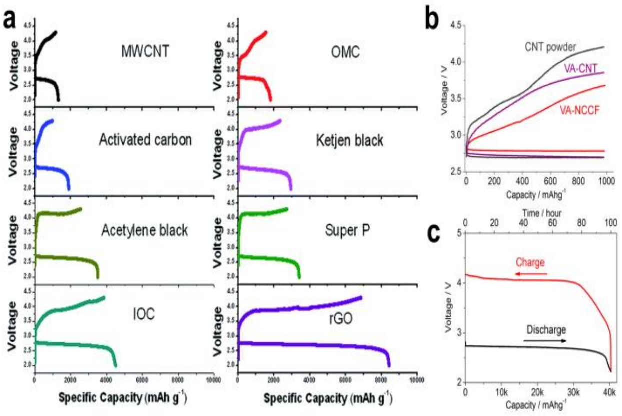

Figure 3 (a) Initial charge/discharge voltage profiles of various carbon materials cycled under 50 mA g-1. (b) Comparisons of VA-NCCF, VA-CNT and CNT powder. (c) Charge/discharge voltage profile of VA-NCCF at a current density of 500 mA g-1

Zhang *et al* [51]. controlled flow of H_2O (gas) to oxidize the reduced graphene into holey graphene (hG) with plenty of nanoholes. The as-prepared hG was heating under NH3/Ar and heating with H_3BO_3 under Ar atmosphere to prepared B,N-hG. B,N-hG shows the lowest overpotential at a current density of 100 mA g-1 and the highest discharge capacity (15340 mA h g-1) than bare hG, B-hG and N-hG. At limit high specific capacities (1000 mA h g-1) and a current density of 500 mA g-1, the battery with B,N-hG as cathode could cycle stably for 117 times which is better than the other three materials. These excellent properties are attributed to the nanopore enlargement in graphene induced by the doping of elements B and N and the synergy between the two elements. The enlargement of nanopore allows the cathode to accommodate more Li_2O_2, and the doping of B and N atoms increases the conductivity of the material itself. Combining these advantages, B,N-hG can obtain higher discharge capacity. Although doping non-metallic elements can improve the properties of carbon materials, large-scale production and control of uniform doping of elements still a challenge. This makes it more difficult to commercialize the method of doping non-metallic elements to improve the electrochemical performance of lithium oxygen batteries.

3 Metals and metal oxides

In oxygen reduction reaction (ORR), metal and metal oxides promote the formation of thin films or nanoparticles with low crystallinity Li_2O_2. Because of the low crystallinity, Li_2O_2 is more easily decomposed during charging (OER), and therefore has a lower decomposition potential during charging. Therefore, metal and metal oxides as catalyst can reduce the overpotential during charge and discharge process and improve the cycle stability of lithium oxygen batteries [52]. In this part, metals and metal oxides are introduced from the following three aspects: (1) noble metal and noble metal oxides, (2) transition metal and transition metal oxides, and (3) perovskite and their oxides.

3.1 Noble metal and noble metal oxides

Noble metal nanoparticles are considered to be excellent catalytic materials that can promote oxygen reduction reactions (ORR) in batteries and many oxidation reactions.

Bui *et al* [53]. prepared carbon nanofibers with platinum nanoparticles (CNF@Pt) by electrospinning. Compared with the traditional encapsulating method, the catalyst prepared by electrospinning can expose more active materials, thus improving the electrochemical performance of lithium oxygen battery. Pt nanoparticles are evenly distributed on CNF. At various current densities of 200 mA g-1, 500 mA g-1, and 1000 mA g-1, the charge-discharge curves of CNF@Pt and CNF are similar, but the capacity of CNF@Pt is much larger than that of CNF, and the overpotential of CNF@Pt is lower than that of CNF in the charge-discharge process. At a current density of 200 mA g-1, the capacity of CNF@Pt was 6938 mA h g-1. At a current density of 500 mA g-1 and limited high specific capacity of 1000 mA h g-1, the battery with CNF@Pt as cathode could cycle stably for 162 times which is better than the battery with CNF as cathode. Due to the catalytic activity of Pt in ORR and OER processes, lithium oxygen batteries with CNF@Pt exhibit higher specific capacity and better cycle stability.

Jeong *et al* [54]. systematically evaluated the catalytic performance of Pt, Pb and Ru nanoparticles by supported them on rGo as cathode catalysts for lithium oxygen batteries. At a current density of 200 mA g-1 and limited high specific capacity of 2000 mA h g-1, the introduction of noble metal can obviously reduce the overpotential between charge and discharge. Among them, Ru presents the best cyclic stability and the lowest overpotential during the charge and discharge process. In the charge discharge curve (figure 4a), it can be found that the introduction of ruthenium can significantly reduce the potential during charging. There are two advantages when Ru is used as a catalyst. First, Ru has obvious effect in reducing the size and induced morphology of the discharge product, and the formed discharge product is easier to be completely decomposed during charging. Second, ruthenium is mixed with Li_2O_2, the discharge product is catalysis decomposed by electron transfer, which reduces the decomposition voltage of the discharge product. Compared with Ru, the incorporation of Pt and Pd will promote the decomposition of electrolyte, resulting in slightly poor performance of lithium oxygen battery.

Compared to single noble metal system, it is difficult for a single metal to perform well in both ORR and OER processes. Therefore, the noble bimetal system can cooperate with the catalytic effect of the two noble metals, and the two metals show excellent catalytic performance in the ORR and OER processes respectively [52].

Lu *et al* [55]. introduced PtAu nanoparticles, which can significantly improve the kinetics of the ORR and OER processes of rechargeable lithium oxygen batteries. As catalysts, PtAu/C and carbon exhibit similar specific capacities (～1200 mA h g-1) in lithium oxygen batteries (figure 4b). It was obvious that PtAu/C overpotential is lower than pure carbon during ORR and OER. As shown in the figure 4c, the discharge curve of PtAu/C is similar to that of Pt in the OER process, and the charge curve of PtAu/C is similar to that of Au in the ORR process. Therefore, it is concluded that Pt nanoparticles have catalytic effect on OER, while Au nanoparticles have catalytic effect on ORR.

Choi *et al* [56]. synthesized PdCu noble bimetal nanoparticles with disordered face-centered cubic and ordered body-centered cubic mixed phase by polyol method for lithium oxygen battery cathode. The lithium oxygen battery with PdCu has a cycle efficiency of nearly 80% at a current density of 200 mA g-1. The discharge voltage without decay after 50 cycles at high current density 5000 mA g-1. The excellent performance of the battery could be attributed to the good catalytic activity of PdCu noble bimetal material during ORR and OER processes, thus greatly reducing the overpotential in the process of charge and discharge. Their theoretical calculations showed that the transfer of electrons from Cu atom to Pd atom weakens the adsorption strength of lithium oxide on the PdCu nanoparticles and ultimately reduces the overpotential.

Noble metal oxides can also be used as catalysts for lithium oxygen batteries. For example, Jung *et al* [57]. synthesized ruthenium (Ru) and hydrated ruthenium oxide ($RuO_2 \cdot 0.64H_2O$) uniformly distributed on rGo. At a current density of 500 mA g-1 and a limited specific capacity of 5000 mA h g-1, the battery cycling stably for 30 cycles (figure 4d). Noble metals and their oxides are used as cathode catalysts for lithium oxygen batteries, the performance of batteries has been greatly improved.

However, the shortcomings of limited reserves in nature and high cost greatly limit the practical application of noble metals and their oxides.

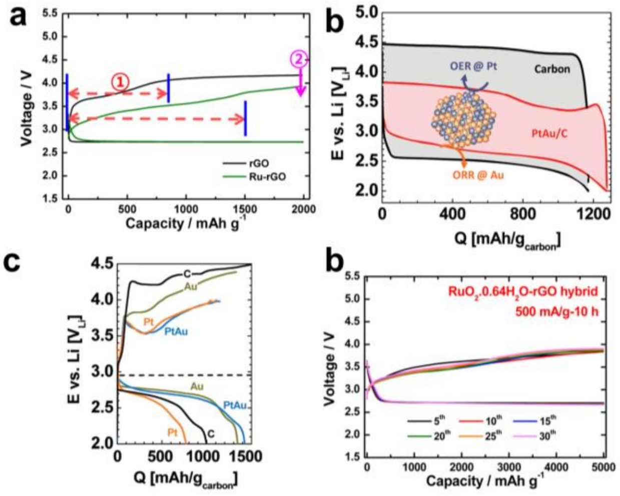

Figure 4 (a) The potential profiles of rGO and Ru-rGO at 200 mA g-1 for 10 h. (b) LOB charge/discharge profiles of carbon and PtAu/C in the third cycle. (c) LOB first charge/discharge profiles of carbon at 85 mA g-1 and of Au/C, Pt/C, and PtAu/C at 100 mA g-1. (d) Charge/discharge profiles of different cycles of $RuO_2 \cdot 0.64H_2O$-rGO hybrid

3.2 Transition metal and transition metal oxides

Transition metals (such as Mn, Fe, Co, Ni, Zn, etc.) and transition metal oxides (such as MnO_2, CoO, FeO, etc.) all show catalytic potential of ORR/OER. Compared with noble metals, they are abundant and cheap. Therefore, many studies have been conducted by using them as catalysts for lithium oxygen batteries.

Wang *et al* [58]. embedded Co single atoms in nitrogen-rich carbon (Co-SAs/N-C) as a catalyst for lithium-oxygen batteries. At a current density of 200 mA g-1, the battery with Co-SAs/N-C as cathode exhibited discharge capacity of 20105 mA h g-1 and charge capacity of 19765 mA h g-1 in the first cycle. The initial coulomb efficiency was close to 100%. At a current density of 400 mA g-1 and a limited specific capacity of 1000 mA h g-1, the battery could cycle stably for 260 times. As shown in the figure 5a, Li atom of the discharge product and N atom form effective coordination sites, and there is also strong binding between O atom and Co atom. In the figure 5b, the N-C material without Co-N4 has only the combination of Li atom and N atom. The overpotentials between charge and discharge is defined as: ∆U=UC-UDC, where UC and UDC represent charge and discharge potential respectively. It is obvious that the calculated overpotential of Co-SAs/N-C is significantly smaller than that of N-C, which indicates that doping Co atoms can reduce the overpotential. As shown in figure 5c that the exposed active sites are conducive to adsorbing more discharge products.

Gao *et al* [59]. reported a CoO/C composite with oxygen vacancy. Compared with commercial CoO, the lithium oxygen battery with CoO/C materials containing oxygen vacancies have higher initial capacity, better rate performance and cycle stability. They attributed the improved performance of CoO/C composites containing oxygen vacancies to the presence of oxygen vacancies. The existence of oxygen vacancies improves the migration capacity of electrons and Li+, and can be used as the active site for the reaction of oxygen and Li_2O_2. In addition, doped C not only has good ORR activity, but also improves the conductivity of CoO and stabilizes oxygen vacancy. Lin *et al* [60]. found that Co_3O_4/CNT had good catalytic activity when it was used as cathode of lithium oxygen battery, which significantly ameliorated the weak catalytic activity of CNT in OER process and reduced the overpotential. In situ EPR test showed that Co_3O_4 catalyst inhibited the formation of by-products.

As the catalyst of lithium oxygen battery, manganese-based material can not only improve the specific capacity, but also improve the coulombic efficiency of the battery.

Zhang *et al* [61]. prepared a tubular δ-MnO_2 material with microstructure by hydrothermal synthesis (as shown in figure 5d). SEM images (figure 5e and f) show that δ-MnO_2 tube is a nanorod with porous flower-like surface. This structure is conducive to the penetration of electrolyte, so as to speed up the transportation of Li+. The lithium oxygen battery with MnO_2/KB as catalyst exhibited a capacity of 6150 mA h g-1 at the current density of 25 mA g-1. Even at a high current density of 600 mA g-1, the battery exhibited a capacity of 2850 mA h g-1. Obviously, the rate properties and cycling properties of MnO_2/KB material are better than pure KB. They found that the discharge product Li_2O_2 of the lithium oxygen battery with MnO_2 forms a uniform nanosheet, which is more easily decomposed during charging. Therefore, the specific capacity and cycle performance of battery were improved, especially the OER reactivity were significantly improved. The improvement to unique microscopic tubular structure of δ-MnO_2 material, which promoted the generation of nanosheet Li_2O_2, thus improved the properties of lithium oxygen battery. In addition to pure manganese oxide, introducing other transition metals to replace a small amount of Mn element in manganese oxide to form doped catalysts is also a method to improve the properties of batteries.

Minowa *et al* [62]. found that the battery with Mn_2O_3 as cathode catalyst had better properties than both MnO and MnO_2. In order to improve the battery performance with Mn_2O_3, they used other transition metals to replace a small amount of Mn in Mn_2O_3 to form Mn_2-xMxO_3 (M = Fe, Mn, Ni and Co) catalyst. The experimental results show that when 0.2Mn is replaced by Fe, the battery exhibits the best property. For example, the capacity of the battery increased, and the overpotential decreased. So far, researchers have studied a variety of manganese oxides, such as α-MnO_2, β-MnO_2, MnOOH and so on.

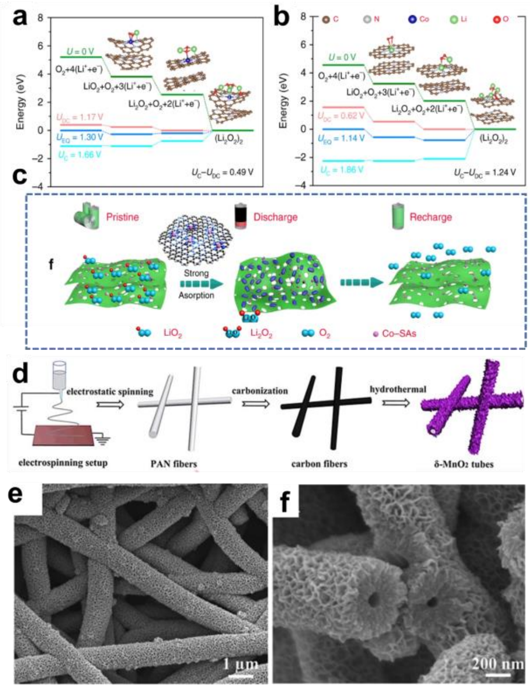

Figure 5 Calculated free energy diagrams for the charge/discharge reactions on the active surface of (a) Co-SAs/N-C and (b) N-C. (c) Schematic illustrations of the working mechanism for the Co-SAs/N-C electrodes. (d) Scheme of the preparation of δ-MnO_2 tubes. (e, f) SEM images of δ-MnO_2 tubes

3.3. Perovskite and their oxides

The molecular formula for perovskite oxide is ABO_3. Perovskite oxides are used in lithium oxygen batteries because of their excellent catalytic activity and electrical conductivity. Hedge *et al* [25]. prepared the oxygen vacant $CaMnO_3$ (H-CMO) with multiple oxygen vacancies by sol-gel method and low-temperature hydrogen reduction method. It is obvious from the figure 6a that H-CMO not only reduces the charging over potential, but also reduces the discharge over potential, which generally reduces the over potential between charging and discharging. In terms of circulation, the performance of H-CMO is also significantly better than that of CMO. At a current density of 500 mA g-1 and a limited specific capacity of 500 mA h g-1, the battery could cycle stably for 110 times. Li *et al* [63]. prepared one-dimensional porous La0.5Sr0.5CoO$_2$.91 nanotubes by electrostatic spinning technology. Electrochemical test showed that the initial discharge capacity is 7205 mA h g-1 at a current density of 100 mA g-1, which is close to the performance of noble metal CNT@Pt. At a current density of 200 mA g-1 and a limited specific capacity of 1000 mA h g-1, the battery could cycle stably for 85 times. The excellent performance of the battery is attributed to the structure of the nanotubes to transport electrons and the addition of active sites.

Compared with common perovskite oxides, double perovskite oxides have higher oxygen and electron transfer capacity. Ma *et al* [64]. synthesized SrCrMoO6-δ (SCM) which is a double perovskite structure oxide. SCM was used as catalyst for lithium oxygen battery. At a current density of 75 mA g-1, the discharge capacity of battery was 2306 mA h g-1, which is much higher than the Super P electrode capacity (1434 mA h g-1). In addition, the overpotential of SCM is lower than that of Super P (figure 6b). At a current density of 200 mA g-1 and a limited specific capacity of 600 mA h g-1, the terminal discharge voltage drops to 2.34 V after 30 cycles. Under the same conditions, the terminal discharge voltage of Super P drops below 1.5 V after 13 cycles. The experimental results showed that the oxides with double perovskite structure can promote the properties of lithium oxygen battery. Zhu *et al* [65]. reported a new cathode catalyst called PrBaCo_2O_5+δ (PBCO). The electrochemical performance of PBCO is much better than that of commercial BP2000. As shown in the figure 8c and d, it can be seen from the charge discharge curve under various current densities that the capacity of PBCO is much higher than that of BP2000. PBCO exceeds 8000 mA h g-1 when the current density is 0.02 mA cm-2. Moreover, the overpotential is also significantly lower than BP2000. When the current density is limited to 1000 mA h g-1, it can be stably maintained for more than 1000 cycles.

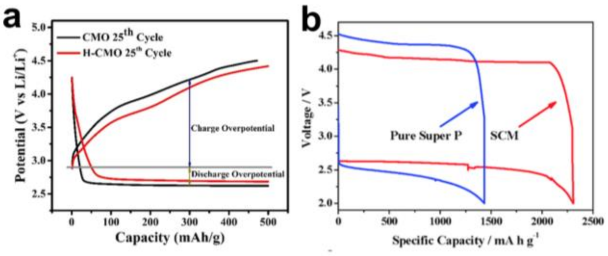

Figure 6 (a) Comparison of overpotentials for CMO and H-CMO. (b) Potential profiles of LOB with SCM based or pure Super P electrodes at 75 mA g-1

Although perovskite oxide can improve the performance of lithium oxygen battery, the battery performance degrades quickly and the cycle performance is at a low level (～ 100 times). Therefore, the research on these materials needs to be more in-depth and comprehensive.

4 Composite materials

The improvement of cathode catalyst can improve the properties of lithium oxygen batteries. Studies in recent years showed that catalysts with good properties usually need to meet the following two requirements, one of which is that catalysts have large specific surface area and more and large pores to store more discharge products (Li_2O_2) to achieve better properties. The other one is that the catalyst promotes both the ORR and OER processes to improve the energy efficiency of the battery. At present, there are few pure materials that can meet these two requirements, so scientists have come up with composite materials.

Functional carbon materials have more and large pores to store discharge product (Li_2O_2), and provide carriers for metal and metal oxides. Carbon materials have excellent catalytic activity for ORR process, but poor catalytic effect for OER process. The development of carbon-based nanocomposites solves this problem. Therefore, the composite materials of functional carbon materials with metal and metal oxides are ideal materials for cathode catalysts of lithium oxygen batteries.

Sun *et al* [66]. synthesized a mesoporous carbon nano-cubes (MCCs) by hard template method. At a current density of 200 mA g-1, the lithium oxygen battery with MCCs as the cathode catalyst showed the discharge capacity was 26100 mA h g-1 and the charge capacity was 16,090 mA h g-1, far higher than that of carbon black (CB) electrode (discharge capacity was 620 mA h g-1 and charge capacity was 3933 mA h g-1). Ru@MCCs was synthesized by wet impregnation method. And the TEM images of MCCs and Ru@MCCs (figure 7a and b) showed that the pore structures of them were similar, indicating that the introduction of Ru did not affect the pores of MCCs. It can be seen from the figure 7c that the charging voltage platform of Ru@MCCs is much lower than MCCs, so the overpotential of Ru@MCCs is much lower than MCCs, only 0.28 V. At a current density of 400 mA g-1 and a limited specific capacity of 1000 mA h g-1, the battery could cycle stably for 120 times. Such excellent performance can be attributed to the unique architecture of MCCs combined with the highly efficient Ru nanocrystal catalysts.

Guo *et al* [67]. prepared N-doped graphene with encapsulated RuO_2 nanoparticles. They compared the electrochemical properties of N-doped graphene, N-doped graphene with unencapsulated RuO_2 nanoparticles and N-doped graphene encapsulated RuO_2 nanoparticles. As exhibited in the figure 7d, it is obvious that the introduction of RuO_2 can reduce the overpotential between charge and discharge progresses. At a current density of 400 mA g-1 and a limited specific capacity of 2000 mA h g-1, the battery could cycle stably for 110 times. The author attributed the excellent performance of the battery to the high catalytic activity of RuO_2 nanoparticles, which reduced the overpotential of Li_2O_2 decomposition. In addition, RuO_2 nanoparticles were encapsulated in graphene, so the batteries showed excellent cycling performance.

In addition to carbon matrix composites, the composite of metals or metal oxides can also make up for defects, so as to obtain better electrochemical performance. Lian *et al* [68]. improved the electrochemical performance of lithium oxygen batteries by loading transition metal atoms on Co_3O_4 nanosheets (MSA-Co_3O_4/CC, M = Ti, V, Cr, Mn, Fe, Ni, Cu, Zn). Through comparison charge/discharge curves, it is found that the introduction of Ni reduces the over potential of the battery most significantly. When the current density is 300 mA g-1 and the limited capacity is 1500 mA h g-1, the overpotential of NiSA-Co_3O_4/CC is only 1.06 V. When the current density is 200 mA g-1 and the limited capacity is 1000 mA h g-1, the over potential is only 0.72 V, and it can circulate stably for 128 cycles. Li *et al* [69]. prepared three-dimensional open Co_3O_4@MnO_2 catalyst. Co_3O_4 has excellent OER catalysis, while MnO_2 is an efficient ORR catalyst. The combination of the two reflects the synergistic effect. Moreover, the three-dimensional open structure also facilitates the generation and decomposition of Li_2O_2. As a catalyst, the LOB shows ultra-high capacity (12980 mA h g-1) and good recyclability (331 cycles can be stably circulated when the capacity is limited to 500 mA h g-1).

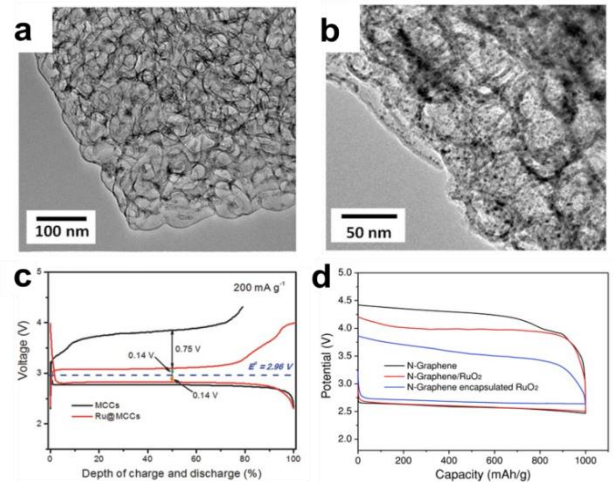

Figure 7 (a, b) High-magnification TEM images of MCCs and Ru@MCCs, and (c) charge/discharge profiles tested of Ru@MCC and MCC at 200 mA g-1. (d) The comparisons of charge/discharge profiles of LOB based on three different cathodes at the same current density and limited capacity

In addition, composite materials of organic compounds and carbon materials have been applied to lithium oxygen batteries, and their electrochemical performance has also been improved. Lin *et al.* [70] studied composite materials, which were composed by nitrogen-containing organic compounds with Ketjin black. The charge and discharge capacity increased significantly. The nitrogen element in the organic compound improves the solvent pathway of Li_2O_2 growth, so that the discharge product exists in an incompact nanosheet shape, which is benefit for decomposition during charging. The organic composite material can also alleviate the sensitivity to the electrolyte. Cui *et al.*[71] reported the influence of different polyaniline contents in three-dimensional porous polyaniline (PANI)/reduced graphene oxide foam (PPGFs) on lithium oxygen batteries. PPGFs-50 shows excellent electrochemical performance, with a high discharge capacity of 36010 mA h g-1 at 200 mA g-1, which can be comparable to noble metal catalysts. Too much polyaniline leads to pore clogging and reduces pore size, while a small amount of polyaniline leads to the reduction of catalytic activity. PPGFs-50 not only has sufficient catalytic activity to promote the generation and decomposition of discharge products, but also can provide sufficient transport channels for lithium ions and oxygen.

Composite materials are the main research direction of lithium oxygen battery. The prepared composites not only need to have sufficient catalytic activity to promote the generation and decomposition of discharge products, but also need to have transport channels for the rapid transport of lithium ions and oxygen. Metal carbon matrix composites have both the characteristics of porous carbon materials and the advantages of high catalytic activity of metals. At present, there are many researches. Nonmetallic composites, such as organic carbon matrix composites, have excellent properties, and the designability of organic structures makes them have great potential.

5 Other materials

In addition to the three kinds of materials mentioned above, there are other types of materials used in lithium oxygen batteries. Such as sulfides, nitrides and so on. Li *et al.* [72] reported the performance of TiN nanoparticles supported on VC as cathode catalysts for lithium oxygen batteries. By comparing the performance of nano TiN/VC (n-TiN/VC), micrometer TiN/VC (m-TiN/VC) and bare VC, it is found that n-TiN /VC overpotential was lower than the other two materials. At a current density of 500 mA g-1, the discharge capacity of N-Tin /VC reaches 6407 mA h g-1, which is much higher than n-TiN /VC and VC. The improvement of battery performance was mainly due to the excellent catalytic activity of TiN nanoparticles and the internal contact between TiN and VC.

Cao *et al.* [73] introduced nitrogen-doped MoS2 (N-MoS2) which was nanoflower-like and porous by hydrothermal method and ammonia-atmosphere calcination process. As cathode catalyst for lithium oxygen battery, N-MOS2 has good performance, such as excellent cycle stability and rate performance. For example, N-MOS2 has a higher specific capacity than MoS2, and the gap between charge and discharge potentials of N-MOS2 is smaller than MoS2 under a same current density. This was due to the rich porous structure of N-MOS2, which provides more catalytic active centers for catalytic reaction. And N doping increased the electrochemical activity. And at a current density of 200 mA g-1 and a limited specific capacity of 1000 mA h g-1, the battery could cycle stably for 100 times. The rate test shows With the increase of current density, the polarization of N-MOS_2 changes little. When the current density returns to 100, the charge discharge voltage of MoS2 also returns to the same as the initial one. As the current density of N-MOS_2 increases, the polarization increases. Even if the current density recovers, the charge discharge voltage does not recover. Sun *et al.* [74] embedded VOx in carbon paper, and then nitrogenize it at 850oC to obtain NV@C-850. The performance of the catalyst doped with nitrogen element is obviously improved at 100 mA g-1 current density, it can have an ultra-high capacity of 8269 mA h g-1, which is attributed to the internal channel of the catalyst, which is conducive to the transportation of Li_2O_2. The synergistic effect between NV and N-doped carbon reduces the overpotential between charge and discharge process (only 0.88 V) and improves the cycle stability (183 cycles at a cut-off capacity of 1000 mA h g-1).

6 Summary

Lithium oxygen battery is a promising form of energy storage. But some problems of LOB make it cannot be used commercially. For example, there are some side reactions in the charge and discharge process, which irreversibly produce other lithium compounds, greatly reducing the charge and discharge capacity of LOB. The cycle life of LOB is very short, and at least 1000 stable cycles are possible to be commercialized. The current research has not met such requirements. In this review, the effects of several types of cathode catalysts on the electrochemical performance of LOB were reviewed, including the formation mechanism and morphology of Li_2O_2. The growth morphology of the discharge product Li_2O_2 will directly affect the electrochemical performance of LOB. LOB with film-like Li_2O_2 has a lower charging potential and a smaller discharge capacity. Whereas LOB with toroidal-like Li_2O_2 shows the discharge capacity increases and the charging overpotential increases. In order to obtain the best electrochemical performance (high capacity and low potential), it can be adjusted by reducing the size of Li_2O_2 particles and increasing the thickness of Li_2O_2 film. There are many methods to adjust the morphology of Li_2O_2. Firstly, the reasonable design of catalyst structure. Porous and large specific surface area cathode materials can improve the structure of Li_2O_2. Secondly, it is favorable to form thin-film Li_2O_2 under high current density. Finally, the selection of electrolyte is also a method to adjust the morphology of discharge products.

In conclusion, the LOB with large capacity, low overpotential and long cycle stability needs to consider the following two factors: 1) forming Li_2O_2 film with increased thickness and 2) forming discharge products particles with decreased size. The following suggestions can be considered to meet the above requirements.

(1) Cathode design. Porous, high specific surface area and high conductivity cathode materials are conducive to the formation of Li_2O_2.

(2) Catalyst selection. Catalysts with advantages like oxygen vacancies and surface coatings can contain more discharge products. The catalyst has the ability to catalyze the formation and decomposition of Li_2O_2, which is helpful to improve the capacity and cycle life of the battery.

(3) Selection of electrolyte. Proper electrolyte is helpful to alleviate the solubility problem. Moreover, solid electrolyte can inhibit the growth of lithium negative dendrite and improve the safety performance of the battery. It is a potential research direction. In addition, electrolyte additive is also a new method to adjust battery life.

The research of LOB is very promising, but more experiments are still needed to study and overcome the shortcomings like the poor cycle performance. The future research and application of lob is very promising.

Acknowledgements

We thank the financial support from the National Natural Science Foundation of China (52172173, 51872071), Anhui Provincial Natural Science Foundation for Distinguished Young Scholar (2108085J25), Anhui Provincial Natural Science Foundation for Outstanding Young Scholar (2208085Y05), Anhui Province Key Laboratory of Environment-Friendly Polymer Materials, the Natural Science Research Projects of Universities in Anhui Province (KJ2020A0021), Guangxi Key Laboratory of Low Carbon Energy Materials (2021GXKLLCEM04).

Author contribution

Chaofeng Zhang and Longhai Zhang putted forward the review topics and gave suggestions. Xuyang Xiong conducted the literature review and classification. Sijiang Hu and Tengfei Zhou designed and drew the figures. Wei Wang and Simin Wang communicated, wrote, and corrected the manuscript.

Conflict of interest

The authors declare no conflict of interest.

References

[1] Wu, F Yu, Y., Toward True Lithium-Air Batteries, Joule 2018(2): 815-817.

[2] Li, J Ding, S Zhang, S et al., Catalytic redox mediators for non-aqueous Li-O2 battery, Energy Storage Mater. 2021(43): 97-119.

[3] Ma, Z.; Yuan, X.; Li, L., et al., A review of cathode materials and structures for rechargeable lithium–air batteries, Energy Environ. Sci. 2015(8): 2144-2198.

[4] Shen, S.; Wu, A.; Xia, G., et al., Facile preparation of unique three-dimensional (3D) α-MnO$_2$/MWCNTs macroporous hybrid as the high-performance cathode of rechargeable Li-O2 batteries, Nano Res. 2019(12): 69-75.

[5] Jung, J.-W.; Cho, S.-H.; Nam, J. S., et al., Current and future cathode materials for non-aqueous Li-air (O$_2$) battery technology – A focused review, Energy Storage Mater. 2020(24): 512-528.

[6] Zhang, X.; Mu, X.; Yang, S., et al., Research Progress for the Development of Li-Air Batteries: Addressing Parasitic Reactions Arising from Air Composition, Energy & Environmental Materials. 2018(1): 61-74.

[7] Sun, T.; Li, Z. J.; Zhi, Y. F., et al., Poly(2,5‐Dihydroxy‐1,4‐Benzoquinonyl Sulfide) As an Efficient Cathode for High‐Performance Aqueous Zinc–Organic Batteries, Adv. Funct. Mater. 2021(31): 1.

[8] Wang, X.-T.; Yang, Y.; Guo, J.-Z., et al., An advanced cathode composite for co-utilization of cations and anions in lithium batteries, Journal of Materials Science & Technology 2022(102): 72-79.

[9] Liu, K.; Liu, Y. Y.; Lin, D. C., et al., Materials for lithium-ion battery safety, Sci. Adv. 2018(4): eaas9820.

[10] Gu, Z.-Y.; Guo, J.-Z.; Sun, Z.-H., et al., Air/water/temperature-stable cathode for all-climate sodium-ion batteries, Cell Reports Physical Science. 2021(2): 2-3.

[11] Wu, K.; Ning, F.; Yi, J., et al., Host-guest supramolecular interaction behavior at the interface between anode and electrolyte for long life Zn anode, J. Energy Chem. 2022(69): 237-243.

[12] Cui, J.; Liu, X.; Xie, Y., et al., Improved electrochemical reversibility of Zn plating/stripping: a promising approach to suppress water-induced issues through the formation of H-bonding, Materials Today Energy. 2020(18): 5.

[13] Wu, K.; Yi, J.; Liu, X., et al., Regulating Zn Deposition via an Artificial Solid-Electrolyte Interface with Aligned Dipoles for Long Life Zn Anode, Nanomicro Lett. 2021(13): 79.

[14] Liu, X.; Fang, Y.; Liang, P., et al., Surface-tuned two-dimension MXene scaffold for highly reversible zinc metal anode, Chin. Chem. Lett. 2021(32): 2899-2903.

[15] Li, Q.; Han, L.; Luo, Q., et al., Towards Understanding the Corrosion Behavior of Zinc‐Metal Anode in Aqueous Systems: From Fundamentals to Strategies, Batteries & Supercaps. 2022(5): 3-5.

[16] Chen, K.; Yang, D. Y.; Huang, G., et al., Lithium-Air Batteries: Air-Electrochemistry and Anode Stabilization, Acc Chem Res. 2021(54): 632-641.

[17] Zhan, Y.; Luo, S.-h.; Feng, J., et al., Improved electrocatalytic activity of hexagonal prisms Fe3O4 derived from metal-organic framework by covering dendritic-shaped carbon layer in Li–O$_2$ battery, Composites Part B: Engineering. 2021(226): 128-134.

[18] Chen, K.; Huang, G.; Ma, J. L., et al., The Stabilization Effect of CO2 in Lithium-Oxygen/CO2 Batteries, Angew. Chem. Int. Ed. Engl. 2020(59): 16661-16667.

[19] Liu, Z.; Zhao, Z.; Zhang, W., et al., Toward high‐performance lithium‐oxygen batteries with cobalt‐based transition metal oxide catalysts: Advanced strategies and mechanical insights, InfoMat. 2021(4): 2.

[20] Guo, X.; Xiao, L.; Yan, P., et al., Synergistic tuning of electrochemical surface area and surface Co^{3+} by oxygen plasma enhances the capacities of Co3O4 lithium–oxygen battery cathodes, Chin. Chem. Lett. 2021(32): 3491-3495.

[21] Hou, C.; Han, J.; Liu, P., et al., Synergetic Effect of Liquid and Solid Catalysts on the Energy Efficiency of Li-O$_2$ Batteries: Cell Performances and Operando STEM Observations, Nano Lett. 2020(20): 2183-2190.

[22] Liu, Y.; He, P.; Zhou, H., Rechargeable Solid-State Li-Air and Li-S Batteries: Materials, Construction, and Challenges, Adv.

Energy Mater. 2018(8): 6-8.

[23] Liu, L.; Liu, Y.; Wang, C., et al., Li_2 O_2 Formation Electrochemistry and Its Influence on Oxygen Reduction/Evolution Reaction Kinetics in Aprotic Li-O_2 Batteries, Small Methods. 2022(6): e2101280.

[24] Liu, B.; Sun, Y.; Liu, L., et al., Advances in Manganese-Based Oxides Cathodic Electrocatalysts for Li-Air Batteries, Adv. Funct. Mater. 2018(28): 56-58.

[25] Hegde, G. S.; Ghosh, A.; Badam, R., et al., Role of Defects in Low-Cost Perovskite Catalysts toward ORR and OER in Lithium – Oxygen Batteries, ACS Applied Energy Materials. 2020(3): 1338-1348.

[26] Zhao, Y.; Chen, W.; Wu, J., et al., Recent advances in charge mechanism of noble metal-based cathodes for Li-O_2 batteries, Chin. Chem. Lett. 2022.

[27] Chen, Y.; Gao, X.; Johnson, L. R., et al., Kinetics of lithium peroxide oxidation by redox mediators and consequences for the lithium-oxygen cell, Nat. Commun. 2018(9): 767.

[28] Sun, G.; Zhao, Q.; Wu, T., et al., 3D Foam-Like Composites of Mo2C Nanorods Coated by N-Doped Carbon: A Novel Self-Standing and Binder-Free O_2 Electrode for Li-O_2 Batteries, ACS Appl Mater Interfaces. 2018(10): 6327-6335.

[29] Ju, B.; Song, H. J.; Lee, G.-H., et al., Nickel disulfide nanosheet as promising cathode electrocatalyst for long-life lithium – oxygen batteries, Energy Storage Mater. 2020(24): 594-601.

[30] Lim, H. D.; Lee, B.; Bae, Y., et al., Reaction chemistry in rechargeable Li-O_2 batteries, Chem. Soc. Rev. 2017(46): 2873-2888.

[31] Shu, C.; Wang, J.; Long, J., et al., Understanding the Reaction Chemistry during Charging in Aprotic Lithium-Oxygen Batteries: Existing Problems and Solutions, Adv Mater. 2019(31): e1804587.

[32] Li, F.; Chen, J., Mechanistic Evolution of Aprotic Lithium-Oxygen Batteries, Adv. Energy Mater. 2017(7):4-7.

[33] Song, L. N.; Zhang, W.; Wang, Y., et al., Tuning lithium-peroxide formation and decomposition routes with single-atom catalysts for lithium-oxygen batteries, Nat. Commun. 2020(11): 2191.

[34] Hou, Y.; Wang, J.; Hou, C., et al., Oxygen vacancies promoting the electrocatalytic performance of CeO_2 nanorods as cathode materials for Li – O_2 batteries, J. Mater. Chem. 2019(7): 6552-6561.

[35] Liang, R.; Shu, C.; Hu, A., et al., Interface engineering induced selenide lattice distortion boosting catalytic activity of heterogeneous CoSe2@NiSe2 for lithium-oxygen battery, Chem. Eng. J. 2020(393):1.

[36] Hou, Y.; Wang, J.; Liu, J., et al., Interfacial Super-Assembled Porous CeO_2/C Frameworks Featuring Efficient and Sensitive Decomposing Li2O2 for Smart Li-O-2 Batteries, Adv. Energy Mater. 2019(9):5.

[37] Jung, I.-S.; Kwon, H. J.; Kim, M., et al., Rapid oxygen diffusive lithium – oxygen batteries using a restacking-inhibited, free-standing graphene cathode film, J. Mater. Chem. 2029(7): 10397-10404.

[38] Li, M.; Xiao, L.; Wang, D., et al., Surface carboxyl groups enhance the capacities of carbonaceous oxygen electrodes for aprotic lithium‒oxygen batteries: A direct observation on binder-free electrodes, Chin. Chem. Lett. 2019(30): 2328-2332.

[39] Xu, J.; Xu, F.; Qian, M., et al., Conductive Carbon Nitride for Excellent Energy Storage, Adv Mater. 2017(29): 87-99.

[40] Yao, L.; Lin, J.; Li, S., et al., Metal-organic frameworks-derived hollow dodecahedral carbon combined with FeNx moieties and ruthenium nanoparticles as cathode electrocatalyst for lithium oxygen batteries, J. Colloid Interface Sci. 2021(596): 1-11.

[41] Du, D.; Zheng, R.; He, M., et al., A-site cationic defects induced electronic structure regulation of $LaMnO_3$ perovskite boosts oxygen electrode reactions in aprotic lithium – oxygen batteries, Energy Storage Mater. 2021(43): 293-304.

[42] Shen, J.; Wu, H.; Sun, W., et al., In-situ nitrogen-doped hierarchical porous hollow carbon spheres anchored with iridium nanoparticles as efficient cathode catalysts for reversible lithium-oxygen batteries, Chem. Eng. J. 2019(358): 340-350.

[43] Zhang, Y.; Ma, J.; Yuan, M. W., et al., The design of hollow PdO-Co_3O_4 nano-dodecahedrons with moderate catalytic activity for Li-O_2 batteries, Chem. Commun. (Camb.). 2019(55): 12683-12686.

[44] Zheng, M.; Jiang, J.; Lin, Z., et al., Stable Voltage Cutoff Cycle Cathode with Tunable and Ordered Porous Structure for Li-O_2 Batteries, 2018(14): e1803607.

[45] Zhao, Z.; Liu, Y.; Wan, F., et al., Free-standing nitrogen doped graphene/$Co(OH)_2$ composite films with superior catalytic activity for aprotic lithium-oxygen batteries, Chin. Chem. Lett. 2021(32): 594-597.

[46] Wang, F.; Qiao, J.; Wang, J., et al., Multimetallic Core – Bishell Ni@Au@Pd nanoparticles with reduced graphene oxide as an efficient bifunctional electrocatalyst for oxygen reduction/evolution reactions, J. Alloys Compd. 2019(811): 3.

[47] Wen, C.; Zhu, T.; Li, X., et al., Nanostructured Ni/Ti_3C_2T MXene hybrid as cathode for lithium-oxygen battery, Chin. Chem. Lett. 2020(31): 1000-1003.

[48] Liu, X.; Huang, Q.; Wang, J., et al., In-situ deposition of Pd/Pd4S heterostructure on hollow carbon spheres as efficient electrocatalysts for rechargeable Li-O_2 batteries, Chin. Chem. Lett. 2021(32): 2086-2090.

[49] Ding, N.; Chien, S. W.; Hor, T. S. A., et al., Influence of carbon pore size on the discharge capacity of Li – O_2batteries, J. Mater. Chem. 2014(A 2): 12433-12441.

[50] Shui, J.; Du, F.; Xue, C., et al., Vertically Aligned N-Doped Coral-like Carbon Fiber Arrays as Efficient Air Electrodes for High-Performance Nonaqueous Li-O-2 Batteries, ACS Nano 2014(8): 3015-3022.

[51] Zhang, J.; Chen, X.; Lei, Y., et al., Highly rechargeable lithium oxygen batteries cathode based on boron and nitrogen co-doped holey graphene, Chem. Eng. J. 2022(428):7.

[52] Yi, L. C.; Ci, S. Q.; Sun, C. L., et al., Cathode Materials of Non-Aqueous Lithium-Oxygen Battery, Progress in Chemistry. 2016(28): 1251-1264.

[53] Bui, H. T.; Kim, D. Y.; Kim, D. W., et al., Carbon nanofiber@platinum by a coaxial electrospinning and their

improved electrochemical performance as a Li–O$_2$ battery cathode, Carbon. 2018(130): 94-104.

[54] Jeong, Y. S.; Park, J.-B.; Jung, H.-G., et al., Study on the Catalytic Activity of Noble Metal Nanoparticles on Reduced Graphene Oxide for Oxygen Evolution Reactions in Lithium-Air Batteries, Nano Lett. 2015(15): 4261-4268.

[55] Lu, Y.-C.; Xu, Z.; Gasteiger, H. A., et al., Platinum-Gold Nanoparticles: A Highly Active Bifunctional Electrocatalyst for Rechargeable Lithium-Air Batteries, J. Am. Chem. Soc. 2010(132): 12170-12171.

[56] Choi, R.; Jung, J.; Kim, G., et al., Ultra-low overpotential and high rate capability in Li – O2 batteries through surface atom arrangement of PdCu nanocatalysts, Energy Environ. Sci. 2014(7): 1362-1368.

[57] Jung, H.-G.; Jeong, Y. S.; Park, J.-B., et al., Ruthenium-Based Electrocatalysts Supported on Reduced Graphene Oxide for Lithium-Air Batteries, ACS Nano. 2013(7): 3532-3539.

[58] Wang, P.; Ren, Y.; Wang, R., et al., Atomically dispersed cobalt catalyst anchored on nitrogen-doped carbon nanosheets for lithium-oxygen batteries, Nat. Commun. 11(2020): 1576.

[59] Gao, R.; Li, Z.; Zhang, X., et al., Carbon-Dotted Defective CoO with Oxygen Vacancies: A Synergetic Design of Bifunctional Cathode Catalyst for Li – O$_2$ Batteries, ACS Catalysis 6(2015): 400-406.

[60] Lin, Y.; Yang, Q.; Geng, F., et al., Suppressing Singlet Oxygen Formation during the Charge Process of Li-O$_2$ Batteries with a Co3O4 Solid Catalyst Revealed by Operando Electron Paramagnetic Resonance, J. Phys. Chem. Lett. 2021(12): 10346-10352.

[61] Zhang, P.; Sun, D.; He, M., et al., Synthesis of Porous delta-MnO2 Submicron Tubes as Highly Efficient Electrocatalyst for Rechargeable Li-O$_2$ Batteries, ChemSusChem. 2015(8): 1972-1979.

[62] Minowa, H.; Hayashi, M.; Hayashi, K., et al., Mn – Fe-based oxide electrocatalysts for air electrodes of lithium – air batteries, J. Power Sources. 2013(244): 17-22.

[63] Li, P.; Zhang, J.; Yu, Q., et al., One-dimensional porous La0.5Sr0.5CoO2.91 nanotubes as a highly efficient electrocatalyst for rechargeable lithium-oxygen batteries, Electrochim. Acta. 2015(165): 78-84.

[64] Ma, Z.; Yuan, X.; Li, L., et al., The double perovskite oxide Sr2CrMoO(6-delta) as an efficient electrocatalyst for rechargeable lithium air batteries, Chem. Commun. (Camb.) 2014(50): 14855-14858.

[65] Zhu, X.; Pan, X.; Wu, Y., et al., Layered perovskite oxide PrBaCo2O5+δ as a potential cathode for lithium–oxygen batteries: High-performance bi-functional electrocatalysts, Mater. Lett. 2019(237): 200-203.

[66] Sun, B.; Chen, S.; Liu, H., et al., Mesoporous Carbon Nanocube Architecture for High-Performance Lithium-Oxygen Batteries, Adv. Funct. Mater. 2015(25): 4436-4444.

[67] Guo, X.; Liu, P.; Han, J., et al., 3D Nanoporous Nitrogen-Doped Graphene with Encapsulated RuO2 Nanoparticles for Li-O$_2$ Batteries, Adv Mater. 2015(27): 6137-6143.

[68] Lian, Z.; Lu, Y.; Ma, S., et al., Metal atom-doped Co3O4 nanosheets for Li-O$_2$ battery catalyst: Study on the difference of catalytic activity, Chem. Eng. J. 2022(445):98-109.

[69] Li, J.; Zhou, H.; Jian, Z., et al., Improved Electrocatalytic Activity of Three-Dimensional Open-Structured Co3O$_4$@MnO$_2$ Bifunctional Catalysts of Li-O2 Batteries by Inducing the Oriented Growth of Li2O$_2$, ACS Sustainable Chemistry & Engineering. 2021(9): 5334-5344.

[70] Lin, H.; Liu, Z.; Mao, Y., et al., Effect of nitrogen-doped carbon/Ketjenblack composite on the morphology of Li2O2 for high-energy-density Li – air batteries, Carbon. 2016(96): 965-971.

[71] Cui, R.; Xiao, Y.; Li, C., et al., Polyaniline/reduced graphene oxide foams as metal-free cathodes for stable lithium-oxygen batteries, Nanotechnology. 2020(31): 445402.

[72] Li, F.; Ohnishi, R.; Yamada, Y., et al., Carbon supported TiN nanoparticles: an efficient bifunctional catalyst for non-aqueous Li-O$_2$ batteries, Chem. Commun. (Camb.) 2013(49): 1175-1177.

[73] Cao, X.; Chen, Z.; Wang, N., et al., Defected molybdenum disulfide catalyst engineered by nitrogen doping for advanced lithium – oxygen battery, Electrochim. Acta 2021(383): 2.

[74] Sun, K.; Liu, M.; Yu, S., et al., In-situ grown vanadium nitride coated with thin layer of nitrogen-doped carbon as a highly durable binder-free cathode for Li – O$_2$ batteries, J. Power Sources. 2020(460):6.

Viser Technology Pte. Ltd.
Research and Application of Materials Science
DOI: 10.33142/rams.v4i1.8462

Research Article Open Access

One dimensional terpyridine-based metal organic framework for stable supercapacitor

Haoxuan FENG, Weiqi LI, Chenyu MA *, Haiyan HE

College of Mechanics and Materials, Hohai University, Nanjing, Jiangsu, 210098, China

****Corresponding Author:*** *Chenyu MA, E-mail addresses: chenyuma1999@163.com*

Abstract:
In summary, a novel structure of MOF based on 1,4–di ([2,2':6',2"terpyridin] -4'-yl)benzene and 1,4-naphthalenedicarboxylic acid has been constructed through hydrothermal reaction. The Ni-MOF displays one dimensional zigzag chain, which connect each other by hydrogen bonding to form three dimensional supramolecule with large channels. The conjugated systems of the terpyridin and benzene ligands enhance the chain rigidity, accelerate the electron transport. The massive channels provides electrolyte rapid transfer. By the structural feature aforementioned, the Ni-MOF demonstrates stable electrochemical performance as suprocapacitor.

Keywords: *suprocapacitor; metal-organic framework; supramolecule; terpyridin; hydrothermal reaction*

1 Introduction

In recent years, with the decline of non-renewable resources and the global demands for clean energy shortage, the development of clean and efficient energy storage equipment has become an important research direction. However, chemical and physical limitations of existing materials hinder performance and require new solutions. For instance, polymers and conductive carbon materials are relatively inexpensive, scalable, and synthetically tunable but can lack physical and chemical stability for device implementation. On the other hand, solid inorganic materials, such as metal oxides and silicon, are used as electrode materials due to their robust structure and redox-active sites. However, sluggish ion diffusion of metal oxides limit charge discharge rate capabilities and large volumetric changes lead to mechanical instability [1]. Metal Organic Frameworks are one reasonable type of materials to solve the above issues due to their metal atoms and organic skeletons, adjustable channels and extraordinary porosity, which display different applications by diverse metal atoms [2-4]. MOFs are entering the limelight as supercapacitors by virtue of the tunable structure, large specific surface area and amount of accessible active centers [5-7]. Meanwhile, MOFs materials can be used as redox centers of pseudo-capacitors, which can accelerate the reaction because of their skeleton structure and many active sites.

Supercapacitors have two main mechanism: a double-layer capacitor and a pseudo-capacitor [8-10].

Double-layer capacitor works on the principle that during charging, ions with opposite charges accumulate on the electrode surface and are stored between the electrodes and electrolytes. The double-layer capacitor has good invertibility and power density because of its fast electrochemical reaction near the surface. The pseudo-capacitorsused in this paper is mainly charged and discharged through the rapid oxidation-reduction reaction on the electrode surface, which reflects well the efficiency of the supercapacitor because of the rapid reaction [11-13]. Due to the high specific surface area of carbon materials, activated carbon, carbon nanotubes and graphene are commonly used as electrode materials in current research. Despite carbon materials have such excellent characteristics, they are not necessarily suitable for supercapacitors. For example, Chao Feng et al. reported a Ni-MOF material with a specific capacitance of 184 F/g at a rate of 5 mV/s [14]. Yue et al reported a kind of Zn-MOF used in supercapacitors. At the current density of 0.5 A/g, the specific capacitance is only 138 F/g[15]. When these materials are used as supercapacitors, they have no good energy storage effect because of their small specific capacitance. Chao Feng et al. reported a Ni-MOF material has lost a lot of specific capacitance under 1000 cycles [16-17].A kind of MOFs used in supercapacitor is reported by Kong et al. After 1000 charge-discharge cycles, the specific capacitance keeps only 72.8% [18]. It indicates that the MOFs material has short service life when used as a supercapacitor, which does not accord with the characteristics of long service life of supercapacitors. While some MOFs have high

Received on March 11, 2022; Accepted on April 18, 2022

specific capacitance and good cycle stability when they are used as supercapacitors, they will lose large specific capacitance when they are used as supercapacitors at high current density. When the material is used as a supercapacitor, the specific capacitance can only keep 71.21% at the current density of 10 A/g at Kang Liu et al.'s paper [19]. At the current density of 20 A/g, the specific capacitance of Zhu et al supercapacitor is only 47.2% [20].

Based on the above question, a Ni-based MOFs material was synthesized by in-situ reaction and its structure was characterized in this paper. The electrochemical performance of the supercapacitor was also evaluated.

2 Experimental section

2.1 Synthesis of HU17

All the reagents were purchased and used directly without further purification, Ni-MOF was synthesized by hydrothermal method, 0.02 g of $Ni(NO_3)_2$, 0.001g of 1,4-di([2,2':6',2''terpyridin]-4'-yl)benzene (1,4-Tpb), 0.005g of 1,4-naphthalenedicarboxylic acid (1,4-Npa) with a balance, and then mixing them with 5 ml distilled water. The glass bottle is put into the plastic inner liner, and then the inner liner is put into the sealed reactor. It was cooled naturally after 72 hours reaction at 150 ℃. If all the impurities are yellow dendritic crystals and a few yellow massive crystals, they will be regarded as pure. The product was extracted into the sample tube and dried in a 50 ℃ constant temperature oven to obtain the required crystals.

2.2 Single-crystal structure determination

The single crystal HU17 was diffracted by Agilent SuperNova X-ray diffractometer at 298K(radiation type is MOK/a, radiation wavelength is 0.71 Å). The crystal table is shown in Table 1.

2.3 Electrochemical measurements

Two rectangular nickel foams with the same shape and similar size are cut and it's twice as long as it's wide. First weighing the quality of two pieces of nickel foam, removing one nickel foam and setting the balance to zero, the sample is 2.5 mg at the end of the remaining nickel foam. Cover with another nickel foam, wrap it in weighing paper, and put it into a tablet press.

In this paper, three-electrode test is used. Pt sheet is used as the opposite electrode, the reference electrode is the saturated calomel electrode, and the working electrode is the MOFs material electrode. The electrolyte solution is 6 Mol/L KOH.

2.3.1Cyclic voltammeters:

The specific capacitance of electrode material is measured by cyclic voltammetry. The formula is

$$C = \frac{\int \mathrm{idu}}{\mathrm{mv}\triangle V} \qquad (1)$$

Among them, C is the specific capacitance (F/g), m is the mass (g) of MOFs, △V is the Window voltage (V), i is the current intensity (A), and v is the scanning rate (mV/s)[21].

We can get different specific capacitance by changing the scanning rate v.

2.3.2Constant current charge and discharge test:

Constant current charging and discharging is to use constant current to test electrode material. The formulais

$$C = \frac{I\triangle \mathrm{t}}{\mathrm{m}\triangle V} \qquad (2)$$

Among them, C is the specific capacitance (F/g), m is the mass (g) of MOFs, △t is the Discharge time (s), I is the current intensity (A), and △V is Window voltage (V)[22-23].

We can obtain specific capacitance at different current by changing current.

2.3.3Impedance test:

Two test voltages are set, one is 0.45 V, and the other is the voltage corresponding to the oxidation peak in the CV curve. Test frequency is 0.01 Hz-100KHz.

Table 1 Crystal date and structure refinement for complexes HU17

complex	HU17
empirical formula	C60 H42 N6 O11 Ni2
formula weight	1140.41
T (K)	293.15
crystal system	triclinic
space group	P1 2/n1 (13)
a (Å)	11.4409 (8)
b (Å)	14.8757 (9)
c (Å)	17.6457 (11)
α (°)	74.092 (2)
β (°)	76.830 (2)
γ (°)	79.855 (2)
V (Å 3)	2791.4 (3)
Z	2
Dc (Mg mm-3)	1.357
μ (mm-1)	0.740
F (000)	1176
index ranges (h, k, l)	-13/13 -17/17 -21/20
reflections collected	7049
Rint	0.0481
restraints/parameters	0/716
GOF (F2)	1.009
R1,wR2 [I > 2σ(I)]a	0.0547, 0.1333
R1,wR2 (all data)b	0.0896, 0.1445
Largest diff. peak/hole (e ·Å-3)	0.413, - 0.304

a R1 = Σ| |Fo|-|Fc| |/ Σ|Fo|

b wR2 = [Σw(Fo2-Fc2)2]/ Σw(Fo2)2]1/2

3 Results and discussion

3.1 Crystal structure of HU17

A novel structure of MOF based on 1,4-di([2,2':6',2"terpyridin] -4'-yl)benzene (1,4-Tpb) and 1,4-naphthalenedicarboxylic acid (1,4-Npa) has been constructed by solvothermal reaction. The asymmetric unit contains two central atoms (Ni1 and Ni2), one1,4-Npa ligand, one 1,4-Tpb ligand, and three coordinated water molecules. As can be seen from the Figure 1, the central atom Ni has two coordination environments. Figure 1(a) shows the Ni1 is a tridentate chelate with a 1,4-Tpb, one 1,4-Npa and two H2O. Figure 1(b) shows the Ni2 is a tridentate chelate with a 1,4-Tpb, one H2O and two 1,4-Npa, respectively. The asymmetric units are directly connected to form a chain. 1,4-Npa presents two coordination environments, one is bridged with two metal center ions Ni, as shown in Figure 1(c); the other is bridged with only one metal center ion Ni, as shown in Figure 1(d). There is only one coordination environment for 1,4-Tpb, that is, the two ends are tridentate chelate with two metal center ions Ni. Figure 1(f) shows the asymmetric unit of complex HU17. It is composed of two units in Figure 1 connected by a common 1,4-Npa. Figure 1 (g) shows the molecular chain of HU17. It is composed of asymmetric units connected. Figure 1(h) is a schematic diagram of the connections between different chains. From the figure, we can see that there is no link between the chain and the chain. Considering the hydrogen bonds with an average distance of 2.67 Å, two parallel chains connected to form a supramolecule network. Figure 1(i) is a schematic diagram of the connection modes of adjacent network structures. The adjacent mesh structures are connected to each other form three-dimensional structures. There are some independent water molecules occupied the channels of these chains.

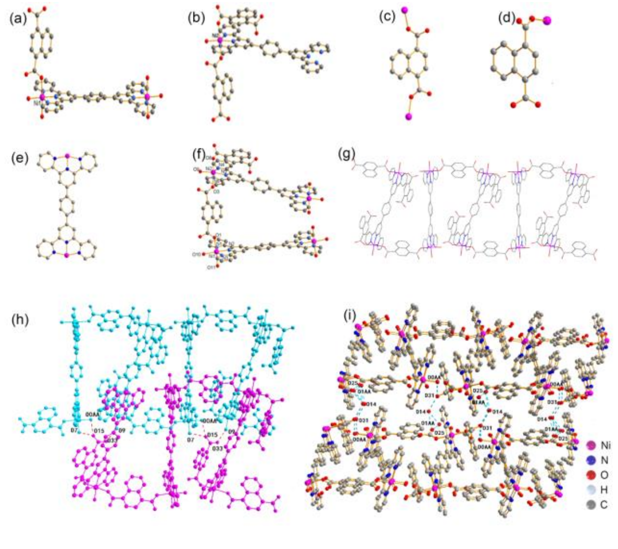

Figure 1 (a) Coordination environment of Ni1; (b) coordination environment of Ni2; (c) and (d) the coordination modes of 1,4-Npa; (e) the bridging mode of 1,4-Tpb; (f) an asymmetric unit of HU17, (g) the single chain structure of HU17; (h) The hydrogen bonds between two chains; (i) The 3D network of HU17

Figure 2 shows the thermogravimetric curve of HU17. It can be seen from the figure that in the range of 0 to 300 ℃, the complex HU17 loses 7% of its mass, which is a process of gradually losing crystal water .In the range of 300 to 780℃, the mass of the complex HU17 is greatly reduced, and 80% of the total mass is lost, because its crystal skeleton is gradually oxidized and decomposed. Above 780℃, the mass increases slightly because the metal is oxidized to metal oxides.

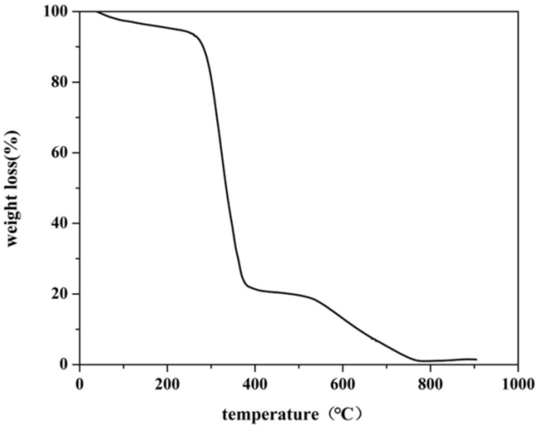

Figure 2 Thermogravimetry analysis of HU17

The GCD curve is shown in Figure 3(a). The current density gradually increased from 1 A/g to 20 A/g. with the increase of current density, the charging and discharging time became shorter and the curve compressed to the ordinate. According to formula b, the specific capacitance of complex HU17 can be calculated. The calculated results are represented by histogram, and the schematic diagram of specific capacitance is Figure 3(c). As can be seen from Figure 3(c), with the increase of current density, the specific capacitance decreases gradually. This is because under the large current density, the charging and discharging time decreases, and all active sites cannot be fully called, so that some active sites are not involved in the charging and discharging, resulting in the reduction of specific capacitance. At the current densities of 1 A/g, 2 A/g, 5 A/g, 10 A/g, 15 A/g and 20 A/g, the specific capacitances are 135.5, 132.4, 127.5, 122.4, 121.6 and 117.2 F/g, respectively. It can be seen that the specific capacitances at 20 A/g and 1 A/g current densities are only 13.5% compared with each other, indicating that the complex HU17 has a faster reaction rate when it is used as a super capacitor, which conforms to the characteristics of fast charging of super capacitor.

Figure 3(b) is the CV test curve. It can be seen from the figure that in the cyclic voltammetry test, the super capacitor has oxidation peak and reduction peak, indicating that the super capacitor is a Faraday capacitor. At the same time, we can see that with the increase of scanning rate, the curve deforms to a certain extent, which shows that the capacitor becomes unstable under high scanning rate. Formula a can be used to calculate the specific capacitance of materials at different scanning rates, and the specific capacitance is displayed by histogram. At the scanning rates of 1 mV/s, 2 mV/s, 4 MV/s, 6 MV/s, 8 MV/s, and 10 mV/s, the specific capacitance is 332.8, 314.7, 294.8, 283, 274.8, 268.9 and 258.6 F/g, respectively. It can be seen that at the scanning rate of 1 mV/s, the material has high specific capacitance, which is in line with the characteristics of high capacitance of super capacitor. At the same time, it can also be seen that the specific capacitance loss rate is only 22.3% at the scanning rate of 20 mV/s and 1 mV/s, that is to say, at the high scanning rate, the electrode material can still maintain a high efficiency, which shows that the electrode material has good stability at high scanning speed.

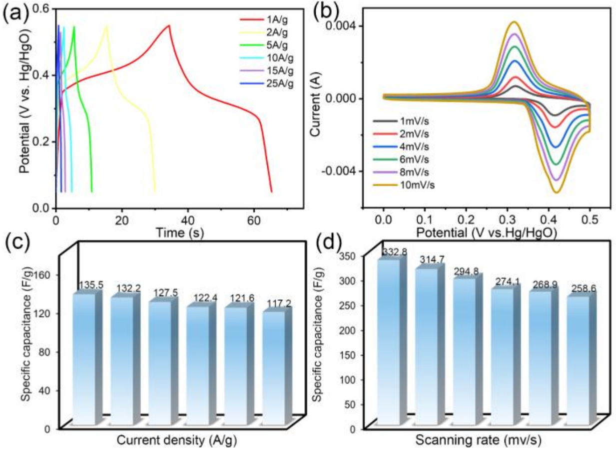

Figure 3 (a) The GCD curve of HU17, (b) the CV curve of HU17, (c) the specific capacitance measured under GCD curves, and (d) the specific capacitance measured under CV curves

The EIS curve of this MOF electrode material is shown in Figure 4 Curve 1 is 0.45V, and Curve 2 is the voltage corresponding to the oxidation peak in the CV curve. From Figure 4(b), it can be seen that the HU17 electrode material has a small semicircle in the high frequency region, which indicates that the electrode material has a small internal resistance. In Figure 4(a), it can be seen that the slope of HU17 electrode material is small in the low frequency region, which indicates that the electron transfer rate of HU17 electrode material is not very fast.

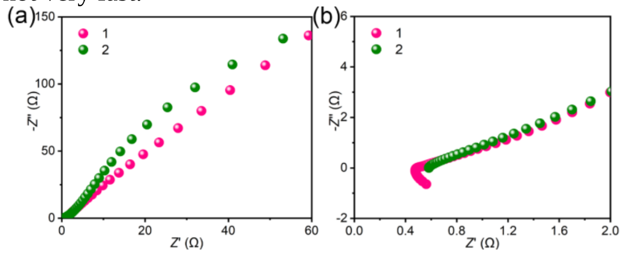

Figure 4 (a) The low frequency zone of EIS Curve and (b) the high frequency zone of EIS curve

Figure 5 shows the cyclic stability curve of HU17 for supercapacitors. It can be seen that the capacitance efficiency of the electrode material can remain 100% after 10000 charge-discharge cycles. This indicates that HU17 has excellent cyclic life for supercapacitors and is suitable for supercapacitors.

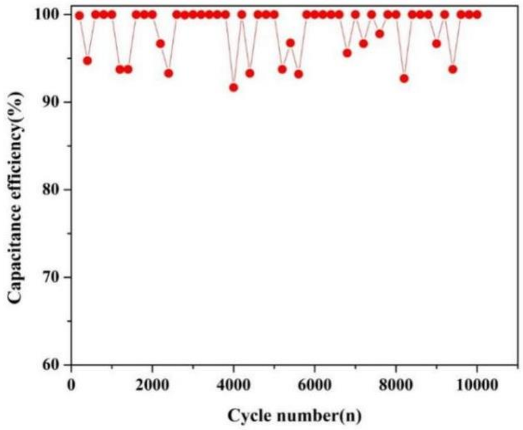

Figure 5 The cyclic stability curve of HU17

4 Conclusions

In summary, a novel structure of MOF based on 1,4–di ([2,2':6',2"terpyridin] -4'-yl)benzene and 1,4-naphthalenedicarboxylic acid has been constructed. The Ni-MOF displays one dimensional zigzag chain, which connect each other by hydrogen bonding to form three dimensional supramolecule with large channels. The conjugated system of the terpyridin and benzene ligands enhance the chain rigidity, accelerate the electron transport. The massive channels provides electrolyte rapid transfer. By the structural feature aforementioned, the Ni-MOF demonstrates stable electrochemical performance as suprocapacitor.

Acknowledgments

This work was financially supported by the National Natural Science Foundation of China (22209037) and the Fundamental Research Funds for the Central Universities (No. B220202042).

References

[1] E. Baumann, A. Burns, Q. Liu, et al. Metal-organic framework functionalization and design strategies for advanced electrochemical energy storage devices, Commun. Chem. 2019(2): 13.

[2] H. Furukawa, E. Cordova, M. O'Keeffe, et al. The chemistry and applications of metal-organic frameworks, Science. 2013(341): 1230444.

[3] X. Du, W. Cai, Q. Zhang, et al. Rhodium nanoflowers on three-dimensional graphitic carbon nitride nanosheets/graphene hybrid aerogels as electrocatalysts for methanol oxidation, ACS Appl. Nano Mater. 2021(4): 9729–9737.

[4] J. Qin, H. Huang, J. Zhang, et al. Stereoassembly of

ultrasmall Rh-decorated zeolite imidazolate framework–MXene heterostructures for boosted methanol oxidation reaction, J. Mater. Chem. A 2023(11): 2848-2856.

[5] D. Sheberla, J. Bachman, J. Elias, et al. Conductive MOF electrodes for stable supercapacitors with high areal capacitance, Nat. Mater. 2017(16):220-224.

[6] L. Wang, X. Feng, L. Ren, et al. Flexible solid-state supercapacitor based on a metal-organic framework interwoven by electrochemically-deposited PANI, J. Am. Chem. Soc. 2015(137):4920-4923.

[7] R. Salunkhe, Y. Kaneti, J. Kim, J. Kim, Y. Yamauchi, Nanoarchitectures for metal-organic framework-derived nanoporous carbons toward supercapacitor applications, Acc.Chem. Res. 49 (2016):2796-2806.

[8] G. Wang, L. Zhang, J. Zhang. A review of electrode materials for electrochemical supercapacitors, Chem. Soc. Rev. 2012(41):797-828.

[9] P. Simon, Y. Gogotsi. Materials for electrochemical capacitors, Nat. Mater. 7 (2008) 845-854.

[10] R. Kotz, M. Carlen. Principles and applications of electrochemical capacitors, Electrochim. Acta. 2000(45):2483-2498.

[11] J. Qiu, Z. Bai, G. Dai, et al. NiO/Co_3O_4 nanoheterostructure derived from nickelocene filled ZIF-67 for supercapacitors, J Alloy. Compd. 2018(763): 966-974.

[12] J. Xu, Y. Wang, S. Cao, et al. Ultrathin Cu-MOF@δ-MnO_2 nanosheets for aqueous electrolyte-based high-voltage electrochemical capacitors, J. Mater. Chem. 2018(A 6): 17329-17336.

[13] Y. Zhang, R. Lin, Y. Fu, et al. Metal-organic framework derived Fe_2O_3 nanocubes on intertwined N-doped carbon nanowires for fiber-shaped supercapacitor, Mater. Lett. 2018(228): 9-12.

[14] X. Fang, B. Zong, S. Mao. Metal-organic framework-based sensors for environmental contaminant sensing, Nano-Micro Lett. 2018(10): 64.

[15] Y. Hou, L. Yan, X. Wang, et al. Excellent supercapacitor performance of robust nickel–organic framework materials achieved by tunable porosity, inner-cluster redox, and in situ fabrication with graphene oxide, Cryst. Growth Des. 2018(18): 6035-6045.

[16] C.Feng, P. Lv, Q. Li, et al. A porous 2D Ni-MOF material with a high supercapacitive performance, J. Solid State Chem. 2018(265): 244-247.

[17] H. Meng, B. Wan, P. Jiang, et al. Rodlike CeO_2/carbon nanocomposite derived from metal–organic frameworks for enhanced supercapacitor applications, J. Mater. Sci. 2018(53): 13966-13975.

[18] M. Yue, C. Yu, H. Duan, et al. Six isomorphous window-beam MOFs: explore the effects of metal ions on MOF-derived carbon for supercapacitors, Chem. 2018(24): 16160-16169.

[19] J. Kong, J. Zhu, W. Shuang, et al. Nitrogen-doped wrinkled carbon foils derived from MOF nanosheets for superior sodium storage, Adv. Energy Mater. 2018(8): 1-8.

[20] K. Liu, M. Deng, D. Li, et al. Two isostructural Co/Ni fluorine-containing metal-organic frameworks for dye adsorption and supercapacitor, J. Solid State Chem. 2019(275): 1-7.

[21] Z. Zhu, Z. Wang, Z. Yan, et al. Facile synthesis of MOF-derived porous spinel zinc manganese oxide/carbon nanorods hybrid materials for supercapacitor application, Ceram. Int. 2018(44): 20163-20169.

[22] R. Salunkhe, Y. Kamachi, N. Torad, et al. Fabrication of symmetric supercapacitors based on MOF-derived nanoporous carbons, J. Mater. Chem. 2014(A 2): 19848-19854.

[23] W. Xuan, R. Ramachandran, C. Zhao. F. Wang, Influence of synthesis temperature on cobalt metal-organic framework (Co-MOF) formation and its electrochemical performance towards supercapacitor electrodes, J. Solid State Electrochem. 2018(22): 3873-3881.

Publisher: Viser Technology Pte. Ltd.

URL: www.viserdata.com
Add.:21 Woodlands Close, #08-18,
Primz Bizhub SINGAPORE (737854)